

---

# On the dark matter halos of massive galaxies under baryon-driven contraction.

---

**Submitted by:** Naoise Holmes - holmesna@tcd.ie

**Supervisors (AIP):** Marcel Pawlowski, Pengfei Li

**Supervisor (FU):** Stefanie Russ

**Supervisor (MPG):** Dirk Manske

May 29, 2024



# Abstract

The prevailing model of galaxy formation states that galaxies form in the gravitational potentials created by dark matter halos. As these halos accrete hydrogen gas, its additional gravitational potential can compress the halo. Conventional dark matter-only simulations indicate that primordial halos exhibit a cuspy nature, a premise in tension with observed galactic dynamics. The effects of gas accretion on halo structure has often been overlooked when interpreting these observational dynamics. A recent study simulated the baryonic compression of primordial Navarro-Frenk-White (NFW) halos, tailored to replicate the specific baryonic distribution of galaxies from the Spitzer Photometry and Accurate Rotation Curve (SPARC) sample. The simulations revealed considerable structural changes to the dark matter halos of massive galaxies. The primordial NFW halos evolved to be even more cuspy, thereby widening the gap between theoretical models and empirical data. Expanding on that study, the current research investigates the effects of baryonic compression on primordial Einasto halos, focusing on 31 massive galaxies from the SPARC sample, offering a comprehensive understanding of potential variations between the two halo models.

**Declaration of Authorship**

*Disclaimer: Please note that only the German version of this document is legally binding. This translation is intended for the convenience of the non-German-reading public and is for informational purposes only.*

|                           |  |
|---------------------------|--|
| Last name: Holmes         | (Please use block capitals or typescript.) |
| First name: Naoise        |  |
| Date of birth: 01.07.1985 |  |
| Student number: 5566969   |  |

I hereby declare to Freie Universität Berlin that I have completed the following Master's Thesis independently and without the use of sources and aids other than those cited.

I declare that the present work is free of plagiarism. Any statements that have been taken from other writings, whether directly or indirectly, have been clearly marked as such.

Further, I declare that this work has not been submitted to any other university as part of an examination attempt, either in identical or similar form, nor has it been published elsewhere.

Date: 29.05.24

Signature: Naoise Holmes

( \_\_\_\_\_ )

# Contents

|          |   |           |
|----------|---|-----------|
| <b>1</b> | <b>Introduction</b>   | <b>1</b>  |
| 1.1      | Observational Evidence of Dark Matter . . . . .                                 | 1         |
| 1.2      | Candidates of Dark Matter Particles . . . . .                                   | 6         |
| 1.2.1    | Baryonic Dark Matter . . . . .  | 6         |
| 1.2.2    | Non-Baryonic Dark Matter . . . . .  | 8         |
| 1.3      | Structure Formation Simulations Based on Cold Dark Matter . . . . .             | 8         |
| 1.4      | Models of Dark Matter Halos . . . . .   | 11        |
| 1.4.1    | NFW Profiles . . . . .  | 11        |
| 1.4.2    | Einasto Profiles . . . . .  | 11        |
| 1.4.3    | Core-Cusp Problem . . . . .   | 13        |
| 1.5      | Baryonic Effects on Dark Matter Halos . . . . .                                 | 14        |
| <b>2</b> | <b>Method &amp; Data</b>  | <b>21</b> |
| 2.1      | Adiabatic Contraction of Dark Matter Halos . . . . .                            | 21        |
| 2.1.1    | Methodology of Modelling Halo Contractions . . . . .                            | 21        |
| 2.1.2    | COMPRESS: A Numerical Realisation of Adiabatic Contraction . . . . .            | 21        |
| 2.1.3    | Generating Initial halos . . . . .  | 23        |
| 2.2      | The SPARC Sample . . . . .  | 23        |
| 2.3      | Deriving Dark Matter Halos For Disk Galaxies . . . . .                          | 25        |
| 2.3.1    | The Traditional Approach . . . . .  | 25        |
| 2.3.2    | New Approach: Incorporating Halo Contractions . . . . .                         | 27        |
| 2.4      | Bayesian Analysis . . . . .   | 29        |
| 2.4.1    | Constraints on Baryonic Disks . . . . .   | 30        |
| 2.4.2    | Constraints on Dark Matter Halos . . . . .                                      | 30        |
| <b>3</b> | <b>Results</b>  | <b>32</b> |
| 3.1      | Individual Rotation Curve Fits . . . . .  | 32        |
| 3.2      | Analysis of Best-Fit & Optimal-Fit Parameters . . . . .                         | 37        |
| 3.2.1    | Mass-to-Light Ratios . . . . .  | 37        |
| 3.2.2    | Checking the Priors on the Initial Dark Matter Halos . . . . .                  | 41        |
| 3.3      | Properties of Compressed Halos . . . . .  | 43        |
| 3.3.1    | Halo Evolution . . . . .  | 44        |
| 3.3.2    | Inner Halo Structure . . . . .  | 46        |
| 3.4      | Possible Solution With Baryonic Feedback: Comparison With Simulations . . . . . | 49        |
| 3.4.1    | Stellar Feedback . . . . .  | 49        |
| 3.4.2    | AGN Feedback . . . . .  | 51        |
| <b>4</b> | <b>Discussion &amp; Outlook</b>   | <b>58</b> |
|          | <b>Bibliography</b>   | <b>62</b> |
| <b>A</b> | <b>Appendix</b>   | <b>67</b> |

# 1 Introduction

## 1.1 Observational Evidence of Dark Matter

Dark matter is a form of unseen matter that does not emit, absorb, or reflect light, but is believed to account for a 85% of all matter in the universe. Its presence is inferred from its gravitational effects on visible matter and the evolution of large-scale structure formation in the universe. In spite of its apparent abundance, direct evidence of it remains elusive. However, there is ample indirect evidence supporting the necessity for the existence of dark matter.

**Evidence In Galaxy Clusters:** The first evidence for dark matter was observed by Swiss astronomer Fritz Zwicky in 1933 during his study of the Coma galaxy cluster (Zwicky, 1933; Andernach and Zwicky, 2017). A galaxy cluster is a large-scale structure consisting of hundreds to thousands of galaxies bound together by gravitational forces. An image of the Coma cluster is displayed in Figure 1.1, where most bright spots correspond to individual galaxies.<sup>1</sup> Zwicky (1933) discerned a substantial discrepancy between the dynamical mass and the observable mass of the Coma cluster.



**Figure 1.1:** Left: The Coma cluster of galaxies. The Coma cluster has been extensively studied and it is now known to contain over 1000 galaxies. Right: Messier 81 spiral galaxy. Images credit: Sloan Digital Sky Survey.

Revisiting Zwicky (1933)'s measurements allows for a re-estimation of this discrepancy. He estimated that the cluster had a radius,  $R = 10^6$  ly. Utilising Doppler shift measurements from several galaxies within the cluster, he calculated the radial velocity dispersion as described by

$$\sigma_r = \sqrt{\frac{1}{n} \sum_{i=1}^n (v_{r,i} - \bar{v}_r)^2} = 1000 \text{ km/s} \quad (1)$$

where  $\bar{v}_r$ ,  $v_{r,i}$  and  $n$  denote the average radial velocity, individual radial velocities of the  $i$ -th galaxy, and the number of measured galaxies, respectively. Subsequently, the crossing time-scale, the time it takes for a galaxy to cross the galaxy cluster, was calculated as

$$t_{\text{cross}} = \frac{R}{\sigma_v} \approx 2 \times 10^8 \text{ yr} \ll t_{\text{uni}} \quad (2)$$

where  $t_{\text{uni}} = 13.6$  Gyr, is the age of the universe. Since  $t_{\text{cross}} \ll t_{\text{uni}}$ , then unless the cluster formed very late it implies that the cluster is gravitationally bound since if this

<sup>1</sup>The brightest spot with a cross-shaped artefact from overexposure is a foreground star.

were not the case then the cluster would have already dissolved. Assuming the cluster did not form very late then the short crossing time relative to  $t_{\text{uni}}$  implies that the cluster is likely in equilibrium, justifying the use of the virial theorem in estimating the dynamical mass of the cluster. The virial theorem states

$$2\langle T \rangle = -\langle U \rangle \quad (3)$$

where  $T$  and  $U$  are the kinetic and potential energy respectively. [Zwicky \(1933\)](#) estimated the total number of galaxies in the Coma cluster to be  $N = 800$ , each with an average observable mass of  $m = 10^9 M_{\odot}$ , where  $M_{\odot}$  represents the mass of the Sun. Using the virial theorem, he determined that the observed cluster mass corresponds to a maximum radial velocity dispersion of  $\sigma \approx 80$  km/s. However, this velocity dispersion is significantly lower than the radial velocity dispersion reported by [Zwicky \(1933\)](#), which is  $\sigma \approx 1000$  km/s. The observed velocity dispersion suggests that the cluster could not be gravitationally bound by the observable mass. This discrepancy in the velocity dispersion yields a total dynamical mass that is approximately 400 times greater than the estimated visible mass of the cluster. This dramatic mismatch between the dynamical mass and the observable mass of the Coma cluster requires a viable explanation. Despite the rough estimations and simplifying assumptions in the preceding discussion, modern examinations of the Coma cluster uphold a substantial mass discrepancy ([Colless and Dunn, 1995](#)) reinforcing the need for dark matter as a plausible explanatory model.

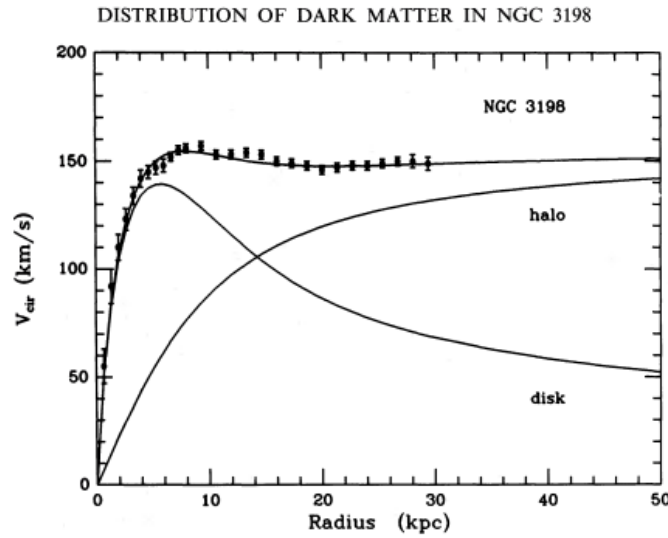
Modern techniques, like gravitational lensing, offer additional evidence for this observed mass discrepancy ([Kubo et al., 2007](#)). Gravitational lensing occurs when the light path from a distant source is deflected due to the gravitational field of a foreground mass, termed the lensing mass. The amount of this deflection, or the deflection angle,  $\theta$ , is directly proportional to the total mass of the lens, denoted as  $M_{\text{lens}}$ , such that  $\theta \propto \sqrt{M_{\text{lens}}}$ . Lensing mass estimates, unlike the Virial theorem mass estimates, do not require the assumption that the system is in dynamical equilibrium. This independence from equilibrium conditions allows for more accurate mass determinations in systems where dynamical equilibrium cannot be assured. From observations of the lensing mass, its baryonic content can be estimated and this results in a mismatch between the baryonic mass and the total lensing mass. This contemporary approach corroborates the existence of a missing mass and points to the necessity for dark matter as a phenomenological explanation.

**Evidence In Galaxies:** A significant indicator of the necessity of dark matter lies in the study of galaxy rotation curves of spiral galaxies. These are graphical representations of the rotational velocities of baryonic matter as a function of their distance from the galactic centre as highlighted in [Figure 1.2](#). A spiral galaxy is a type of galaxy characterised by a rotating thin disk of baryonic matter, with arms that spiral outward from a dense, central bulge. An example is displayed in [Figure 1.1](#). Spiral galaxies are particularly suitable for studies of gravitational potential because they are rotationally supported, meaning the bulk of their kinetic energy is in the form of rotational motion. This makes their constituent stars and gas effective tracers of the underlying gravitational potential. In practice, rotational velocities are typically measured using spectroscopy of 21cm neutral hydrogen ( $\text{H}_I$ ), the photon emitted when the  $\text{H}_I$  spin flips. This is because  $\text{H}_I$  is dynamically cold, so its velocity dispersion is typically small compared to its rotational velocity in high mass galaxies. Thus, the line of sight velocity can be measured from the Doppler shift of 21cm  $\text{H}_I$ .  $\text{H}_I$  also typically follows circular orbits which reduces complications that can arise when handling elliptical orbits. Furthermore, it typically extends out far beyond the optical range of galaxies, allowing to trace the gravitational poten-

tial out to large radii. This last detail is important because, from observations, most baryonic mass is concentrated in the centre of the galaxy. Thus, if dark matter were not present within galaxies, a signature Keplerian decline in velocity at large radii would be expected. This decline can be derived by balancing gravitational and centripetal forces, given as

$$\frac{mv^2(r)}{r} = \frac{GMm}{r^2} \implies v(r) = \sqrt{\frac{GM(r)}{r}} \quad (4)$$

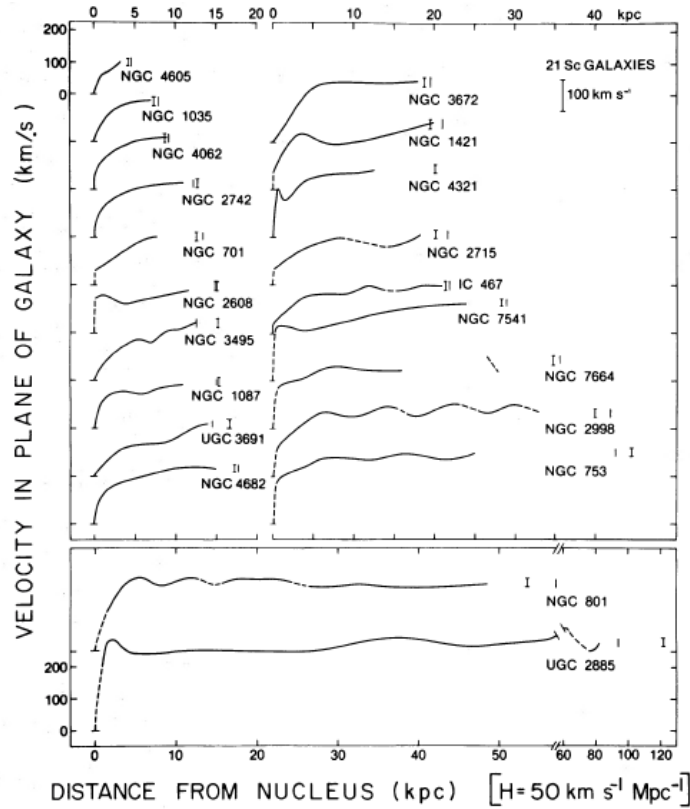
where  $r$ ,  $G$ ,  $M(r)$  and  $m$  are the radial distance from the galactic centre, the gravitational constant, the enclosed mass as a function of radius and the mass of a test particle, respectively. It should be noted that, for a spiral galaxy, equation 4 is not entirely accurate, as a spiral galaxy is not spherically symmetric. However, at large radii, it is approximately qualitatively correct.



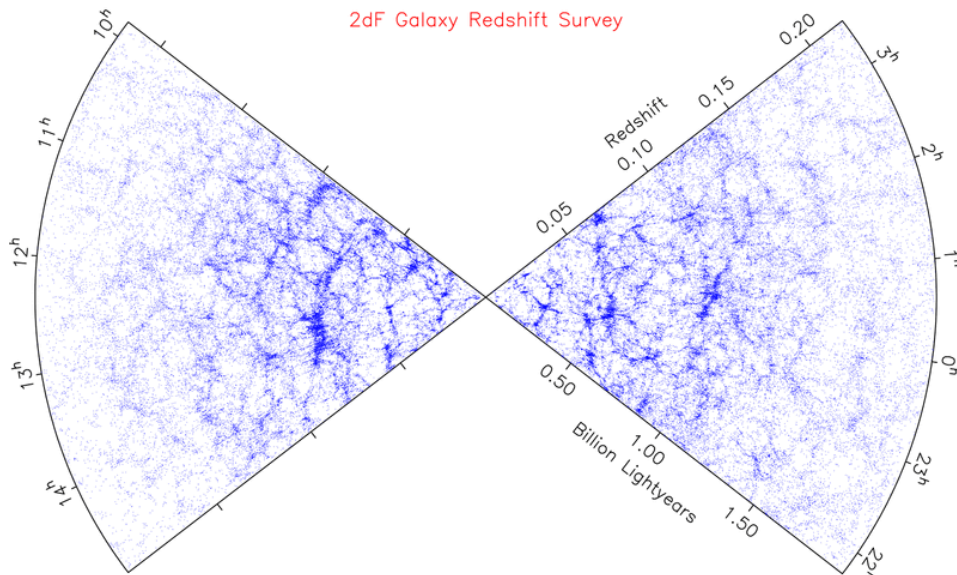
**Figure 1.2:** The rotation curve for the spiral galaxy NGC 3198 studied by [Van Albada et al. \(1985\)](#) is depicted above. Black markers indicate measured rotational velocities with associated error bars. The "disk" curve estimates the velocity contribution from the galaxy's baryonic matter, while the "halo" curve represents the unaccounted for velocity contribution attributed to dark matter.

Figure 1.3 shows the rotation curves of 21 spiral galaxies ([Rubin et al., 1980](#)). Although, the observable stellar mass of disk galaxies drops off quickly at large radii, none of the galaxies show a significant decline in velocity at large radii. For galaxies with data extending to large radii, their rotation curves flatten. This feature is observed in most spiral galaxies. Equation 4 suggests that a constant velocity at large radii indicates that  $M(r) \propto r$  or equivalently the mass density  $\rho(r) \propto r^{-2}$ . Such observations suggest there must be a significant amount of matter distributed throughout the galaxies, extending out beyond the optical range. This underscores the necessity for dark matter.

**Evidence In Cosmology:** Indirect evidence for dark matter can be discerned from understanding the formation of the large scale structure in the universe. Galaxy redshift surveys and measurements of the cosmic microwave background (CMB) are among the most effective tools available to understand this. Galaxy redshift surveys, such as the one depicted in Figure 1.4, map the spatial distribution of galaxies in the universe. Because light from more distant galaxies has taken longer to reach us, these surveys effectively serve as temporal probes, and thus provide insight into the evolution of cosmic structure formation. On the other hand, the CMB provides a snapshot of the state of the universe



**Figure 1.3:** Above is a figure adapted from a pioneering study conducted by [Rubin et al. \(1980\)](#). They studied the rotation curves of 21 spiral galaxies which are collected in the plot above. Many of the galaxies were observed to have an increasing rotational velocity at the edge of the optical range.



**Figure 1.4:** Wedge plot from the 2-degree Field Galaxy Redshift Survey (2dFGRS) ([Colless et al., 2001](#)), an observational campaign aimed at measuring the redshifts of galaxies to map their three-dimensional distribution in space. Each dot represents a galaxy; the redshift range shown here traces the evolution of cosmic structure formation from approximately 2 Gyr ago to the present day.

380,000 years after the big bang, during the era of recombination at redshift  $z_{\text{rec}} = 1100$ . This epoch marks the last significant interaction of CMB photons with baryonic matter. With its near-perfect black body spectrum, the CMB indicates that the early universe was in thermal equilibrium when it consisted of a hot, dense plasma of coupled baryons and photons. The anisotropies in the CMB, as highlighted in Figure 1.5, are temperature fluctuations on the order of  $\frac{\Delta T}{T} = 10^{-5}$  and represent over-densities and under-densities in the energy distribution of the early universe. These properties are significant as they set the initial conditions for the evolution of the universe. Given that photons and baryons were coupled before recombination, the temperature fluctuations in the CMB serve as a proxy for the density fluctuations of baryons at  $z_{\text{rec}}$ .

The initial density fluctuations can be defined as

$$\delta(\mathbf{r}, t) = \frac{\rho(\mathbf{r}, t) - \bar{\rho}(t)}{\bar{\rho}(t)} \approx 10^{-5}, \quad (5)$$

where  $\bar{\rho}(t)$  is the mean matter density at time  $t$  and  $\rho(\mathbf{r}, t)$  is the matter density at time  $t$  and position  $\mathbf{r}$ . These fluctuations evolve over time due to gravitational instability. Overdense regions see an increase in density and underdense regions see a decrease. Unlike a static universe where perturbations would grow exponentially under gravitational instability, the expansion of the universe suppresses the growth of these fluctuations. As a result, their growth is typically proportional to the scale factor.

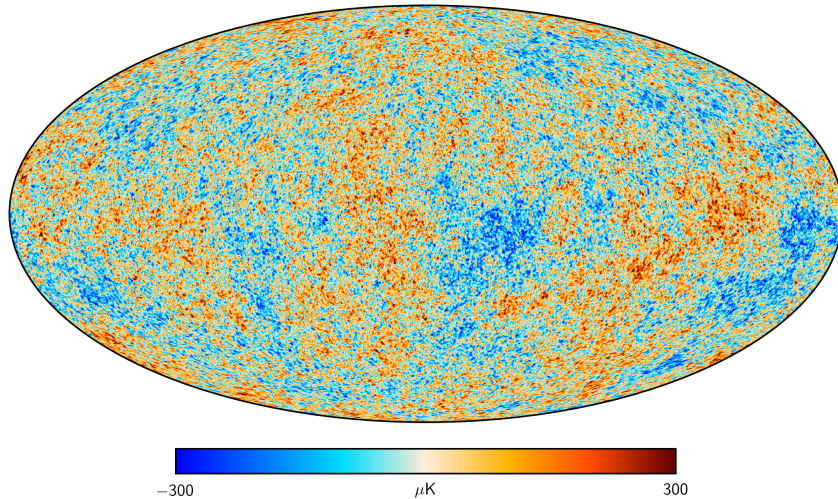


**Figure 1.5:** Temperature fluctuations of the CMB, which has a black body temperature of  $T = 2.726\text{K}$ . The observed temperature fluctuations are on the order of  $\frac{\Delta T}{T} = 10^{-5}$ . Image credit: ESA and the Planck Collaboration (Adam et al., 2016).

The scale factor  $a(z)$  describes the evolution of distances between comoving points in the universe. In comoving coordinates, a type of coordinate system where the position of an object is fixed if the object moves only along with the expansion of the universe, the actual physical distance is given by  $R = a(t)r$ , for a fixed comoving distance  $r$ . The scale factor is related to redshift as

$$a(z) = \frac{1}{1+z}. \quad (6)$$

Since  $\delta \propto a(z)$ , it follows that the expected amplitude of fluctuations, evolved from CMB fluctuations to present day,  $z_0 = 0$ , is given by

$$\delta_0 \propto \delta_{\text{rec}} \frac{a(z_0)}{a(z_{\text{rec}})} \approx 10^{-2}. \quad (7)$$

However, at present day  $\delta > 1$  on the scale of galaxy clusters; this implies that non-linear growth must have occurred for  $\delta$  to have reached such a magnitude. This is essential for overdense regions to decouple from the expanding universe and undergo faster, non-linear growth, eventually forming structures like galaxies.

To bridge the gap from the density fluctuations inferred from the CMB to the large-scale structures observed today, the role of dark matter is crucial. Unlike baryonic matter, whose gravitational collapse is counteracted by radiation pressure early on, dark matter is free to cluster, creating gravitational wells. By  $z_{\text{rec}}$ , these dark matter overdensities have started to significantly evolve, acting as a gravitational scaffold for baryonic matter to fall into, cool, and form stars.

It is important to note that the anisotropies in the CMB primarily reflect fluctuations in the baryonic matter density at  $z_{\text{rec}}$ , not those in dark matter. During the era leading up to recombination, photons were strongly coupled to baryons, making the CMB a sensitive probe of baryonic density variations at that time. However, because dark matter does not interact with photons in the same way, its overdensities are not directly imprinted in the CMB. Due to this differing interaction, fluctuations in dark matter at the time of the CMB can already be much larger than those of baryons.

Consequently, in a dark matter-dominated universe, small clumps of dark matter coalesce into larger structures known as dark matter halos. These halos then expedite the process of baryonic matter accretion, laying the groundwork for the rapid formation of galaxies and other large-scale structures.

This property of dark matter is a significant reason against the argument that dark matter is composed of baryons, as the latter remain coupled to the radiation longer due to their interaction with photons. Baryonic matter could not create the early potential wells needed to catalyze structure formation, as it would still be "washed out" by the radiation pressure at these early epochs. Such interaction with radiation consequently hinders the growth of significant density perturbations, making it impossible to form galaxies as observed today without the presence of non-baryonic dark matter.

## 1.2 Candidates of Dark Matter Particles

Given that empirical data necessitates dark matter, then the obvious question is what is dark matter? Two main categories of candidates can be identified: baryonic dark matter and non-baryonic dark matter.

### 1.2.1 Baryonic Dark Matter

Baryonic dark matter could consist of astronomical objects that emit minimal light, such as brown dwarfs, white dwarfs, neutron stars, small black holes, and planets. However, the mass contribution from planets is relatively insignificant compared to the other astronomical objects. If these objects contribute to the unaccounted mass in galaxies, then they need to be located beyond a galaxies' optical range, in the galactic halo, in order to explain flat rotation curves. Collectively, such astronomical objects in the halo are referred to as Massive Compact Halo Objects (MACHOs).

[Paczynski \(1986\)](#) proposed a method to investigate the existence of MACHOs as potential dark matter candidates in the Milky Way's halo. His proposal centered around the concept of gravitational microlensing, whereby the flux of a distant light source varies due to the gravitational lensing effect of MACHOs in the galactic halo as illustrated in [Figure 1.6](#). [Paczynski \(1986\)](#)'s analysis showed a relationship between the lensing mass (MACHO) and the variation time as  $M_{\text{MACHO}} \propto t_{\text{var}}^2$ . Additionally, he posited that the number density of MACHOs in the galactic halo should be proportional to the frequency

of lensing events. Consequently, by analysing the light curves of a sufficiently large sample of sources, a statistical framework could be developed to estimate the abundance of MACHOs in the Milky Way's halo.

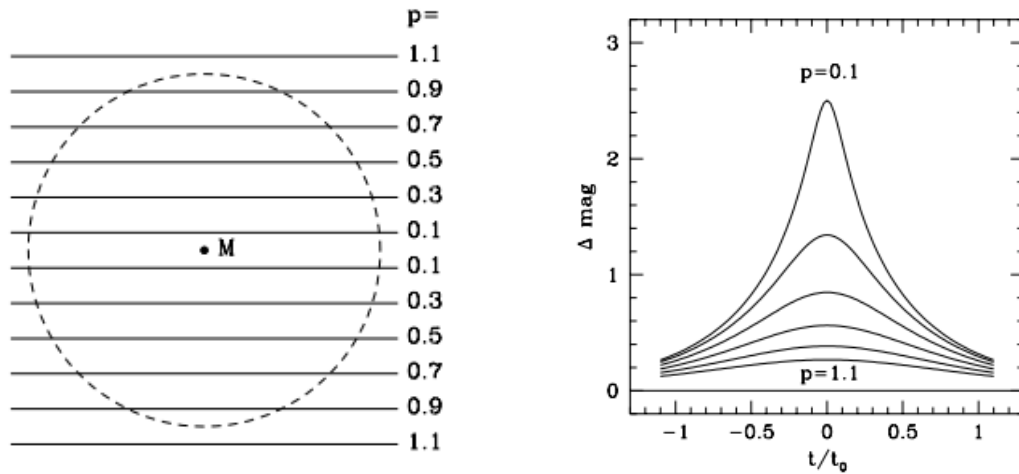


**Figure 1.6:** The geometry of a gravitational microlensing event is shown in the left panel (Paczynski, 1996). In this setup the lensing mass (MACHO) is stationary and twelve possible trajectories of a background source are represented by horizontal lines, each labelled with a dimensionless impact parameter,  $p$ . The right panel highlights the variation in the magnification (and therefore flux), of a background star due to the gravitational lensing of a MACHO as a function of time for various values of the impact parameter.

During the 1990s, both the MACHO and EROS collaborations undertook extensive surveys in search of lensing events attributable to MACHOs within the galactic halo. The MACHO collaboration identified approximately 20 such events, each corresponding to masses within the range  $0.15M_{\odot} \leq M_{\text{MACHO}} \leq 0.9M_{\odot}$ . These lensing events implied that a fraction  $f < 0.2$  of the halo mass might be attributed to MACHOs (Alcock et al., 2000). This fraction falls well below the expected contribution from dark matter. Subsequent analysis even questioned the validity of some of these lensing events (Popowski et al., 2003).

On the other hand, the EROS collaboration established even stricter constraints on the MACHO parameter space and set an upper bound on the fraction of dark matter that MACHOs could constitute (Tisserand et al., 2007). Specifically, they ruled out MACHOs as the predominant component of galactic dark matter for the mass range  $0.6 \times 10^{-7}M_{\odot} \leq M_{\text{MACHO}} \leq 15M_{\odot}$ . They determined limits of  $f \leq 0.04$  for  $10^{-3}M_{\odot} \leq M_{\text{MACHO}} \leq 10^{-1}M_{\odot}$  and  $f \leq 0.1$  for  $10^{-6}M_{\odot} \leq M_{\text{MACHO}} \leq 1M_{\odot}$ . Consequently, while MACHOs could potentially account for a minor fraction of galactic dark matter, they have been dismissed as a primary dark matter candidate.

Despite the empirical findings regarding MACHOs, it is primarily cosmological arguments which exclude baryonic matter as a viable dark matter candidate. As touched upon in the preceding subsection, baryonic matter, including MACHOs, encounter inherent limitations in this regard. In the early universe, baryonic matter remained tightly coupled to radiation up until the era of recombination. This interaction hampered the formation of early potential wells required for structure formation. Consequently, baryonic matter alone would not suffice for the growth of significant density perturbations, making it unsuitable for explaining the observed formation of galaxies without the presence of non-baryonic dark matter.

### 1.2.2 Non-Baryonic Dark Matter

Non-baryonic dark matter postulates the existence of new elementary particles that could account for dark matter. These candidates necessitate extensions and variations of the standard model of particle physics. Such particles can be broken into three categories dependent on their mass: hot, warm, and cold dark matter.

**Hot Dark Matter (HDM):** HDM particles are extremely light (eV scale) and relativistic. HDM candidates include axinos and gravitinos, which arise from extensions of the standard model of particle physics that introduce supersymmetry. In HDM cosmological models, the small-scale fluctuations observed in the CMB are washed out due to the free streaming of relativistic dark matter particles. This suggests that in an HDM-dominated universe, structure formation would proceed in a "top-down" manner, with the largest structures (superclusters of galaxies) forming first and then fragmenting into smaller structures. This occurs because HDM cannot be confined within small scales due to its relativistic nature; thus, large-scale structure formation can only proceed if the overdensities of dark matter in the early universe were extremely large, implying that the initial dark matter halos were also extremely large.

However, observations from galaxy redshift surveys suggest that structure formation proceeds in a "bottom-up" manner; smaller objects (subgalactic systems) form first and then aggregate into larger structures. This process is referred to as hierarchical structure formation. Consequently, while HDM particles may be suitable for accounting for the missing mass in large-scale structures like galaxy clusters, they fall short as suitable candidates on the smaller scales of individual galaxies and their rotation curves.

**Warm Dark Matter (WDM):** WDM is a particle with a mass on the keV scale. In a WDM-dominated universe, the particles could be warm enough to dampen some small-scale fluctuations without completely washing them out. This would lead to a reduction in small scale structure and would allow for larger structures to evolve earlier. WDM cosmological models are an active area of research.

**Cold Dark Matter (CDM):** CDM comprises heavy (GeV scale), non-relativistic particles. In CDM cosmological models, the significant mass of these particles facilitates the formation of small-scale overdensities, leading to a "bottom-up" approach in structure formation. As a result, in a CDM-dominated universe, the oldest structures to form are subgalactic in size, which subsequently coalesce to form larger structures such as superclusters of galaxies. This is corroborated by observations from galaxy redshift surveys (Colless et al., 2001), and this success contributes to the widespread acceptance of CDM within the prevailing cosmological framework.

The favoured candidate for CDM falls under the category of Weakly Interacting Massive Particles (WIMPs), which are predicted under many extensions of the standard model of particle physics, such as supersymmetry (Baer et al., 2016). However, WIMPs have been losing favour as experiments continue to rule out large portions of their parameter space (Arcadi et al., 2018). Other candidates like axions are gaining attention in this context. These particles should interact with baryonic matter primarily through gravity and the weak nuclear force. It is these very properties that allow dark matter to decouple from radiation earlier than baryonic matter in the early universe, thereby facilitating the formation of gravitational wells essential for accelerating structure formation.

## 1.3 Structure Formation Simulations Based on Cold Dark Matter

At this point, it would be prudent to note that the prevailing cosmological model, known as  $\Lambda$ CDM, assumes the validity of Einstein's general relativity and posits that dark matter is cold (hence, the CDM in  $\Lambda$ CDM). In this model,  $\Lambda$  represents the cosmological

constant, a term introduced by Einstein that is now associated with dark energy.<sup>2</sup> This project focuses on the role of dark matter within this framework, and the physics involved is governed by classical mechanics.

Given this context, competing cosmological models may incorporate WDM or HDM. N-body numerical simulations have become indispensable for distinguishing the predictions of structure formation among different cosmological models and for comparing these models with observations. This necessity arises because the dynamical complexity of structure formation on a cosmological scale exceeds the capabilities of analytical tools. In particular, dark matter-only (DMO) simulations are often used to investigate the evolution of structure formation and the properties of dark matter halos. This is a valid simplification for most purposes given that the ratio of dark matter to baryonic matter is approximately 5.25 (Aghanim et al., 2020).

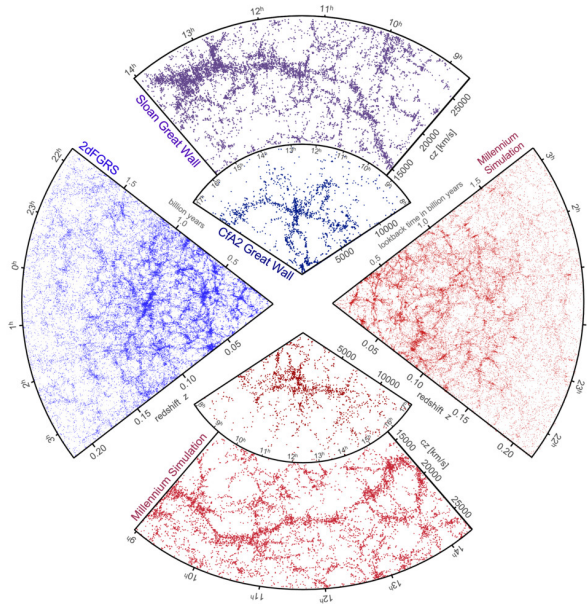


**Figure 1.7:** The wedges above illustrate how the DMO simulations using the  $\Lambda$ CDM model resemble the structures in the nearby universe. The left and upper blue wedges are galaxy redshift surveys carried out by the 2-degree Field Galaxy Redshift survey (Colless et al., 2001) and the Sloan Digital Sky Survey respectively (Gott III et al., 2005). The upper inner wedge is the pioneering galaxy redshift survey carried out by the Centre for Astrophysics (Geller and Huchra, 1989). The lower and right wedge are mock galaxy redshift surveys obtained from the galaxy distributions of the DMO Millennium simulation (Springel et al., 2005), based on the  $\Lambda$ CDM cosmological model. The mock galaxy redshift surveys were chosen from a set of random mock redshift surveys of the Millennium simulation such that they had a similar structure to the real galaxy redshift surveys in order to highlight that the simulations using  $\Lambda$ CDM cosmology can statistically reproduce the large scale structure observed in the universe today. This image was adapted from Springel et al. (2006)

In an N-body DMO simulation, the universe is typically represented as a cubic volume with periodic boundary conditions, chosen to reflect scales where the universe appears homogeneous and isotropic. Modern simulations can trace more than  $10^{10}$  particles, where each particle represents a macroscopic body of dark matter with mass,  $M$ , as tracing microscopic particles is neither possible or necessary. A typical mass range for dark matter particles used in DMO simulations is approximately  $\log(M/M_{\odot}) \in (7, 10)$  (Angulo et al., 2012; Boyle-Kolchin et al., 2009). The initial conditions of the simulation are set in the very early universe where each simulation begins with a distribution of dark matter particles subject to the constraints of the cosmological model being used.

<sup>2</sup>For further details on  $\Lambda$  and its implications, refer to standard cosmology texts.

The simulation then calculates the time and spatial evolution of the mock universe by integrating the particle equations of motion forward in time. These simulations detail the step-by-step evolution of structure formation, allowing models to make specific predictions about structure development which can then be compared to the observable universe or other models.

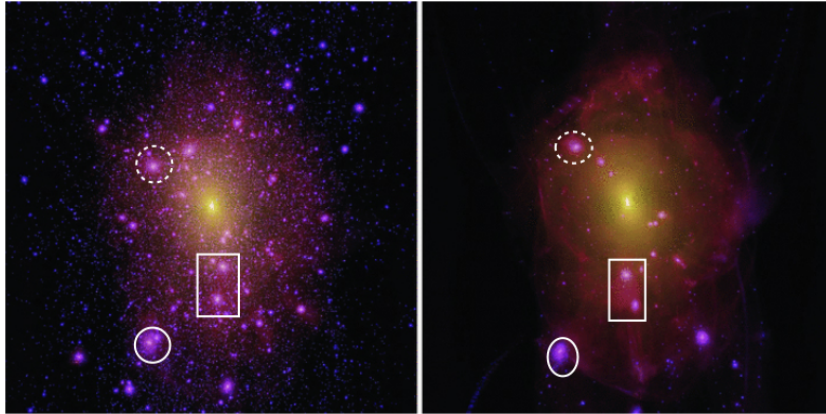


**Figure 1.8:** Comparison of dark matter halos from two N-body DMO simulations taken from a study conducted by Lovell et al. (2012). The left panel depicts a CDM halo, while the right showcases a WDM halo. Both simulations started with closely matched initial dark matter distributions. However, the power spectrum, which determines the amplitude of density fluctuations on all scales, was adjusted to dampen small scale fluctuations in the WDM model. Notably, the  $\Lambda$ CDM model exhibits more substructure than its WDM counterpart. Despite their apparent differences and an evolution timeline spanning the age of the universe, both halos remarkably exhibit similar characteristics in some of the larger substructures, as indicated by the overlaid markings.

As an illustrative case, Figure 1.7 juxtaposes galaxy redshift surveys with mock galaxy redshift surveys derived from the Millennium simulation, rooted in the  $\Lambda$ CDM cosmological model. Notably, there's a remarkable congruence between the mock and actual surveys concerning the evolution of large-scale structures, consistent with the hierarchical assembly of structures observed in the universe.

DMO simulations based on the  $\Lambda$ CDM cosmological model are proven to effectively emulate large-scale structure evolution, but there are problems that arise on smaller scales. These differences between simulations and observations often serve as prominent areas of investigation in current research. For instance, the "missing satellites problem" refers to the significant discrepancy between the large number of low-mass dark matter halos predicted by CDM simulations and the observed number of dwarf satellite galaxies around Milky Way-like galaxies (Bullock, 2013). Part of the motivation to study WDM models is to find a solution to this problem.

Figure 1.8 displays a comparison of a DMO simulated CDM halo against its WDM counterpart. Both halos, initiated under closely matched conditions, with their divergence owing to the dark matter type. Each "blob" in the images correspond to a dark matter subhalo with the main halo being the central bright region. The WDM model predicts far less subhalo satellites of the main halo than its CDM counterpart, hinting at a potential resolution to the missing satellites problem. It is imperative, however, to remember that DMO simulations, by design, exclude baryonic physics components such as star formation and feedback mechanisms, which could also influence small-scale structural patterns.

## 1.4 Models of Dark Matter Halos

One of the fundamental properties of dark matter halos derived from DMO simulations, grounded in the  $\Lambda$ CDM framework, is that they seemingly exhibit a universal density profile. This profile remains consistent across varying masses and sizes when characterised by specific fitting parameters. Two significant models, the Navarro-Frenk-White (NFW) density profile (Navarro et al., 1996), and the Einasto density profile (Einasto, 1965), are relevant for this project.

### 1.4.1 NFW Profiles

A seminal study by Navarro, Frenk and White first identified a universal dark matter halo density profile within simulations, resulting in what is now widely recognised as the NFW profile (Navarro et al., 1996). The study included 19 simulated dark matter halos spanning 4 decades in mass range. They found that the density profiles of the 19 simulated halos could all be described by a mass density with the functional form

$$\rho_{\text{NFW}}(r) = \frac{\rho_s}{\left(\frac{r}{r_s}\right) \left(1 + \frac{r}{r_s}\right)^2}. \quad (8)$$

The scale density, denoted as  $\rho_s = 4\rho_{\text{NFW}}(r_s)$ , determines the density profile's amplitude. The scale radius,  $r_s$ , is best understood by looking at the logarithmic slope of the density profile which is given by

$$\beta(r) = -1 - \frac{2r}{r + r_s} \quad (9)$$

where it is evident that the scale radius is then the radius at which  $\beta = -2$ . Figure 1.9 depicts 4 simulated halos and the best-fits according to equation 8.

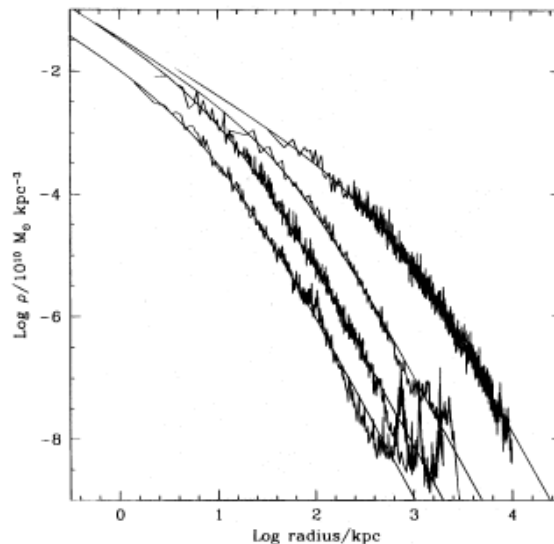


**Figure 1.9:** Spherically averaged density profiles of 4 simulated dark matter halos spanning 4 orders of magnitude in mass ranging from dwarf galaxies to galaxy clusters (Navarro et al., 1996). The solid smooth curves are the best-fit curves to the data using the NFW profile (equation 8).

### 1.4.2 Einasto Profiles

Following the seminal work by Navarro et al. (1997), Navarro et al. (2004) later suggested that DMO simulated halos could be better described by an alternative density profile

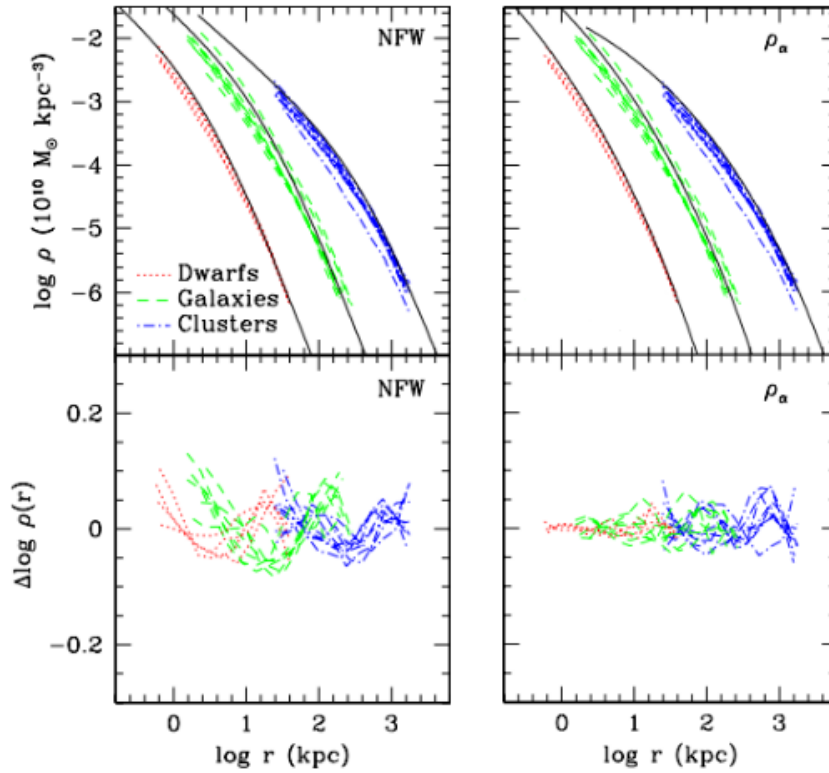


**Figure 1.10:** Spherically averaged density profiles of 19 simulated halos. These halos are classified into three mass groups: dwarf galaxies ( $10^{10}M_{\odot}$ ), galaxies ( $10^{12}M_{\odot}$ ), and galaxy clusters ( $10^{14}M_{\odot}$ ). In the top left and right panels, the solid lines are respectively representative of the expected profiles for the specified mass range, as described by the NFW profile (equation 8) and the Einasto profile (equation 10). The lower panels display the deviations of the simulated halos from the best-fit profiles of each halo, with a pronounced improvement observed for the Einasto model. Image adapted from Navarro et al. (2004)

known as the Einasto profile (Einasto, 1965). This can be mathematically depicted as

$$\rho_{\text{Einasto}}(r) = \rho_s \exp \left\{ -\frac{2}{\alpha_{\epsilon}} \left[ \left( \frac{r}{r_s} \right)^{\alpha_{\epsilon}} - 1 \right] \right\}. \quad (10)$$

This profile, like the previous, is expressed in terms of the scale radius and scale density, but incorporates an additional parameter,  $\alpha_{\epsilon}$ , termed the shape parameter, which determines the overall structure of the profile. Analysing the logarithmic slope of this profile yields

$$\beta(r) = -2 \left( \frac{r}{r_s} \right)^{\alpha_{\epsilon}}. \quad (11)$$

Here, consistent with NFW profile, the scale radius is also the radius at which  $\beta(r) = -2$ .

In Figure 1.10, the universality of both the NFW and Einasto profiles is highlighted based on the analysis of 19 simulated dark matter halos, as reported by Navarro et al. (2004). Across varying mass ranges, the data appear to be adequately described by both profiles. The lower panels show the deviations from the best-fit for each profile as a function of radius. Using this as a metric to quantify the quality of fit, the Einasto profile offers a roughly 10% better fit to the data than the NFW profile. This increased accuracy might be expected, considering the additional free parameter inherent to the Einasto model. For each dark matter halo, Navarro et al. (2004) determined that the best-fit Einasto shape parameter fell between 0.122 and 0.219, with an average value of  $\alpha_{\epsilon} = 0.172$ .

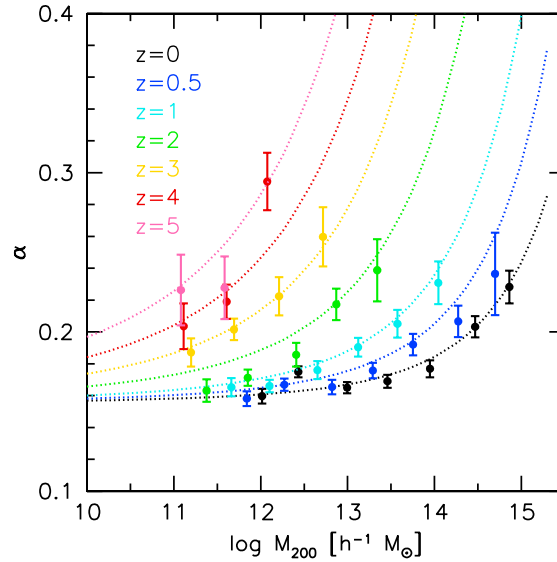


**Figure 1.11:** The redshift evolution of the Einasto shape parameter as a function of halo mass resulting from study by [Dutton and Maccio \(2014\)](#)

Further investigations into the Einasto profile, using DMO simulations, have provided constraints on the behaviour of  $\alpha_\epsilon$  in relation to halo mass. One notable study, encompassing a spectrum of halo masses from dwarf galaxies to galaxy clusters, is illustrated in Figure 1.11 ([Dutton and Maccio, 2014](#)). This study depicts the evolution of  $\alpha_\epsilon$  and its functional dependence on halo mass. The galaxies relevant to this project are located at redshift  $z = 0$ , and exhibit an approximate halo mass range of  $\log (M_{200}/M_\odot) \in (12, 14)$ . From the plot, it is evident that within this mass range,  $\alpha_\epsilon \approx 0.17$ .

### 1.4.3 Core-Cusp Problem

Central to this project is the so called core-cusp problem; a tension between observations in dwarf galaxies and DMO simulations regarding the innermost slope of the density profile of dark matter halos. A cored profile is a profile whose central density is finite whereas a cuspy profile is a profile where density seemingly increases without bound towards the centre. This tension can be characterised using a power-law representation  $\rho \approx r^{-\gamma}$ , where  $\gamma$  represents the innermost region of the logarithmic slope of the density profile. A cored profile corresponds to  $\gamma = 0$ , while  $\gamma = 1$  indicates a distinctly cuspy profile.

DMO simulated halos consistently exhibit a cuspy central mass density. This property was first derived by [Dubinski and Carlberg \(1991\)](#) through analytical fits of the simulated halos. The NFW profile is a cuspy halo model ( $\gamma = 1$ ), evident from equation 9 in the limit as  $r \rightarrow 0$ . The Einasto model is inherently a cored profile when  $\alpha_\epsilon > 0$  evidenced from equation 11. However, when  $\alpha_\epsilon \approx 0.1$ , the approach to a finite central density is so gradual that with the current numerical methods, the profile seems to exhibit a cusp. Essentially, the shape parameter acts as an indicator of the cusp's prominence in the profile with  $\alpha_\epsilon \approx 0.1$  appearing very cuspy whereas  $\alpha_\epsilon \approx 0.6$  is characteristically cored. Typically, DMO simulated halos fitted with the Einasto profile yield  $\alpha_\epsilon \approx 0.17$  ([Navarro et al., 2004](#)), indicating that they are seemingly cuspy.

Yet, cuspy dark matter halos are in stark contrast with the dark matter density profiles inferred from observed dwarf galaxy rotation curves. Analysis of their rotation curves suggests that the dark matter halos in which they reside have a central core,

described by  $\rho \approx r^0$ , leading to  $\gamma = 0$ . The parameter  $\gamma$  can be utilised to quantify the "cuspsiness" of a halo, with  $\gamma \geq 0.8$  representing a distinctly cuspy halo,  $\gamma \approx 0.2$  indicating a mild cusp and  $\gamma = 0$  indicating a cored halo.

Systematic effects in observational data have been proposed as potential explanations for the discrepancies observed between DMO simulations and real-world observations. Beam smearing, a consequence of the finite resolution of telescopes, is one such systematic effect that might give the illusion of a core-like behaviour in galactic rotation curves (De Blok et al., 1996). Historically, rotation curves were often derived from observations of the  $H_I$  line, which is detected using radio telescopes. These observations could potentially produce beam smearing effects that under-represent the true velocities. However, a significant improvement in spatial resolution can be achieved by observing the  $H_\alpha$  line, the emission line corresponding to the transition from the  $n = 3$  to  $n = 2$  energy level. This line is particularly effective in regions of galaxies with ongoing star formation, where the conditions to produce  $H_\alpha$  emission exist. While the  $H_\alpha$  line may not be prominent in the outermost regions of galaxies, due to limited absorption sources, it can be prolific nearer to the galactic centres where star formation is more active. This makes the  $H_\alpha$  line a suitable probe of the inner rotation curves. Importantly, observations using the  $H_\alpha$  line have corroborated those from the  $H_I$  line (McGaugh et al., 2001), suggesting that the core-like characteristic of dark matter halos in dwarf galaxy rotation curves is consistent across various observational methods.

The potential for enhanced resolution in simulations to reconcile discrepancies between theory and observations is another possible solution to the tension between observation and simulation. With the advancement of computational techniques and increased resolution, a broad spectrum of results has been obtained for the inner slopes of dark matter density profiles which lie in the range  $\gamma \in (0.7, 1.5)$  (Moore et al., 1999; Navarro et al., 2004). This range not only demonstrates the varied outcomes from distinct simulations but also emphasises the typical cuspsiness observed in simulated dark matter halos. Despite the advancements in both observational techniques and simulation resolution, the tension remains and is now known as the core-cusp problem. This presents another small-scale challenge to the  $\Lambda$ CDM model and it is the primary focus of this project.

It should be noted that a cuspy density profile is not a prediction of  $\Lambda$ CDM cosmology from first principles but rather it arises from the analysis of DMO simulations based on  $\Lambda$ CDM cosmology. As such the solution to the core-cusp problem could be found by further improving the resolution of observations or simulations. Alternatively, it could be that DMO simulation are not sufficient to model the formation of dark matter halos inferred from observation. As such the solution of the core-cusp problem could be found within the investigation of baryonic effects on dark matter halos.

## 1.5 Baryonic Effects on Dark Matter Halos

DMO simulations are instrumental for modelling the initial, self-supported halos but are limited in capturing the evolved structure of dark matter halos in actual galaxies. While baryonic effects in simulations are negligible when replicating observations on cosmological scales, they become significant at the galactic level and as such introducing baryonic physics offers a resolution to the core-cusp problems.

During galaxy formation, dark matter halos accrete baryons into their gravitational potential wells. These baryons cool, form stars, and as galaxies evolve, are partially re-ejected into the interstellar medium due to activity from stars and black holes. This accretion and subsequent ejection of baryons are critical processes that modify the structure of the halo. Specifically, these processes lead to two primary mechanisms influencing

the structure of dark matter halos during galaxy evolution: feedback and adiabatic compression

**Feedback:** Feedback refers to processes that redistribute baryonic matter into the interstellar medium. This change in the distribution of baryonic matter affects the galaxy’s gravitational potential well, consequently altering the dark matter distribution within the galaxy. A notable feedback mechanism are supernovae, which can potentially transform a cuspy halo into a cored one (Di Cintio et al., 2014).

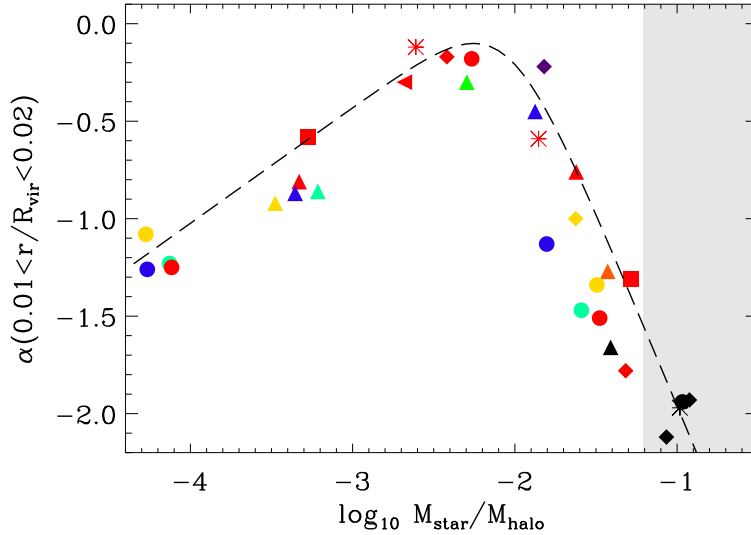


**Figure 1.12:** Relationship between the dark matter halo’s inner logarithmic density slope, denoted here as  $\alpha$ , and the stellar-to-halo-mass ratio (Di Cintio et al., 2014). The coloured markings correspond to 31 simulated galaxies incorporating supernovae feedback processes in their evolution.

A supernova is the explosive death of a star, triggered by gravitational collapse or thermonuclear processes, resulting in the ejection of stellar material and a tremendous release of energy into the surrounding space. As a feedback mechanism it is sufficient to heat and expel gas from the central regions of galaxies. This redistribution of baryonic matter has been shown to flatten the central cusp of the dark matter density profile in galaxies, as highlighted in Figure 1.12. The plot shows a tight relationship between the the inner logarithmic slope and the stellar-to-halo-mass (SHM) ratio of galaxies. For lower values of the SHM ratio, the fraction of stellar mass is too small for the feedback mechanism to modify the dark matter distribution, and the halos retain their cuspy profiles. Notably as the SHM ratio increases, the feedback becomes strong enough to flatten the cusp with a sweet spot around  $\log(M_*/M_{\text{halo}}) = -2.3$ . For galaxies with a large SHM ratio this flattening diminishes. This is because the gravitational well is too deep for the feedback energy to overcome, and the gravitational well is so deep that it has the effect of contracting the halo such that the halo becomes cuspier. However, Di Cintio et al. (2014) noted that the mass range at which the density profiles become cuspier are also the halo mass range at which active galactic nucleus (AGN) become significant and they have suggested that simulations incorporating AGN feedback could possible flatten the cusp at this halo mass range.<sup>3</sup>

<sup>3</sup>An active galactic nucleus is the central region of a galaxy where an accreting supermassive black hole emits a large amount of electromagnetic radiation. This emission often outshines the entire galaxy and can influence its surrounding environment, affecting both star formation rates and intergalactic medium properties. The energetic outflows act as a feedback mechanism displacing central gas concentrations,

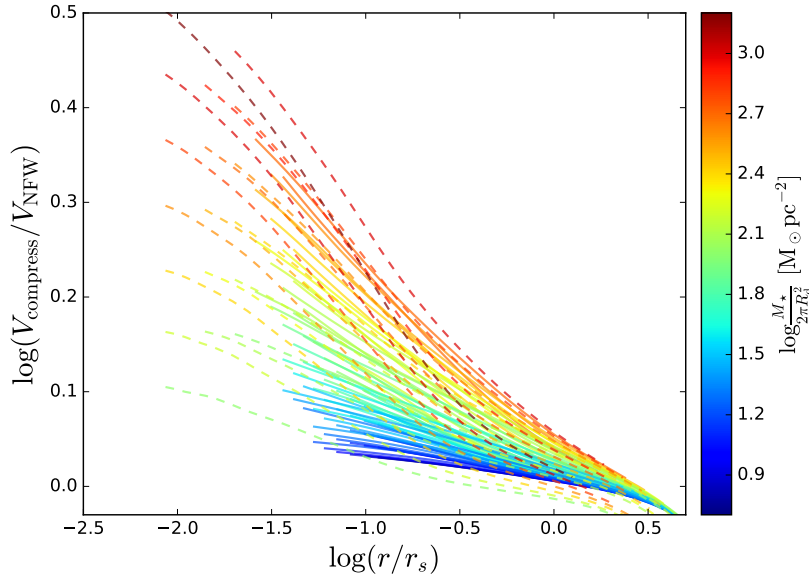


**Figure 1.13:** The figure illustrates the ratios of rotation velocities for compressed halos relative to their antecedent NFW halos. The study conducted by Li et al. (2022b) utilised data from 80 model galaxies, each coloured by surface mass density.

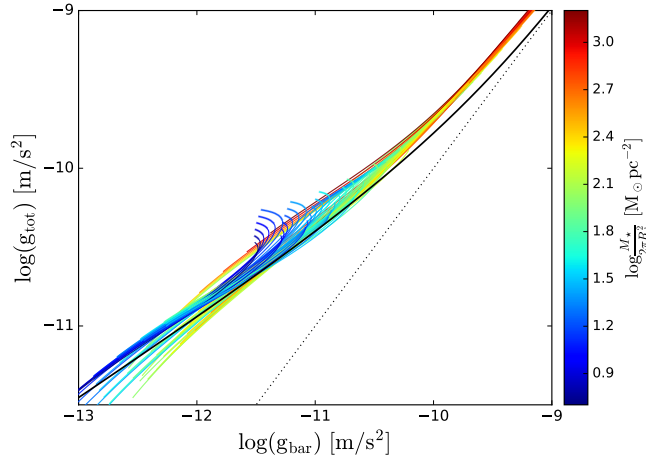
**Adiabatic Compression:** Adiabatic compression is the gravitational response of dark matter halos to baryons accreted during the galaxy formation process. As gas moves toward the central regions of a galaxy, the increasing matter density can deepen the gravitational well. This invokes a contraction of the dark matter halo in response, amplifying the density in the innermost regions. This effect, often overlooked in numerical simulations that include baryonic physics, was systematically investigated by Li et al. (2022b). In their study they created a sample of 80 model galaxies using the NFW profile as the basis for the dark matter component. Subsequently they numerically computed the adiabatic compression of dark matter NFW halos in response to the growth of the baryonic component of the model galaxy.

Figure 1.13 displays the rotational velocity ratios for each compressed halo to its antecedent NFW halo from which it was derived under baryonic compression, plotted as a function of radius. The plots are coloured by their surface mass density, clearly showing that the innermost rotational velocities have increased between 10% for dwarf galaxies (bluer tones) and 300% for massive galaxies (redder tones). Given that velocity is proportional to the square root of the density, it is implicit that the density of the dark matter halos has increased across the entire sample, with the most pronounced effects in galaxies with greater baryonic content.

Figure 1.14 introduces the Radial Acceleration Relation (RAR), an empirical link between baryonic matter and galactic dynamics observed across a range of galaxy types. In this relation, the total radial acceleration at any given radius,  $g_{\text{tot}}$ , correlates with the radial acceleration attributable solely to the baryonic matter,  $g_{\text{bar}}$ . The black line in the figure represents the observed RAR from studies (McGaugh et al., 2016; Lelli et al., 2016), while the dotted line shows the line of parity between  $g_{\text{bar}}$  and  $g_{\text{tot}}$ . This relationship reveals that in high-acceleration regions—typically found in massive galaxies—the slope

---

which can indirectly affect the structure of a dark matter halo. Unlike supernovae, the influence of AGN feedback may be more localised due to its origination from the galactic centre.



**Figure 1.14:** The radial acceleration relation (RAR) is depicted for the 80 model galaxies analysed in the study by Li et al. (2022b), as illustrated in the preceding figure. Each galaxy is distinguished by its surface mass density, The black solid line represent the observed RAR (McGaugh et al., 2016; Lelli et al., 2016). The line of parity is shown as the dotted line.

is approximately 1, indicating that the inner dynamics of these galaxies are dominated by baryonic matter.

The figure also plots the RAR for the 80 model galaxies, which include the effects of baryonic compression on dark matter halos, as studied by Li et al. (2022b). These compressed dark matter halos are derived from NFW profiles, characterised by a density that decreases with radius following a  $r^{-3}$  relationship and thus for clarity regarding the plot's orientation, it is important to note that the lower acceleration range typically corresponds to larger radii, while higher accelerations are found at smaller radii. The plots corresponding to dwarf galaxies (bluer tones) exhibit 'hooks' where they bend upwards at smaller radii, deviating from the observed relation. Comparing these lower mass density model galaxies with their corresponding data in the previous figure reveals that their halos are the least impacted by baryonic compression, yet they diverge the most from the empirical relation. This discrepancy illustrates the core-cusp problem. These hook features suggest that an NFW halo, even before compression, dominates the central dynamics of low mass density galaxies, leading to larger total accelerations, and any compression effects only serve to increase dark matter dominance in central dynamics. Moreover, the plots indicate that when the effects of baryonic compression are included in models of massive galaxies (redder tones), these galaxies too begin to show deviations from the RAR in high-acceleration regions. This discrepancy indicates that once baryonic compression is accounted for in models of galaxy formation, the core-cusp problem may not be confined to a tension between dwarf galaxy observations and DMO simulations but may also include massive galaxies.

Following Li et al. (2022b)'s study, Li et al. (2022a) conducted a comprehensive investigation into the effects of baryonic compression on dark matter halos using real-world observations. A novel aspect of this paper is that the baryonic distribution used to numerically solve the compression of the NFW halos was tailored to match the specific baryonic distribution of observed galaxies. The compressed dark matter halos were simultaneously incorporated into the rotation curve fitting procedure.

A rotation curve fit traditionally does not incorporate any baryonic effects on the dark matter halo. Usually, a rotation curve fit assumes a dark matter density profile, such as the NFW profile, and then searches the parameter space for the best fit. The left panel in Figure 1.15 shows an example of a conventional rotation curve fit that does

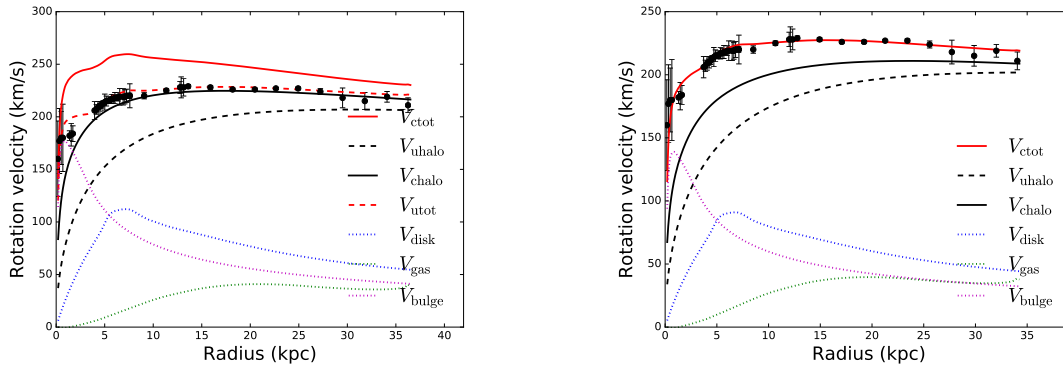


**Figure 1.15:** Left panel is a best-fit rotation curve, derived by Li et al. (2022a), neglecting the adiabatic contraction of the dark matter halo for the Galaxy UGC 06786 whereas the right panel is the best-fit rotation curve incorporating the baryonic compression of the dark matter halo during the fitting procedure. The black data points with error bars are the measured rotation curve. Blue and purple dotted curves denote the contribution to the rotation curve for the stellar disk and the bulge respectively, which have been adjusted to find the best-fit, while the green dotted curve corresponds to the gas contribution to the total rotation curve. The dashed black curve is the contribution of the best-fit NFW halo. The red dashed curve represents the quadrature sum of the baryonic and NFW dark matter halo contribution yielding the total velocity curve. The solid black curve shows the contribution to the rotation curve of a the corresponding compressed dark matter halo; derived from numerical solving the baryonic compression of the best-fit NFW dark matter halo for the given best-fit baryonic distribution. The red solid curve is the total velocity curve if the compressed dark matter halo were used instead of the NFW dark matter halo.

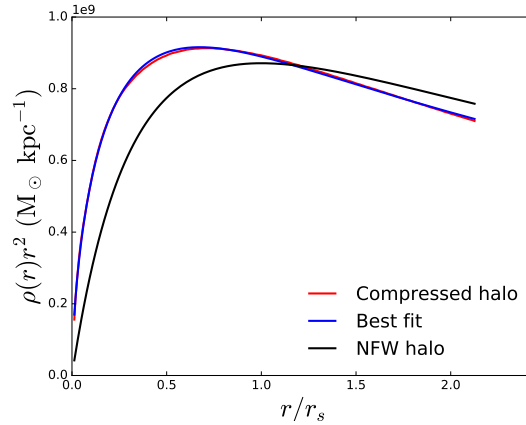
not incorporate adiabatic compression of the dark matter halo during the fitting process. The best-fit NFW halo contribution to the rotation curve is shown as the dashed black curve. The total best-fit velocity curve is the dashed red curve, which demonstrates that modelling the galactic dynamics using the NFW profile provides a reasonably good fit for the observable data.

For comparison, Li et al. (2022a) took the best-fit NFW halo and numerically solved its baryonic compression for the given mass distribution of the galaxy. The resulting velocity contribution for the compressed halo is shown as the solid black curve in the left panel of Figure 1.15, illustrating that the dark matter halo has been significantly modified. The solid red curve represents the total velocity curve had the NFW halo been first compressed according to the baryonic distribution in the galaxy. It is clear that this does not provide a suitable fit for the observable data. Neglecting the baryonic compression effect when fitting rotation curves clearly leads to a significant difference in the outcome.

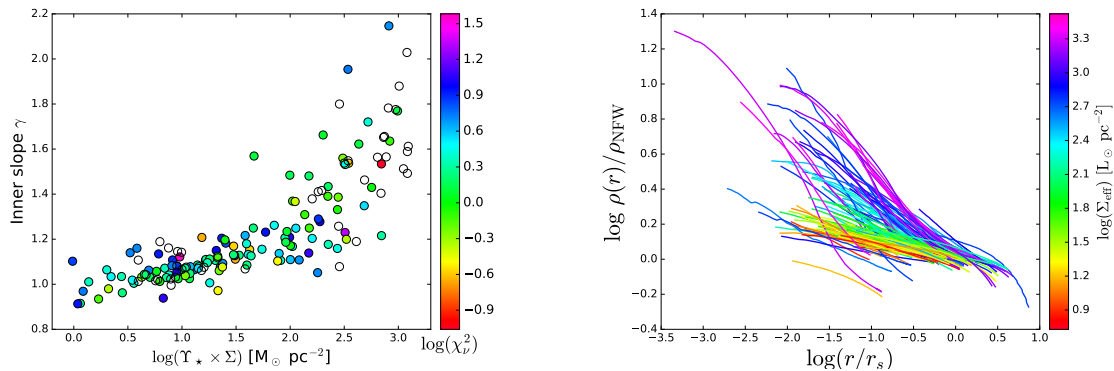
The right panel in Figure 1.15 shows the best-fit rotation curve for the same galaxy, except in this instance, the compressed dark matter halo, derived from the NFW profile, was used during the fitting procedure. To achieve the best-fit when incorporating the effect of baryonic compression on the dark matter halo, the contributions of both the disk and the bulge to the velocity curve—represented by blue and purple dotted lines, respectively—have been reduced compared to the uncompressed fit shown in the left panel.

Figure 1.16 illustrates the impact of baryonic compression on the structure of the dark matter halo. The blue curve is the parametric fit according to the so-called  $(\alpha, \beta, \gamma)$  model given by

$$\frac{\rho}{\rho_s} = \frac{1}{\left(\frac{r}{r_s}\right)^\gamma \left[1 + \left(\frac{r}{r_s}\right)^\alpha\right]^{(\beta-\gamma)/\alpha}} \quad (12)$$



**Figure 1.16:** The density profiles of the compression dark matter halo (red curve) and the NFW halo (black curve) from which it derives (Li et al., 2022a). The blue curve is a parametric fit to the compressed halo using a generalised dark matter halo model.



**Figure 1.17:** Left panel shows of the inner slope of the compressed halo of 125 galaxies derived in the study by Li et al. (2022a) plotted against the surface mass density colour coded by the rotation curve fit quality. Right panel shows the density ratio of the compressed dark matter halos to the NFW halos from which they were derived.

with  $\alpha$  fixed to unity. Note that the NFW profile is the same as the  $(\alpha, \beta, \gamma)$  model when  $(\alpha, \beta, \gamma) = (1, 3, 1)$ . By fitting the compressed halo using the  $(\alpha, \beta, \gamma)$  model, the inner slope  $\gamma$  can be used to quantify how much the inner structure of the original NFW halo ( $\gamma = 1$ ) has changed due to baryonic compression.

Li et al. (2022a) successfully incorporated baryonic compression in rotation curve fits for a sample of 125 galaxies. The inner slope of the compressed halos was determined using the parametric fit according to equation 12. The left panel of Figure 1.17 shows the inner slope of the resulting compressed halos for each of 125 galaxies as a function of the surface mass density. The NFW halo has an inner slope  $\gamma = 1$ , and it is clear that the inner slope increases with surface mass density. The effect is such that for the most massive galaxies the compressed dark matter halo become "super-cuspy".

Moreover, the right panel of Figure 1.17 plots the density ratios of the resulting compressed halos to the primordial NFW halo from which they were derived, colour-coded by their surface brightness. In almost every instance, an increase in inner density is observed, attributable to baryonic compression. For the most massive galaxies (blue and purple hues), the central density increases by up to tenfold, where primordial NFW halos were transformed into super-cuspy dark matter halos. This substantial increase in density results in a significant problem: these super-cuspy halos leave less room for baryons, consequently resulting in best-fit baryonic densities that are systematically

lower than those predicted by stellar population synthesis models (Schombert et al., 2019).<sup>4</sup>

Baryonic feedback is a potential solution to this problem, where feedback processes can expand the halo, allowing for more baryonic mass. Di Cintio et al. (2014) have shown, as evidenced in Figure 1.12, that stellar feedback processes can flatten a regular cusp in dwarf galaxies. However, Li et al. (2022a)'s findings demonstrate that to achieve baryonic densities consistent with predictions when modelling rotation curves incorporating baryonic compression, the feedback must be strong enough to transform a super-cuspy halo into a regular cusp in massive galaxies, thereby allowing more room for baryonic matter.

If feedback processes are not sufficient to expand a super-cuspy halo, then Li et al. (2022a)'s research indicates that a primordial cored halo model may be necessary for modelling massive galaxies, in order to achieve a best-fit baryonic density that agrees with the predictions of stellar population synthesis models (Schombert et al., 2019). A cored dark matter halo model would allow for greater baryonic density, which could then, under baryonic compression, transform the core into a regular cusp suitable for modelling the observed dynamics of massive galaxies. If modelling massive galaxies necessitates a cored primordial halo, this broadens the cusp-core problem to include massive galaxies.

The study by Li et al. (2022a) and its implications for the cusp-core problem serves as the primary motivation for this project. The objective is to incorporate baryonic compression into rotation curve fits using a subsample of the most massive galaxies examined by Li et al. (2022a). This project will, for the first time, employ the cored Einasto dark matter profile as the primordial halo. In the Einasto model, the shape parameter governs the cuspieness of the density profile, offering more flexibility than the NFW profile through its additional parameter. By leveraging this flexibility, the project aims to explore potential solutions to the problem identified by Li et al. (2022a).

The methodology involves numerically solving the baryonic compression of a dark matter halo to ensure the baryonic distribution used for the compression matches that of observed galaxies. The resulting compressed dark matter halo will then be incorporated into the rotation curve fitting procedure, followed by a comprehensive analysis of the outcomes.

---

<sup>4</sup>Stellar population synthesis aims to synthesise the spectral energy distribution (SED) of model galaxies from the combined radiative contributions of all stellar constituents. This synthesised SED is then compared with observational data to deduce the composition and properties of the galaxy's stellar population, despite the inability to resolve individual stars within these galaxies.

## 2 Method & Data

### 2.1 Adiabatic Contraction of Dark Matter Halos

#### 2.1.1 Methodology of Modelling Halo Contractions

Adiabatic processes, characterised by gradual changes, allowing systems to remain close to equilibrium, are pivotal in astrophysics. [Young \(1980\)](#)'s seminal work established a numerical model for such a process, specifically addressing the adiabatic growth of black holes. Central to Young's method is the conservation of adiabatic invariants, a concept derived from Hamiltonian mechanics. In a spherically symmetric system, these invariants are the radial action  $J_r$ , azimuthal action  $J_\phi$ , and polar action  $J_\theta$ . [Young \(1980\)](#) demonstrated that the distribution function (DF), when expressed in terms of these invariants, remains constant throughout adiabatic transformations of the system.

#### 2.1.2 COMPRESS: A Numerical Realisation of Adiabatic Contraction

The process of baryonic compression of a dark matter halo can be modelled as an adiabatic process. COMPRESS is a program that extends principle of Young's method to model the adiabatic compression of dark matter halos, in response to the incremental addition of baryonic matter to the system ([Sellwood and McGaugh, 2005](#); [Sellwood, 2014](#)). This program adapts [Young \(1980\)](#)'s approach with assumptions tailored to dark matter halos:

1. **Adiabatic and Spherical Symmetry:** It is assumed that the dark matter halo is adiabatic and spherically symmetric. These conditions enable the use of gravitational perturbative techniques to approximate changes in the halo arising from the incremental addition of baryonic matter.
2. **Adiabatic Invariants in Halo Dynamics:** The adiabatic invariants play a crucial role in evolving the dark matter halo as baryonic mass is introduced, affecting the gravitational potential and therefore the specific energy of the dark matter particles. The invariants,  $J_{r,n}(E_n, L) = J_{r,0}(E_0, L)$ ,  $J_\phi = L$ , and  $J_\theta = 0$ , correlate the initial state (subscript 0) with the state after the  $n$ -th iteration. The invariant azimuthal action is the angular momentum,  $L$ , of the dark matter particles while the energy of the dark matter particles is denoted by  $E$ . The polar action,  $J_\theta$ , is zero indicating the confinement of particle motion to a plane, a consequence of the system's spherical symmetry under a central force.<sup>5</sup>
3. **Invariant Distribution Function and Numerical Solution:** The conservation of the DF when written as a function of  $J_r$  and  $J_\phi$  simplifies the transition to the computationally convenient  $(E, L)$  space. This transition is critical in the numerical solution for the adiabatic compression of the dark matter halo. As the baryonic mass alters the gravitational potential, the dark matter particles' energy  $E_n$  changes. This new energy is deduced from the gravitational potential and adiabatic invariants, facilitating the update of the DF from  $f_0$  to  $f_n$  in response to the evolving system.

---

<sup>5</sup>The disk galaxies in this study do not exhibit spherical symmetry. However, this assumption used in COMPRESS was tested using N-body simulations, and the findings indicate that even a substantial disk's influence on dark matter halo geometry is minimal, validating the assumption of spherical symmetry as a first-order approximation ([Sellwood and McGaugh, 2005](#)).

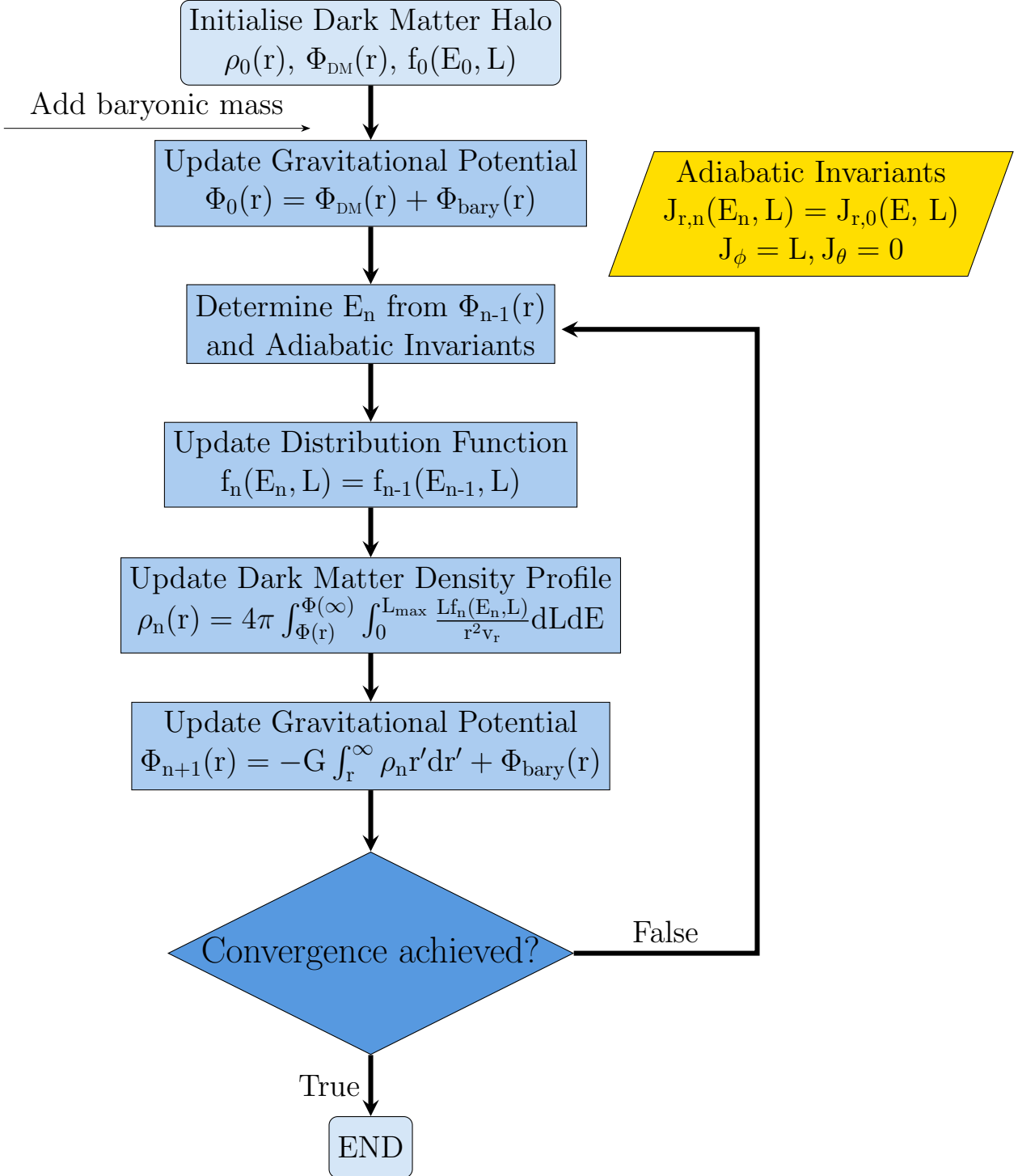


**Figure 2.1:** Flowchart illustrating the iterative procedure of Young’s Method as implemented by COMPRESS for the adiabatic contraction of dark matter halos. Starting with a dark matter halo characterised by its density  $\rho_0(r)$ , initial gravitational potential  $\Phi_{DM}(r)$ , and distribution function  $f_0(E_0, L)$ , the process sequentially updates the system’s gravitational potential to include the effects of an incrementally added baryonic component. Each iteration recalculates the dark matter particles’ energy based on the adiabatic invariants within the updated potential. The distribution function is then revised according to the new energy states, leading to an updated density profile  $\rho_n(r)$  and subsequent gravitational potential  $\Phi_n(r)$ . This iterative loop is repeated until the potential converges to a pre-defined level of consistency, signalling the achievement of a compressed dark matter halo that is in dynamical equilibrium with the additional baryonic distribution.

The procedure used in COMPRESS to numerically solve the baryonic compression of a dark matter halo is illustrated with a flowchart in figure 2.1. COMPRESS takes an initial dark matter halo density input and numerically solves the adiabatic compression of the dark matter halo in response to the addition of a baryonic component. The output is the density of a compressed dark matter halo, its velocity contribution to the galaxy rotation curve as well as the velocity contribution of the additional baryonic components to the rotation curve.

The great advantage of COMPRESS is its flexibility in specifying the distribution of baryonic matter; the resulting baryonic distribution can be tailored to match that of a real-world galaxy. This does not imply that the compressed dark matter halo will exactly match the observed galaxy’s dark matter halo. Nevertheless, incorporating the resulting compressed dark matter halo from the COMPRESS program into a rotation curve fitting procedure allows for a comparison of the best-fit compressed halo to its primordial antecedent. Comparing the inner slopes of both the uncompressed and compressed dark matter halos quantifies the magnitude of compression in response to the growth of the baryonic distribution.

### 2.1.3 Generating Initial halos

To employ the COMPRESS program effectively, initialising the DF of the primordial halos is crucial. The DF must be in equilibrium, characterised by a velocity distribution that prevents the halo from collapsing or dispersing while preserving the specific shape and characteristics of the underlying dark matter profile. In Li et al. (2022a)’s study on the effects of baryonic compression, they generated DFs based on the NFW profile. In contrast, this work employs Einasto profiles to model initial halos. COMPRESS includes a subroutine specifically for generating the DFs of primordial halos.

The DFs for the primordial halos are generated using the inverse Eddington formula, which computes a DF from a given density profile according to:

$$f(\mathcal{E}) = \frac{1}{\sqrt{8\pi^2}} \left[ \int_0^{\mathcal{E}} \frac{d^2\rho}{d\Psi^2} \frac{d\Psi}{\sqrt{\mathcal{E} - \Psi}} + \frac{1}{\sqrt{\mathcal{E}}} \left( \frac{d\rho}{d\Psi} \right)_{\Psi=0} \right] \quad (13)$$

where  $\Psi(r) = \Phi_0 - \Phi(r)$  and  $\mathcal{E} = \Psi - \frac{1}{2}|\mathbf{v}^2|$ .

The procedure begins with the calculation of the gravitational potential  $\Phi(\mathbf{r})$  using a dark matter density profile,  $\rho$ . Next, the velocity,  $\mathbf{v}$  for the dark matter particles are determined based on this potential, aligning them with the density profile. Finally, the DF is integrated out using derived potential and dark matter particle velocities. Employing the inverse Eddington formula with an Einasto profile results in a DF that accurately models a dark matter halo in dynamical equilibrium with a density that corresponds to an Einasto profile. For each shape parameter value of the Einasto model, a separate DF must be generated to accommodate variations in halo characteristics.

## 2.2 The SPARC Sample

The COMPRESS code (Sellwood and McGaugh, 2005; Sellwood, 2014), by design, can be used to map the primordial dark matter halos of observed galaxies. Utilising data from the SPARC (Spitzer Photometry & Accurate Rotation Curves) database (Lelli et al., 2016),<sup>6</sup> COMPRESS can model the dark matter halos of these observed galaxies as they were before the substantial accretion of baryonic matter. SPARC, containing

<sup>6</sup>The SPARC database can be accessed <http://astroweb.cwru.edu/SPARC/>

data on over over 175 galaxies, is instrumental in this effort, providing comprehensive photometric and kinematic details essential for such analysis.

A significant advantage of the SPARC database lies in its comprehensive data collection, which includes Spitzer Space Telescope photometry in the near-infrared band and detailed measurements of gas distributions. The near-infrared wavelength range is particularly effective for stellar mass estimation. In comparison to optical band measurements, near-infrared data results in a smaller scatter in the mass-to-light ratio. This is because, in the optical range, young, luminous stars can disproportionately affect the mass-to-light ratio, leading to less accurate mass estimations. However, the near-infrared band captures light emission that is more evenly representative of the entire stellar population, including older, less luminous stars that constitute the majority of a galaxy's mass. This results in more reliable and consistent estimations of the stellar component.

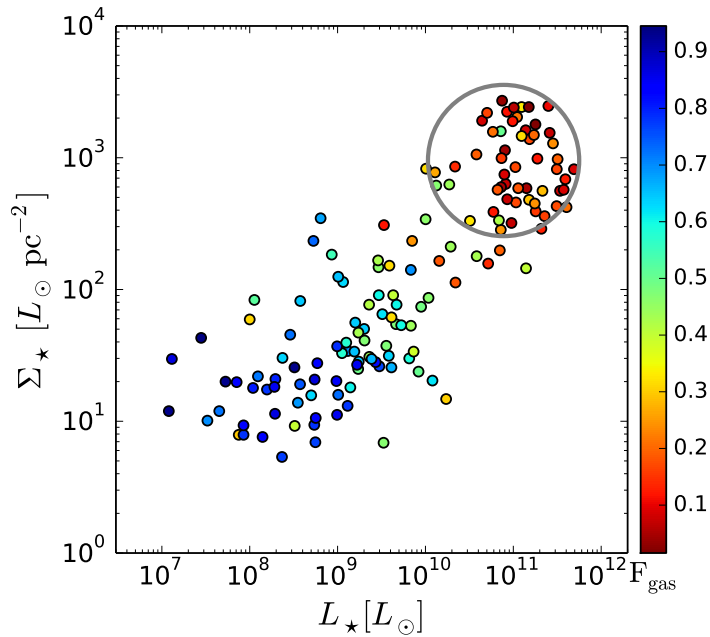


**Figure 2.2:** The distribution of SPARC galaxies in luminosity and effective surface brightness (McGaugh et al., 2016). Each galaxy is colour-coded by gas fraction with the colour gradient varying from gas-rich (blue) to gas-poor (red) galaxies. The range of galaxies used for this project have been highlighted with a grey circle.

In addition to stellar data, SPARC's 21cm radio interferometry maps the distribution of hydrogen gas across the galaxy. The combination of stellar mass estimates from near-infrared photometry and gas distribution data from radio interferometry offers a comprehensive view of the baryonic components in galaxies, which is essential for accurately modelling the effect of these baryons on dark matter halos using COMPRESS.

Furthermore, SPARC's rotation curves, derived primarily from H<sub>I</sub>/H<sub>α</sub> observations, offer extensive and precise coverage. Extending up to 100kpc, and reaching as deep as 1kpc into galactic centres, these curves trace the gravitational potential, constraining the gravitational influence of dark matter halos. These kinematic data constraints enhance the effectiveness of COMPRESS, enabling a more accurate mapping of the structure of dark matter halos.

Figure 2.2 plots all 175 SPARC galaxies in effective surface brightness and effective luminosity space colour-coded by the fraction of gas in the galaxy. This project focuses on 31 of the galaxies marked in the grey circle in the figure. These galaxies are massive and exhibit a lower gas fraction, indicative of a stellar-dominated baryonic composition. These galaxies provide a representative sample of the most massive and least gas-rich

systems within the SPARC data set. This project focuses on the most massive galaxies in SPARC because the effects of baryonic compression are expected to be most significant for this subsample.

## 2.3 Deriving Dark Matter Halos For Disk Galaxies

### 2.3.1 The Traditional Approach

The standard method for fitting galaxy rotation curves typically relies on assuming a specific dark matter density profile, such as the NFW profile, and then finds the best fit parameters that align with observed rotation curves. An example of this approach is depicted in figure 2.3, where a pristine NFW dark matter halo was employed to achieve a reasonably good fit. However, this method, while widely used, has significant limitations. Principally, it treats the dark matter halo and the baryonic distribution within galaxies as separate, independent components, despite their actual interconnection via gravity. Such an approach leads to the assumption that the NFW dark matter halos qualitatively remain constant throughout galactic evolution, disregarding the potential impact of baryonic matter reshaping the dark matter halo during galaxy formation.

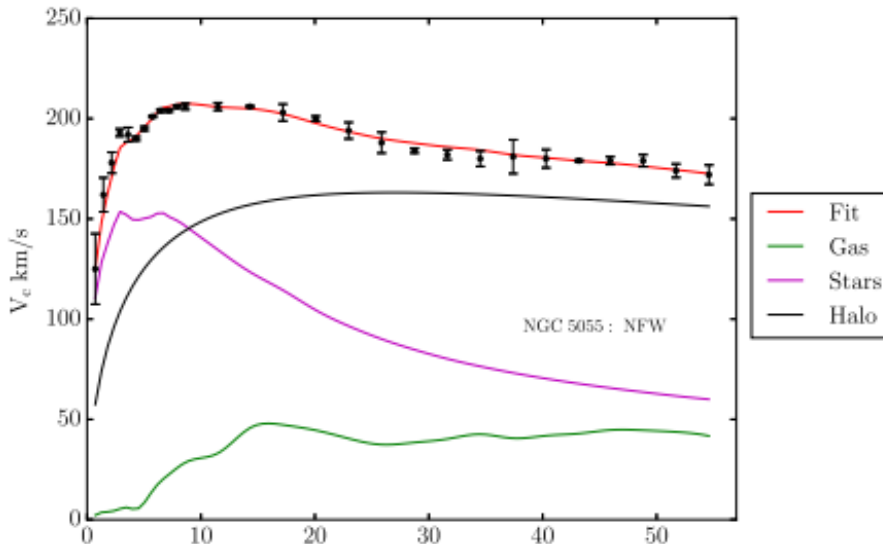


**Figure 2.3:** Best fit rotation curve neglecting the adiabatic contraction of the dark matter halo for the galaxy NGC 5055 from Katz et al. (2017). The black data points with error bars are the measured rotation curve. Magenta and green curves denote the contribution to the rotation curve for the stars and gas respectively, where the stellar contribution has been adjusted to find the best fit. The black curve is the contribution of the best-fit NFW halo. The red curve represents the total rotation curve according to equation 20.

To adequately explore the parameter space required for fitting a rotation curve, a mathematical description of a dark matter halo is required. In this project, a commonly used convention to describe a dark matter halo is adopted. While a dark matter halo can theoretically extend to infinity, for practical purposes, it is characterised as a spherical region within which the average mass density reaches a specific threshold relative to the critical density of the universe.<sup>7</sup> This threshold is conventionally set at 200 times the

<sup>7</sup>The critical density of the universe is a concept in cosmology that represents the density at which the universe achieves a flat geometry, neither continuing to expand indefinitely nor collapsing back in on itself. It is the precise density needed for the universe's expansion rate to asymptotically approach zero over an infinite timescale. This density is incredibly small, equivalent to just a few hydrogen atoms per cubic meter of space.

critical density, denoted as  $\bar{\rho} = 200\rho_{\text{cr}}(z)$ .  $\rho_{\text{cr}}(z)$  is a dynamic quantity that can change with redshift. The galaxies relevant to this study are all located at a redshift  $z = 0$ , so let  $\rho_{\text{cr}}(0) = \rho_{\text{cr}}$ . The radius at which a dark matter halo's average density matches 200 times the critical density of the universe is termed the virial radius and is denoted by  $R_{200}$ . The corresponding mass within this radius, termed the halo or virial mass, is the sphere with average density  $\bar{\rho} = 200\rho_{\text{cr}}$  given by

$$M_{200} = 200\rho_{\text{cr}} \frac{4\pi}{3} R_{200}^3. \quad (14)$$

This mass represents an approximate total mass of the halo, rather than an absolute boundary of it and the approximation is a pragmatic approach to model a dark matter halo. From this definition, the so-called virial velocity associated with the halo is given by

$$V_{200} = \sqrt{\frac{GM_{200}}{R_{200}}} = \sqrt{\frac{800G\pi\rho_{\text{cr}}}{3}} R_{200}. \quad (15)$$

### Fitting NFW Halos to Rotation Curves

Considering the NFW density profile as described by equation 8, then the mass enclosed by the radius  $r$  is found by integrating the density

$$M_{\text{NFW}}(r) = 4\pi\rho_s r_s^3 \int_0^r \frac{r' dr'}{(r_s + r')^2} = 4\pi\rho_s r_s^3 \left[ \ln\left(1 + \frac{r}{r_s}\right) - \frac{r}{r + r_s} \right] \quad (16)$$

While the NFW density profile is singular, the enclosed mass is well behaved at the origin of the halo. Then by definition, the halo mass is the mass within the virial radius

$$M_{200} = M_{\text{NFW}}(R_{200}) = 4\pi\rho_s r_s^3 \left[ \ln(1 + C_{200}) - \frac{C_{200}}{1 + C_{200}} \right] \quad (17)$$

where the so-called concentration index,  $C_{200} = \frac{R_{200}}{r_s}$ , is another frequently employed metric when analysing dark matter halos. It quantifies the mass concentration in the halo's inner regions, with larger  $C_{200}$  values indicating increased concentration. By combining equations 16, 17 and 4 the velocity of a test particle moving on a circular orbit within the gravitational well of a NFW dark matter halo is given by

$$V_{\text{NFW}}(x) = V_{200} \sqrt{\frac{C_{200}}{x} \frac{\ln(1+x) - x/(1+x)}{\ln(1 + C_{200}) - C_{200}/(1 + C_{200})}} \quad (18)$$

where the dimensionless parameter  $x = \frac{r}{r_s}$  has been introduced. However, it should be noted that

$$r_s = \frac{R_{200}}{C_{200}} = \frac{V_{200}}{C_{200}} \sqrt{\frac{3}{800G\pi\rho_{\text{cr}}}}, \quad (19)$$

which is pertinent since then it can be seen that  $V_{\text{NFW}} = V_{\text{NFW}}(r, V_{200}, C_{200})$ . Thus when fitting rotation curves  $V_{200}$  and  $C_{200}$  serve as two of the fitting parameters. The total circular velocity, which is used to model an observed rotation curve such as that shown in 2.3, is typically given as

$$V_{\text{tot}}(r) = \sqrt{V_{\text{NFW}}(r)^2 + \Upsilon_* V_*(r)^2 + V_{\text{gas}}(r)^2}. \quad (20)$$

The velocity contributions from the stars, and gas are denoted by  $V_*(r)$  and  $V_{\text{gas}}(r)$  respectively. The mass to light ratio is expressed as a ratio of solar mass to solar luminosity,  $\Upsilon_* = n \frac{M_{\odot}}{L_{\odot}}$  for some real number  $n > 0$  and it is used to infer how much stellar

mass is in the galaxy. This point is important since what is measured is the galaxy's luminosity, but the mass is the quantity of interest. If on average a star in the observed galaxy had the same mass and luminosity as the Sun, then  $n = 1$ . In practice, the value of  $\Upsilon_*$  is inherently uncertain and as such it is typically a free parameter during the rotation curve fitting process.

In the context of rotation curve fitting, the velocity contribution of  $V_{\text{gas}}$  is often treated as a fixed parameter. This is due to the precise mapping of the gas distribution in galaxies achieved through 21cm radio interferometry. This method accurately traces the hydrogen gas distribution without the uncertainties associated with mass-to-light ratios, used for stellar components. As a result,  $V_{\text{gas}}$  is considered a reliable measure, consistently contributing to the total rotation curve across different models.

In summary it can be seen that there are at least three free parameters for rotation curve fitting using an NFW halo,  $\{V_{200}, C_{200}, \Upsilon_*\}$ . The first two parameters define the NFW dark matter halo while the third sets the amount of baryonic matter in the galaxy.

### 2.3.2 New Approach: Incorporating Halo Contractions

As mentioned earlier, using the pristine NFW halo in the traditional rotation curve fitting procedure treats the dark matter halo and the baryonic matter as independent component. Addressing this limitation, the current project is motivated from the work of [Li et al. \(2022a\)](#), who expanded upon this conventional rotation curve fitting methodology. To briefly revisit their approach, they innovatively incorporated the baryonic compression of the NFW profile into the rotation curve fitting process. Their findings revealed that the resulting compressed halos for massive galaxies were extremely cuspy, a significant increase from the initial NFW halos. The resulting super-cuspy halos left little room for baryons, consequently broadening the Core-Cusp problem to massive galaxies. The goal of this project is to adopt a similar approach but with the Einasto model as the starting point for the primordial dark matter halo, with the focus on the most massive galaxies from the SPARC database for which the effect of baryonic compression should be most pronounced.

The Einasto dark matter halo model emerges as an ideal candidate for further exploration, since it was demonstrated by [Navarro et al. \(2004\)](#) to be a superior fit to DMO simulated halos compared to the NFW model. Compared to the NFW profile, the Einasto model, as formulated in equation 10, includes an additional free parameter, the shape parameter  $\alpha_\epsilon$ . This parameter significantly enhances the model's flexibility, allowing for a range of profiles from characteristically cored to cuspy, particularly at the smallest resolvable radii. Such versatility is of great benefit to this investigation, enabling an examination of a spectrum of primordial halo structures, ranging from distinctly cored to super cuspy, to understand their evolution under the influence of baryonic compression. By leveraging the Einasto model's adaptability with  $\alpha_\epsilon$ , a better determination of the initial dark matter halo conditions necessary to replicate observed rotation curves after undergoing baryonic compression can be investigated.

#### Fitting Contracted Einasto Halos to Rotation Curves

Following the methodology used for the NFW profile, the mass enclosed by radius  $r$  for the Einasto profile is obtained through the integration of equation 10 as

$$\begin{aligned} M_{\text{Einasto}}(r) &= 4\pi\rho_s \exp\left(\frac{2}{\alpha_\epsilon}\right) \int_0^r r'^2 dr' \exp\left\{-\frac{2}{\alpha_\epsilon} \left(\frac{r'}{r_s}\right)^{\alpha_\epsilon}\right\} \\ &= 4\pi\rho_s r_s^3 \exp\left(\frac{2}{\alpha_\epsilon}\right) \left(\frac{2}{\alpha_\epsilon}\right)^{-\frac{3}{\alpha_\epsilon}} \frac{1}{\alpha_\epsilon} \Gamma\left(\frac{3}{\alpha_\epsilon}, \frac{2}{\alpha_\epsilon} \left(\frac{r}{r_s}\right)^{\alpha_\epsilon}\right) \end{aligned} \quad (21)$$

where  $\Gamma(a, x) = \int_0^x t^{a-1} e^{-t} dt$  is the incomplete gamma function. Then, the halo mass is the enclosed mass at the virial radius given as

$$M_{\text{Einasto}}(R_{200}) = M_{200} = 4\pi\rho_s r_s^3 \exp\left(\frac{2}{\alpha_\epsilon}\right) \left(\frac{2}{\alpha_\epsilon}\right)^{-\frac{3}{\alpha_\epsilon}} \frac{1}{\alpha_\epsilon} \Gamma\left(\frac{3}{\alpha_\epsilon}, \frac{2}{\alpha_\epsilon} C_{200}^{\alpha_\epsilon}\right). \quad (22)$$

The circular velocity, as a function of the dimensionless parameter  $x = \frac{r}{r_s}$ , of a test particle moving in the gravitational potential well of an Einasto dark matter halo is given by

$$V_{\text{Einasto}}(x) = V_{200} \sqrt{\frac{C_{200}}{x} \frac{\Gamma\left(\frac{3}{\alpha_\epsilon}, \frac{2}{\alpha_\epsilon} x^{\alpha_\epsilon}\right)}{\Gamma\left(\frac{3}{\alpha_\epsilon}, \frac{2}{\alpha_\epsilon} C_{200}^{\alpha_\epsilon}\right)}}. \quad (23)$$

In contrast to the NFW dark matter halo velocity curve the Einasto model is dependent on 3 free parameters with  $V_{\text{Einasto}} = V_{\text{Einasto}}(r, V_{200}, C_{200}, \alpha_\epsilon)$ .

All the galaxies in this project have a bulge, disk and gas component and as such the total circular velocity can be written as

$$V_{\text{tot}}(r) = \sqrt{V_{\text{CH}}(r)^2 + \Upsilon_{\text{bulge}} V_{\text{bulge}}(r)^2 + \Upsilon_{\text{disk}} V_{\text{disk}}(r)^2 + |V_{\text{gas}}(r)| V_{\text{gas}}(r)}. \quad (24)$$

The velocity contributions from the galactic bulge, the disk and gas are denoted by  $V_{\text{bulge}}(r)$ ,  $V_{\text{disk}}(r)$  and  $V_{\text{gas}}(r)$  respectively.  $V_{\text{CH}}$  is the velocity contribution of the Einasto dark matter halo after baryonic compression, the compressed halo (CH). Galactic bulges typically exhibit higher luminosity than disks, necessitating distinct mass-to-light ratios denoted as  $\Upsilon_{\text{bulge}}$  and  $\Upsilon_{\text{disk}}$ , respectively. Thus, the total parameter space is given by  $\{V_{200}, C_{200}, \alpha_\epsilon, \Upsilon_{\text{bulge}}, \Upsilon_{\text{disk}}\}$ , where the first three parameter are defining the primordial Einasto dark matter halo while the latter two define the amount of baryonic mass in the galactic bulge and disk of the system.

Equation 24 encapsulates the innovative rotation curve fitting procedure pioneered by Li et al. (2022a). Utilising  $V_{\text{CH}}$  instead of  $V_{\text{Einasto}}$  in equation 24 when modelling observed rotation curves ensures that baryonic matter and dark matter are no longer treated as independent components. Instead, the baryonic compression of the primordial Einasto halo is numerically solved in response to a given baryonic distribution, whose mass is determined by the mass-to-light ratios, and the resulting compressed halo is used in the fitting procedure.

The flowchart in Figure 2.4 illustrates the iterative approach for determining the best-fit parameters for rotation curve fitting, adapted for this project based on the methodology of Li et al. (2022a). The procedure begins by setting the magnitude baryonic mass by choosing a tuple from the parameter subspace  $\{\Upsilon_{\text{bulge}}, \Upsilon_{\text{disk}}\}$ . With a fixed baryonic mass distribution a sub-process begins with initialising an Einasto dark matter halo using a triplet from the parameter subspace  $\{V_{200}, C_{200}, \alpha_\epsilon\}$ . COMPRESS is executed and its output velocity of the compressed dark matter halo,  $V_{\text{CH}}$  is then used in conjunction with the velocity contributions of the baryonic components to calculate the total velocity curve according to equation 24. This is tested against the measured rotation curve and in conjunction with prior knowledge of the  $\Lambda$ CDM cosmology the next set of dark matter halo parameters from the subspace  $\{V_{200}, C_{200}, \alpha_\epsilon\}$  are determined to initialise another Einasto dark matter halo and the sub-process is iterated until two successive dark matter halo parameters converge. Once convergence is achieved the results are stored and a new tuple from the the baryonic dependent subspace is chosen and the entire procedure is iterated until the subspace  $\{\Upsilon_{\text{bulge}}, \Upsilon_{\text{disk}}\}$  is exhausted. The best-fit parameters are chosen based on the rotation curve fit quality in conjunction with the  $\Lambda$ CDM prior.

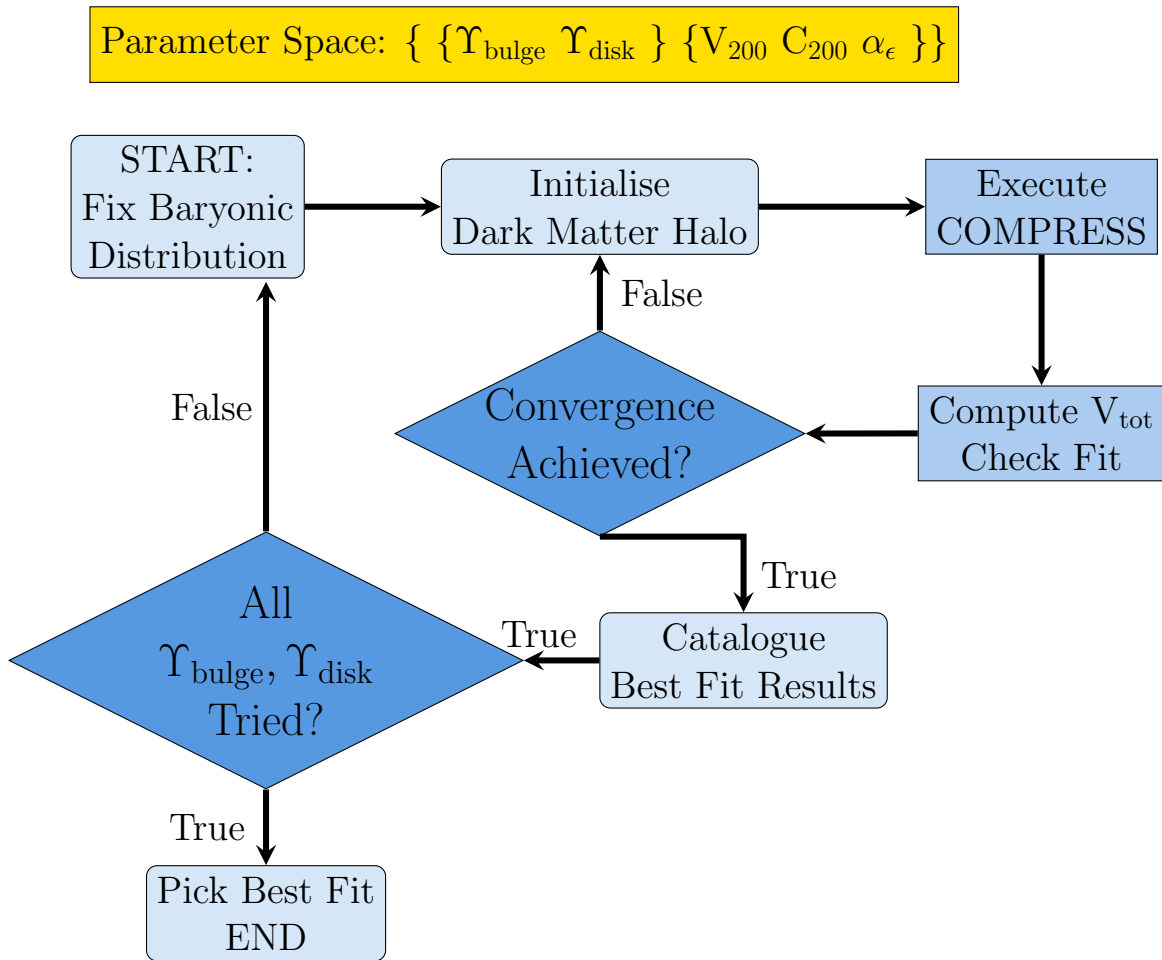


**Figure 2.4:** Flowchart outlining the iterative procedure employed for fitting rotation curves with a compressed dark matter halo. The parameter space, segmented into two distinct sets, is illustrated above the chart. One set pertains to the baryonic-dependent parameters  $P_1 = \{ \Upsilon_{\text{bulge}}^0, \Upsilon_{\text{disk}}^0 \}$ , while the other is related to the dark matter halo-dependent parameters  $P_2 = \{ V_{200}, C_{200}, \alpha_{\epsilon} \}$ . The algorithm initiates by fixing the baryonic distribution based on a specific tuple drawn from  $P_1$ . Subsequently, an iterative search is conducted within the dark matter halo parameter space, starting with an initialised dark matter halo defined by a triplet from  $P_2$ . The COMPRESS algorithm is utilised to numerically solve for the compressed dark matter halo. The resulting total velocity curve  $V_{\text{tot}}$ , in accordance with equation 24, is evaluated against both fit quality and cosmological constraints. Iteration continues, reinitialising the dark matter halo parameters, until successive values of dark matter halo parameters converge. Upon achieving convergence, the results are stored, and a new tuple from the baryonic parameter space is selected. The procedure is repeated until all tuples from  $P_1$  have been exhausted. Then, the best fit mass-to-light ratios are chosen from  $P_1$  and their corresponding best fit halo parameters from  $P_2$  are recorded.

## 2.4 Bayesian Analysis

In this project, Bayesian principles are used to guide the fitting process. Bayes' theorem forms the basis for these principles, positing that:

$$P(A|B) \propto P(B|A)P(A), \quad (25)$$

where  $P(A|B)$  is the posterior probability, representing the probability of proposition  $A$  after considering the evidence  $B$ .  $P(B|A)$  is the likelihood function, which expresses the probability of observing the evidence  $B$  assuming that proposition  $A$  is true.  $P(A)$  is the prior probability of  $A$ , reflecting beliefs about  $A$  before any evidence is considered.

For this project, the likelihood function is selected as  $\exp(-\frac{1}{2}\chi^2)$ , where  $\chi^2$  quantifies

the fit quality of the rotation curves. Simultaneously, a  $\Lambda$ CDM prior is utilised as  $P(A)$ , imposing the prior beliefs based on the  $\Lambda$ CDM cosmological framework.

These Bayesian principles facilitate the fitting procedure by penalising non-physical outcomes by drawing on existing cosmological knowledge. The objective of the Bayesian analysis is to determine the best-fit parameters that maximise a probability function, which combines the likelihood function and the  $\Lambda$ CDM prior. This combined probability function is given by

$$P = \exp\left(-\frac{1}{2}\chi^2\right) \times \exp\left(-\frac{(\log C_{200} - \log C_{\Lambda\text{CDM}})^2}{2\sigma_1^2}\right) \times \exp\left(-\frac{(\log M_{200} - \log M_{\Lambda\text{CDM}})^2}{2\sigma_2^2}\right). \quad (26)$$

Here,  $C_{200}$  and  $M_{200}$  are the halo parameters, and  $C_{\Lambda\text{CDM}}$  and  $M_{\Lambda\text{CDM}}$  are their predicted values according to the prior, with  $\sigma_1$  and  $\sigma_2$  representing the scatter associated with the  $\Lambda$ CDM prior. While  $V_{200}$  is utilised in the fitting process,  $M_{200} \propto V_{200}^3$  is often more relevant and thus they are used interchangeably when referring to halo parameters.

In practical terms, equation 26 is transformed into minimising the modified probability function:

$$P' = -2\ln(P) = \chi^2 + \frac{(\log C_{200} - \log C_{\Lambda\text{CDM}})^2}{\sigma_1^2} + \frac{(\log M_{200} - \log M_{\Lambda\text{CDM}})^2}{\sigma_2^2}. \quad (27)$$

Typically, Bayesian analysis involves the use of hundreds of random walkers to explore the parameter space. However, due to the high computational demands associated with numerically solving the adiabatic compression of a dark matter halo, only one random walker is utilised in this study. This walker is initialised by selecting a pair of mass-to-light ratios, from which the stellar mass,  $M_*$ , is calculated. The stellar mass, in conjunction with the  $\Lambda$ CDM prior, are used to initialise the halo parameters of the random walker. Once initialised, the walker traverses the parameter space to find the point that maximises the probability function as outlined in Equation 27.

#### 2.4.1 Constraints on Baryonic Disks

When measuring rotation curves, two additional factors—galaxy distance and inclination relative to the line of sight—can influence the results. These parameters are sometimes treated as free parameters in traditional rotation curve fitting. However, due to the computational demands of incorporating baryonic compression of dark matter halos into the fitting process, both galaxy distance and disk inclination angle are held constant at their fiducial values as provided by SPARC (Lelli et al., 2016). This approach reduces the number of free parameters, thereby focusing the fitting process on the stellar mass-to-light ratios for the baryonic component. Statistically, these ratios are expected to exhibit lognormal distributions around different mean values, with fiducial values of  $\Upsilon_{\text{disk}} = 0.5$  and  $\Upsilon_{\text{bulge}} = 0.7$  (Bell and de Jong, 2001; McGaugh and Schombert, 2015). During the fitting procedure, a flat prior is imposed on the mass-to-light ratios, which are constrained within the range of  $[0.1, 1.0]$  with a step size of 0.01. To explore this portion of the parameter space, a coarse-to-fine grid search method is employed.

#### 2.4.2 Constraints on Dark Matter Halos

The constraints on dark matter halos are informed by the  $\Lambda$ CDM prior. This prior encompasses the stellar-to-halo mass (SHM) relation and the halo mass concentration

(HMC) relation, imposing constraints informed by established expectations concerning the stellar mass, the halo mass  $M_{200}$ , and the halo concentration  $C_{200}$ .

The HMC relation, deduced from DMO simulations, forms a complementary  $\Lambda$ CDM prior. This relation is quantitatively established as:

$$\log C_{200} = a - b \log (M_{200} / [10^{12} h^{-1} M_{\odot}]) \quad (28)$$

with coefficients  $a$  and  $b$  being contingent on both the adopted cosmology and the dark matter density profile utilised in the analysis (Macciò et al., 2008). For the Einasto profile, the optimal coefficients were determined to be  $a = 0.977$  and  $b = 0.130$  and a standard deviation of  $\sigma = 0.11$  (Dutton and Maccio, 2014).

Alongside the HMC relation, the SHM relation establishes a semi-empirical linkage between the stellar mass within a galaxy and its corresponding dark matter halo mass, grounded in the  $\Lambda$ CDM cosmological framework. According to this framework, the gravitational potential wells of primordial dark matter halos accrete and cool gas to trigger star formation. Galaxies are formed and evolve within the gravitational potential wells of dark matter halos. The stellar mass of a galaxy is, therefore, anticipated to correlate with the mass of its halo, with the premise that more significant potential wells are capable of collecting more gas, leading to increased star formation.

Stellar mass observations are directly measured and statistically represented by the stellar mass function, which reflects the distribution of galaxies across various stellar masses. Conversely, the distribution of dark matter halo masses is deduced from n-body simulations, known as the halo mass function. The SHM relation thus serves as a nexus between these observable and inferred distributions and is expressed mathematically as:

$$\frac{M_{\star}}{M_{200}} = 2N \left[ \left( \frac{M_{200}}{M_1} \right)^{-\beta} + \left( \frac{M_{200}}{M_1} \right)^{\gamma} \right]^{-1} \quad (29)$$

Here,  $M_{\star}$  and  $M_{200}$  denote the stellar and halo masses, respectively. The equation includes four parameters which are redshift-dependent fitting parameters. For galaxies at redshift  $z = 0$ , used in this project, these parameters remain constant, with values derived by Moster et al. (2013) as  $\log M_1 = 11.590$ ,  $N = 0.0351$ ,  $\beta = 1.376$ , and  $\gamma = 0.608$  with a standard deviation  $\sigma = 0.15$ .

### 3 Results

The rotation curve fitting procedure was successfully executed for 31 massive galaxies drawn from the SPARC database (Lelli et al., 2016). A  $\Lambda$ CDM prior was imposed on the halo parameters during the fitting procedure, specifically the SHM (Dutton and Maccio, 2014) and HMC (Macciò et al., 2008) relations, as described in 29 and 28 respectively. A flat prior was imposed on the mass-to-light ratios. Five free parameters for the fitting procedure were identified in the previous section: three halo parameters  $\{V_{200}, C_{200}, \alpha_\epsilon\}$ , and two parameters for the baryonic component  $\{\Upsilon_{\text{disk}}, \Upsilon_{\text{bulge}}\}$ . However, due to computational demands, a strategic decision was made to fix  $\alpha_\epsilon$  at six different values in the range  $[0.1, 0.6]$ , with a step size of 0.1. To illustrate the computation demand, finding the remaining four best-fit parameters for a single galaxy with a fixed  $\alpha_\epsilon$  value takes approximately 7-9 hours on a 12-CPU system.

The rotation curves were fitted for each galaxy seven times: once using the NFW model and six times using the Einasto model, each time with a different fixed value of the shape parameter. This approach allows for a comprehensive study of the effects of baryonic compression on six characteristically different Einasto profiles, ranging from characteristically cuspy ( $\alpha_\epsilon = 0.1$ ) to cored ( $\alpha_\epsilon = 0.6$ ).

The layout of the results is as follows. Section 3.1 presents a selection of rotation curves representative of the sample. Section 3.2 examines whether the best-fit mass-to-light ratios agree with the predictions of stellar synthesis models (Schombert et al., 2019) and whether the best-fit primordial halo parameters recover the imposed  $\Lambda$ CDM prior. Section 3.3 investigates the properties of the best-fit compressed halos and the primordial halos from which they are derived. Finally, Section 3.4 compares the results with those derived from hydrodynamical simulations.

#### 3.1 Individual Rotation Curve Fits

Upon completing the fitting procedure, rotation curves for each galaxy were plotted and analysed. The best-fit rotation curves are collected in the appendix. This discussion focuses on two representative cases: galaxies UGC 08699 and IC 4202. UGC 08699 is a spiral galaxy located at a distance of  $39.30 \pm 9.82$  Mpc, with a noted inclination of  $73^\circ \pm 9^\circ$  (Lelli et al., 2016). The distance and inclination angle are significant since they both influence the measurements of the observed rotation curves and are sources of uncertainty. It is a member of the Lyons Group of Galaxies, LGG 361, indicating its interactions and evolutionary history could be influenced by nearby galactic neighbours. IC 4202 is located in the constellation Coma Berenices. It is one of the most distant galaxies in the sample at an approximate distance of  $100.40 \pm 10$  Mpc (Lelli et al., 2016). The galaxy is observed edge on with an inclination angle of  $90^\circ \pm 1^\circ$ .

Figure 3.1 presents the best-fit rotation curves for UGC 08699, alongside Table 3.1, which records the best-fit mass-to-light ratios, the reduced chi-squared ( $\chi_\nu^2$ ) values as a measure of the rotation curve fit quality, the best-fit primordial halo parameters and the corresponding values of  $\alpha_\epsilon$ . Each rotation curve is labelled according to the  $\alpha_\epsilon$  value employed in the fitting process, with the exception of the curve labelled as NFW which corresponds to the fitting procedure that began with an NFW halo.

The comparison between the best-fit rotation curves for  $\alpha_\epsilon = 0.1$  and  $\alpha_\epsilon = 0.6$  in Figure 3.1 is particularly striking. For the cuspiest halo configuration ( $\alpha_\epsilon = 0.1$ ), the compressed dark matter halo has a more significant impact on the inner galactic dynamics at lower radii. Conversely, its influence is greatly diminished in the most cored configuration ( $\alpha_\epsilon = 0.6$ ). It is apparent that the velocity contribution of dark matter,

| Galaxy Name | $\alpha_\epsilon$ | $\Upsilon_{\text{disk}}$<br>[ $M_\odot/L_\odot$ ] | $\Upsilon_{\text{bulge}}$<br>[ $M_\odot/L_\odot$ ] | $V_{200}$<br>[km/s] | $C_{200}$ | $\chi_\nu^2$ |
|-------------|-------------------|---|--|---------------------|-----------|--------------|
| UGC08699    | 0.1               | 0.27  | 0.41   | 136.64              | 10.57     | 1.19         |
| UGC08699    | 0.2               | 0.31  | 0.5  | 125.28              | 9.43      | 0.96         |
| UGC08699    | 0.3               | 0.34  | 0.55   | 114.91              | 8.88      | 0.94         |
| UGC08699    | 0.4               | 0.68  | 0.53   | 127.9               | 5.34      | 0.73         |
| UGC08699    | 0.5               | 0.72  | 0.59   | 155.83              | 4.49      | 0.59         |
| UGC08699    | 0.6               | 0.82  | 0.59   | 147.34              | 4.48      | 0.58         |
| UGC08699    | NFW               | 0.5   | 0.48   | 139.9               | 6.48      | 0.69         |
| IC4202      | 0.1               | 0.64  | 0.1  | 204.64              | 5.09      | 23.95        |
| IC4202      | 0.2               | 0.59  | 0.1  | 159.22              | 7.73      | 19.22        |
| IC4202      | 0.3               | 0.58  | 0.1  | 134.1               | 9.13      | 15.69        |
| IC4202      | 0.4               | 0.5   | 0.1  | 123.29              | 10.35     | 15.93        |
| IC4202      | 0.5               | 0.1   | 0.1  | 122.34              | 14.21     | 14.35        |
| IC4202      | 0.6               | 0.2   | 0.1  | 104.18              | 14.35     | 11.33        |
| IC4202      | NFW               | 0.61  | 0.1  | 141.1               | 9.2       | 16.85        |

**Table 3.1:** Best-fit mass-to-light ratios, primordial halo parameters and corresponding rotation curve fit quality for each fixed value of the shape parameter for UGC 08699 and IC 4202. The instances in which the NFW halo was used in the rotation curve fitting procedure state NFW in the second column.

denoted  $V_{\text{halo}}$ , to the total rotation curve decreases with larger  $\alpha_\epsilon$  values. This trend is not surprising as smaller  $\alpha_\epsilon$  values correspond to cuspier initial halos. The greater central density of cuspier halos will generally exert a greater influence on the inner dynamics compared to more cored configurations.

Further comparison in Figure 3.1 shows that as  $\alpha_\epsilon$  increases, so too does the velocity contribution from  $V_{\text{disk}}$  (blue dashed curve). This phenomenon is supported by Table 3.1, which indicates that larger  $\alpha_\epsilon$  values correlate with higher  $\Upsilon_{\text{disk}}$  values. Although less obvious, data also confirm that the bulge contribution,  $V_{\text{bulge}}$  (purple dashed curve), to the total velocity curve similarly increases with the shape parameter values. Consequently, the increasing contributions from both  $V_{\text{bulge}}$  and  $V_{\text{disk}}$  make it clear that the role of baryonic matter in the inner galactic dynamics becomes more pronounced as  $\alpha_\epsilon$  increases. This shift occurs because more cored dark matter halos contribute less to the inner galactic dynamics, thereby allowing baryonic components to exert a greater influence. This is a trend is observed across the sample of 31 galaxies.

Moreover, the figures in Figure 3.1—the solid black curve representing the compressed halo and the dashed black curve the initial halo—indicates that the impact of baryonic compression is greater for configurations with larger  $\alpha_\epsilon$  values. This is partly because more cored halos having the capacity to accommodate a larger amount of baryonic matter, leading to a more significant baryonic compression effect on the dark matter halos. However, it will be seen and discussed later that the SHM ratio plays a more significant role in compressing the primordial dark matter halos than the baryonic content alone.

Table 3.1 reveals that, although the Einasto profile yields a better fit compared to the NFW profile in certain cases, this is not consistent across all explored values of  $\alpha_\epsilon$ . However, the fit quality indicates that cored halos can adequately model the rotation curves of massive galaxies.

IC 4202 counters the prevalent trend observed in the sample, where more cored halos

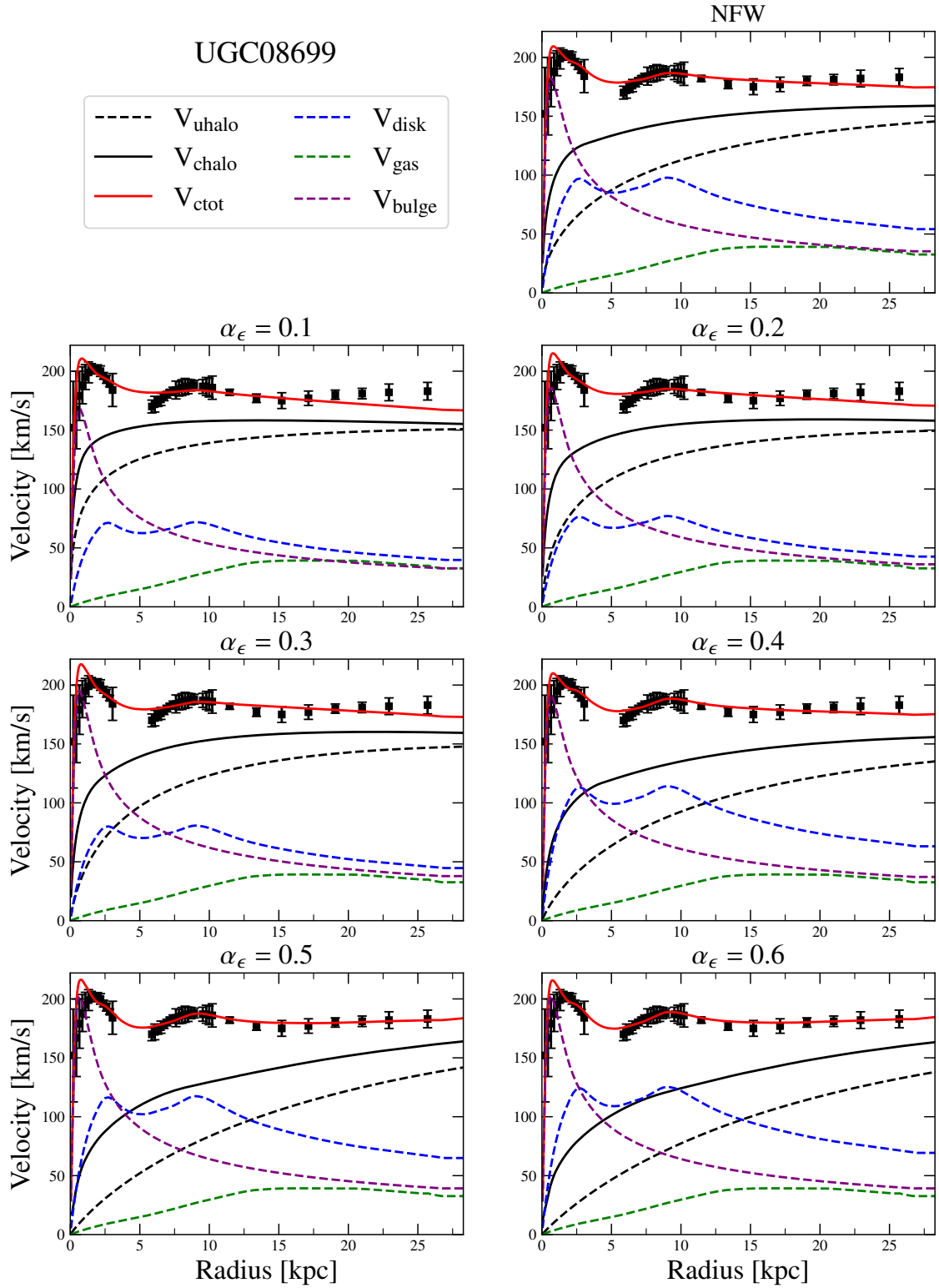


**Figure 3.1:** Rotation-curve fits incorporating adiabatically compressed dark matter halos for galaxy UGC 08699. Markers with error bars represent the observed galaxy rotation curve, showing a noticeable gap between 3.5 and 5.5 kpc where no  $H_{\alpha}$  emission was detected on either side of the galaxy (Noordermeer et al., 2007). The velocity contributions from different components are illustrated by various curves: the gas (green dashed), disk (blue dashed), bulge (purple dashed) and adiabatically compressed dark matter halo (black solid). The red solid curves are the composite rotation curves, summing all baryonic and compressed dark matter halo contributions in accordance with equation 24. For comparison, initial dark matter halos are shown with black dashed curves. Each sub-panel displays a model configuration identified by its  $\alpha_{\epsilon}$  value, which is used as the title for clarity. Additionally, a model using an NFW halo as the primordial halo is included for comparison in the top right panel

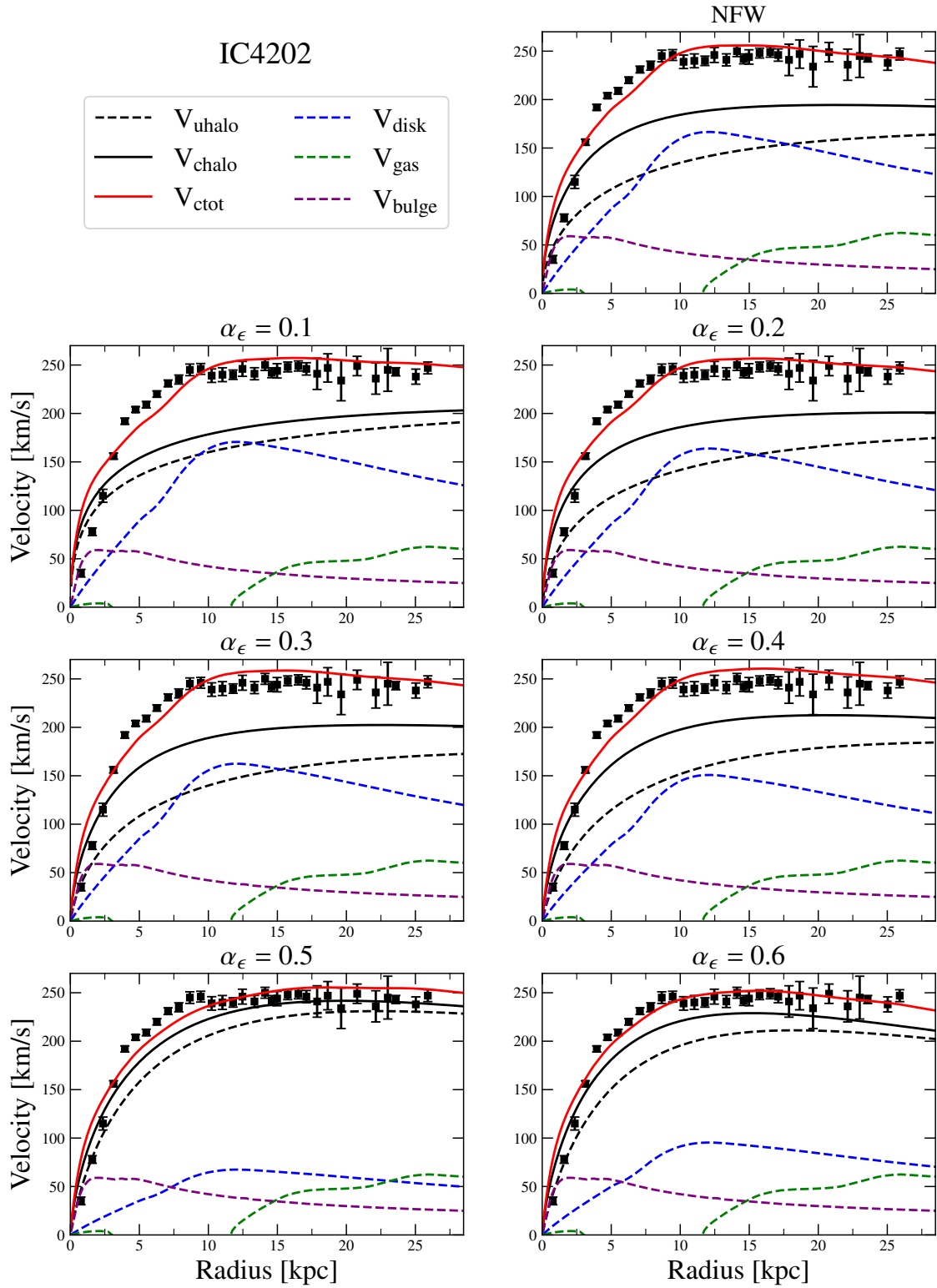


Figure 3.2: Same as Figure 3.1, but for galaxy IC 4202.

generally support a larger baryonic mass compared to the cuspier halos. Its best-fit rotation curves are illustrated in Figure 3.2 with corresponding best-fit parameters detailed in Table 3.1. The stellar mass-to-light ratios for the bulge,  $\Upsilon_{\text{bulge}}$ , is tightly constrained by the innermost data point of the observed rotation curve, necessitating a minimal value of  $\Upsilon_{\text{bulge}} = 0.1$ . In the best-fit rotation curve corresponding to a  $\alpha_\epsilon = 0.1$ , the substantial disk contribution does not translate into effective compression of the primordial halo as might be expected if the bulge were more prominent. Comparing the configurations corresponding to  $\alpha_\epsilon = 0.1$  and  $\alpha_\epsilon = 0.4$ , the baryonic mass within the disk has decreased by approximately 20%, yet the effect of baryonic compression has intensified. This deviates from the pattern noted in UGC 08699. Within the inner region of the galaxy (less than 10 kpc), a discernible increase in the SHM ratio is evident for the configuration with  $\alpha_\epsilon = 0.4$  compared to  $\alpha_\epsilon = 0.1$ , despite a reduction in the overall baryonic content. Quantitatively, the total SHM ratio has increased from  $\log(M_\star/M_{200}) \approx -1.46$  in the  $\alpha_\epsilon = 0.1$  configuration to  $\log(M_\star/M_{200}) \approx -0.90$  in the  $\alpha_\epsilon = 0.4$  configuration.

It can be seen from Table 3.1 that  $C_{200}$  is twice as large for the configuration with  $\alpha_\epsilon = 0.4$  compared to the configuration with  $\alpha_\epsilon = 0.1$ . This may suggest that more concentrated halos are more difficult to compress than less concentrated halos. The enhanced effect of baryonic compression in IC 4202, despite a diminished baryonic contribution, underscores the significant role that the SHM ratio plays in impacting compression, rather than the baryonic content alone. Moreover, it can be observed in Table 3.1 that the fit quality is quite poor for IC 4202, as demonstrated by high  $\chi_\nu^2$  values. While IC 4202 deviates from the general trend seen across the sample, where larger  $\alpha_\epsilon$  values correspond to larger mass-to-light ratios, the poor fit quality makes it less reliable than the previous representative galaxy, UGC 08699. And yet, despite the poor fit quality, it is evident from the  $\chi_\nu^2$  values that IC 4202 is better modelled using cored halos.

It is also noteworthy that for  $\alpha_\epsilon \geq 0.5$ , there is a significant reduction in the disk mass-to-light ratio, leading to a rotation curve where dark matter dominates across all radii. Such observed rotation curves, characterised by a gradual rise and subsequent flattening, could potentially be modelled effectively by a dark matter component alone. This feature becomes critical within the context of a four-dimensional parameter space in the fitting procedure. The absence of distinctive features such as wiggles or bumps on the rotation curve introduces the risk of degeneracies. Often, these wiggles or bumps can be attributed to the velocity contributions from the baryonic matter distribution alone. Consequently, rotation curves exhibiting such features, when modelled to include both baryonic matter and dark matter components, necessitate an interplay between the parameters of the dark matter halo and those of the baryonic matter. Within the sample, rotation curves exhibiting these specific characteristics sometimes result in best-fit scenarios where the baryonic contribution is suppressed, and the dark matter component dominates the dynamics, underscoring a limitation of the current fitting approach. To mitigate this issue, refinement strategies could include narrowing the grid search for the mass-to-light ratio parameter space or setting a more stringent limits on the mass-to-light ratios for galaxies with such flat rotation curves. These adjustments could help to enhance the robustness of the fitting procedure and reduce the impact of degeneracies.

However, such adjustments, while theoretically sound, would require careful implementation on a galaxy-by-galaxy basis and may introduce subjective biases. Additionally, an attempt to refine the grid for galaxy NGC 5985 did not yield improved fit parameters, indicating that this approach may not necessarily resolve the underlying issue of degeneracies.

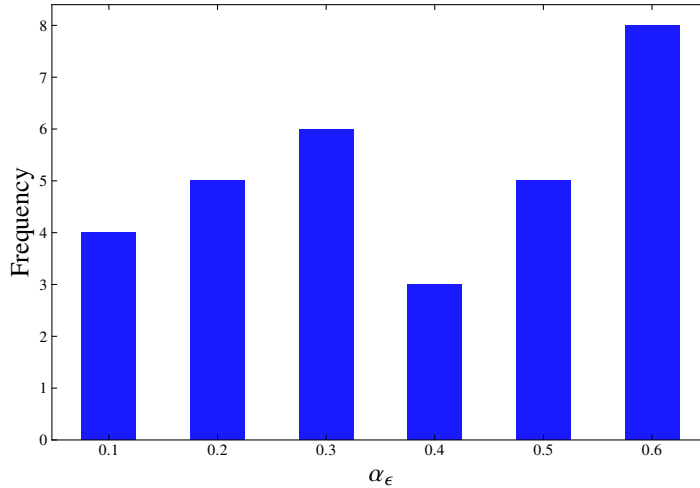


**Figure 3.3:** Histogram of the distribution of  $\alpha_\epsilon$  values for the optimal-fit parameters.

## 3.2 Analysis of Best-Fit & Optimal-Fit Parameters

This subsection analyses the best-fit parameters  $\{M_{200}, C_{200}, \Upsilon_{\text{disk}}, \Upsilon_{\text{bulge}}\}$  in the context of the imposed  $\Lambda$ CDM prior during the fitting procedure and the expectations of stellar population synthesis models [Schombert et al. \(2019\)](#). The best-fit parameters are those which, during the fitting procedure, minimise the probability function, as described by equation 27. The best-fit parameters, derived for both the NFW and Einasto dark matter halo models, are documented in Tables A.1 and A.2 in the appendix.

For the Einasto model, the parameters that represent the most optimal fit for each galaxy—highlighted in bold in the table—are termed “optimal-fit” parameters. These are selected from the range of  $\alpha_\epsilon$  values, chosen for each galaxy based on their ability to best minimise the probability function. Thus, while the best-fit parameters refer to the most suitable values found for each individual galaxy across the entire range of  $\alpha_\epsilon$  values, the optimal-fit parameters refer specifically to the subset of these that provided the best-fit per the selection criteria for each of the 31 galaxies, effectively narrowing down the selection to 31 sets of parameters. *Distinguishing between the optimal-fit and best-fit parameters provides an additional layer of analysis throughout the results section.*

Although  $\alpha_\epsilon$  was not used as a free parameter during the fitting procedure, examining the values derived from the optimal-fit parameters for each galaxy is insightful. These values are displayed in the histogram in Figure 3.3. The mean value is  $\bar{\alpha}_\epsilon = 0.38$ , significantly higher than the prediction of approximately  $\alpha_\epsilon \approx 0.17$  suggested by DMO simulations ([Dutton and Maccio, 2014](#)). Notably, the most frequent result is the configuration with  $\alpha_\epsilon = 0.6$ , representing the most cored initial dark matter halo. However, the median value,  $\alpha_\epsilon = 0.4$ , suggests that there is no clear preference within the optimal-fit parameters for either distinctly cored or cuspy dark matter halo models, as evidenced by the frequency distribution. However, the distribution of  $\alpha_\epsilon$  for optimal-fits indicate that cored halo can perform as well as cuspy halos when incorporating baryonic compression into a model of galactic dynamics of massive galaxies.

### 3.2.1 Mass-to-Light Ratios

During the fitting procedure a flat prior was imposed on the mass-to-light ratios. For this analysis the effective mass-to-light ratio is defined as

$$\Upsilon_{\text{eff}} = \frac{L_{\text{disk}} \Upsilon_{\text{disk}} + L_{\text{bulge}} \Upsilon_{\text{bulge}}}{L_{\text{disk}} + L_{\text{bulge}}} \quad (30)$$

where  $L_{\text{disk}}$  and  $L_{\text{bulge}}$  are the disk luminosity and bulge luminosity of the galaxy as listed in the SPARC database (Lelli et al., 2016). This was calculated for each galaxy for a given  $\alpha_\epsilon$  value with corresponding best-fit mass-to-light ratios,  $\Upsilon_{\text{disk}}$  and  $\Upsilon_{\text{bulge}}$ . For each  $\alpha_\epsilon$  configuration, the best-fit mass-to-light ratios were separated into six bins of equal width.

Figure 3.4 presents the frequency distribution of the best-fit stellar mass-to-light ratios, according to these bins, across six characteristic Einasto models. The frequency distribution was fitted to find the best-fit lognormal distribution and is shown as the black curve in each panel. The chi-square value,  $\chi^2$  of each best-fit lognormal distribution to the binned data was also calculated and is indicated in the top left corner of each panel. The fit quality pertaining to  $\Upsilon_{\text{disk}}$  was so poor that the best fit curve and chi-square values have been omitted from the figure. In contrast to the predicted lognormal distribution centred around fiducial values (Bell and de Jong, 2001; McGaugh and Schombert, 2015), the actual distributions do not conform to this expectation. Although the sample size of 31 may limit the statistical robustness, it is remarkable that the mean of the best-fit distributions falls below the fiducial values ( $\Upsilon_{\text{disk}} = 0.5$ ,  $\Upsilon_{\text{bulge}} = 0.7$ ) in all 18 instances examined in the figure.

Notably,  $\Upsilon_{\text{bulge}}$  tends to favour values significantly below the fiducial benchmark in all instances. This trend is less pronounced in the models with more core-like structures (larger  $\alpha_\epsilon$  values), where a greater proportion of mid-to-low range  $\Upsilon_{\text{bulge}}$  values is apparent. However, for two galaxies in the sample (IC 4202, NGC 4217), the innermost points of their observed rotation curves markedly reduce  $\Upsilon_{\text{bulge}}$ , contributing to a disproportionate representation in the lowest histogram bin. The  $\chi^2$  values demonstrate that for  $\Upsilon_{\text{bulge}}$ , the cuspiers ( $\alpha_\epsilon \leq 0.3$ ) outperform the more cored models in fitting a lognormal distribution. However, for the configuration  $\alpha_\epsilon = 0.1$ , the mean of the lognormal distribution,  $\mu(\alpha_\epsilon = 0.1) \approx 0.13 M_\odot/L_\odot$ , represents a value that is not physically plausible.

The distributions of  $\Upsilon_{\text{disk}}$  exhibit a clear bias for values beneath the fiducial level across all models. Once more, the more distinctly cored models demonstrate a distribution extending towards the fiducial value of  $\Upsilon_{\text{disk}} = 0.5$ , reinforcing the inference that such models accommodate a larger baryonic component when incorporating baryonic compression of dark matter halos into the rotation curve fitting procedure. Nonetheless, apart from the model at  $\alpha_\epsilon = 0.4$ , each distribution peaks below the fiducial value, notably in the lowest histogram bin. While a minority of the observed rotation curves result in best-fit parameters that minimise baryonic mass—indicating dark matter dominance—this factor alone does not account for the prevalence of low  $\Upsilon_{\text{disk}}$  values across the dataset.

When analysing  $\Upsilon_{\text{eff}}$ , it becomes apparent that the distributions for  $\alpha_\epsilon \leq 0.3$  closely align with a lognormal profile, with the mean incrementally increasing as  $\alpha_\epsilon$  rises. The cuspiers ( $\alpha_\epsilon \leq 0.3$ ) show similar distribution patterns among themselves, in contrast to the distinct patterns exhibited by the characteristically cored models ( $\alpha_\epsilon \geq 0.4$ ), which also demonstrate consistency in their distributions. This observation suggests that  $\Upsilon_{\text{eff}}$  exerts a more consistent influence within the fitting procedure compared to  $\Upsilon_{\text{disk}}$  or  $\Upsilon_{\text{bulge}}$  alone. This consistency partly arises because  $\Upsilon_{\text{eff}}$  determines the total stellar mass, which is instrumental when imposing the  $\Lambda$ CDM prior (SHM relation) during the fitting process. Moreover, the total stellar mass is more directly linked to the overall gravitational effects that influence dark matter halos during baryonic compression.

Figure 3.5 presents the averaged best-fit stellar mass-to-light ratios corresponding to different values of  $\alpha_\epsilon$ , with error bars denoting the standard error of the mean. This figure shows that the averaged stellar mass-to-light ratios are increasing with larger

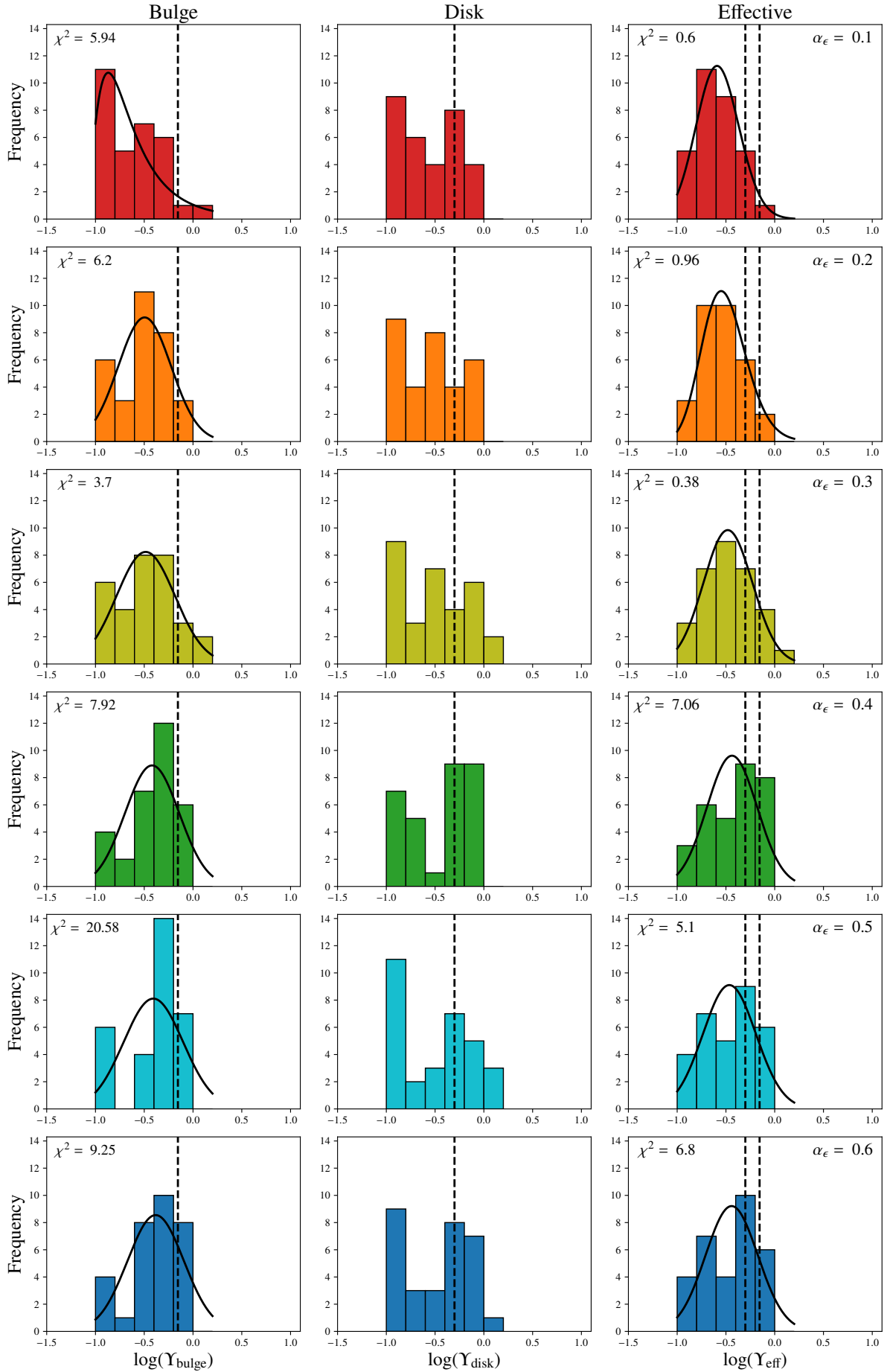


**Figure 3.4:** Histograms depicting the distribution of best-fit stellar mass-to-light ratios for the disks and bulges alongside their combined effective mass-to-light ratio, with vertical dashed lines represent the fiducial values  $\Upsilon_{\text{disk}} = 0.5$  and  $\Upsilon_{\text{bulge}} = 0.7$ . The arrangement of histogram rows correlates with increasing values of the Einasto shape parameter  $\alpha_\epsilon$ . The black curves are the best-fit lognormal distribution with the chi-square value,  $\chi^2$ , of each fit noted in the top left of each panel.

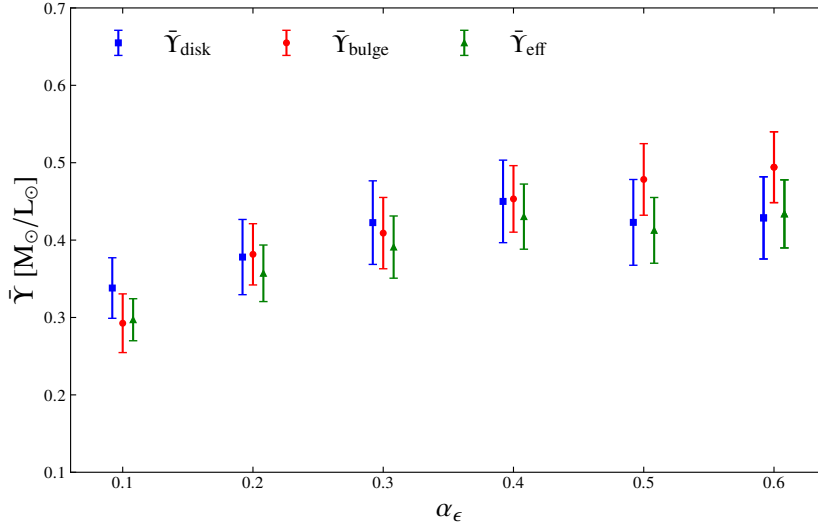


**Figure 3.5:** Averaged best-fit stellar mass-to-light ratios for the disk,  $\bar{\Upsilon}_{\text{disk}}$ , bulge,  $\bar{\Upsilon}_{\text{bulge}}$ , and the effective ratio  $\bar{\Upsilon}_{\text{eff}}$  across the sample of 31 galaxies as a function of the shape parameter  $\alpha_\epsilon$ . To better distinguish the mass-to-light ratios, both  $\Upsilon_{\text{disk}}$   $\Upsilon_{\text{eff}}$  are plotted with a small offset. Error bars denote the standard error of the mean for each  $\alpha_\epsilon$ .

values of  $\alpha_\epsilon$ . This reinforces the previous observations that halos with more core-like structures can facilitate a greater fraction of baryonic matter. The rotation curve fitting procedure reveals no significant differences in the mean stellar mass-to-light ratios of the disk and bulge components across all models. The average ratios predominantly lie below the fiducial values, except for the model at  $\alpha_\epsilon = 0.4$ , which aligns within the margin of error of the disk fiducial value,  $\Upsilon_{\text{disk}} = 0.5$ . While the more cored halos leave more room for baryons, the observed increase in the mean stellar mass-to-light ratios across varying Einasto models is moderate, with the most significant difference observed between the models at  $\alpha_\epsilon = 0.1$  and  $\alpha_\epsilon = 0.6$ , showing a  $\Delta\bar{\Upsilon}_{\text{bulge}} = 0.2$ . Nevertheless, this demonstrates that using more cored configurations can lead to a systematically larger mass-light-ratios.

Calculating the mean stellar mass-to-light ratios for the optimal-fit parameters,  $\bar{\Upsilon}_{\text{disk}} = 0.45 \pm 0.06$ . This is within the error margin of the fiducial value. However,  $\bar{\Upsilon}_{\text{bulge}} \approx 0.42 \pm 0.04$  remains considerably lower at approximately 60% the fiducial value  $\Upsilon_{\text{bulge}} = 0.7$ . The corresponding NFW model mean values are found to be  $\bar{\Upsilon}_{\text{disk}} \approx 0.46 \pm 0.05$  and  $\bar{\Upsilon}_{\text{bulge}} \approx 0.42 \pm 0.04$ . While the NFW model has a degree of cuspsiness similar to that of the Einasto model with configuration  $\alpha_\epsilon = 0.2$ , the resulting mean best-fit mass-to-light ratios align more closely with the average baryonic component proportions seen in Einasto configurations with  $\alpha_\epsilon \geq 0.3$ .

The analysis depicted in Figures 3.4 and 3.5 corroborates the problem previously identified by Li et al. (2022a), wherein accounting for baryonic compression of dark matter halos during the modelling of rotation curves in massive galaxies leads to the suppression of best-fit mass-to-light ratios below the values predicted by stellar population synthesis models (Schombert et al., 2019). A plausible resolution to this discrepancy could be the incorporation of baryonic feedback mechanisms, which might facilitate the expansion of the halo, thereby accommodating a greater proportion of baryonic matter. An exploration of baryonic feedback as a potential solution will be detailed in Section 3.4.

Should the effects of baryonic feedback prove insufficient to significantly expand the dark matter halo and thereby provide additional space for baryons, an alternative approach may involve the adoption of cored primordial halos. The present analysis indicates

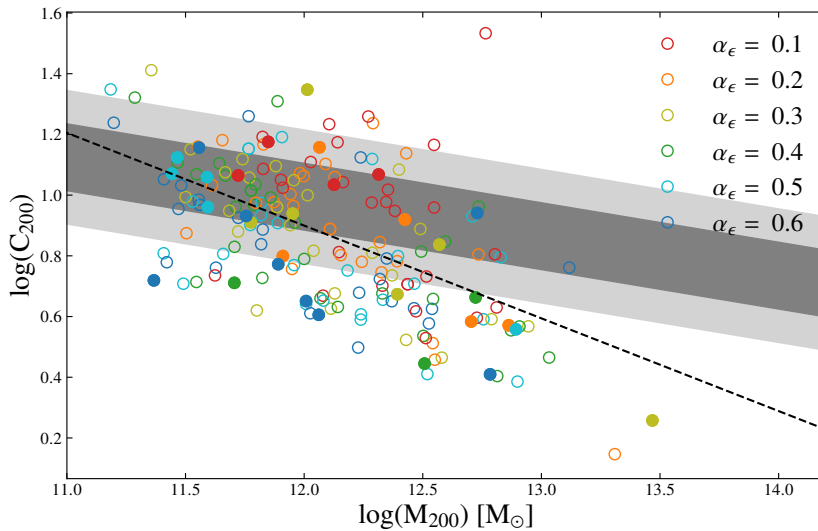


**Figure 3.6:** Comparison of the best-fit parameters for initial dark matter halo from the rotation curve fitting procedure to the halo mass-concentration relation predicted by DMO simulations, as detailed in 28. The shaded areas represent the  $1\sigma$  and  $2\sigma$  prediction intervals, respectively, with a standard deviation of  $\sigma = 0.11$  (Macciò et al., 2008). The data points present the outcomes of the collective 186 best-fit results, with each outcome colour-coded according to the value of the Einasto shape parameter  $\alpha_\epsilon$ . The dashed line represents the regression line of the best-fit parameters, showing a relationship where  $\log(C_{200}) \approx -0.31 \log(M_{200})$ . Filled data points correspond to the 31 optimal-fit parameters, distinguishing them from the broader set of best-fit results.

that configurations with a more pronounced core (larger  $\alpha_\epsilon$  values) coincide with larger mass-to-light ratios. This suggests that employing configurations with  $\alpha_\epsilon > 0.6$  or other cored dark matter halo profiles as the primordial halo may potentially resolve this tension. However, the existence of cored primordial halos contrasts starkly with the cuspy profiles predicted by DMO simulations (Navarro et al., 1996, 2004). Consequently, the necessity for primordial cored halos would have profound implications for the properties of dark matter particles as modelled in DMO simulations predicated upon the  $\Lambda$ CDM paradigm.

### 3.2.2 Checking the Priors on the Initial Dark Matter Halos

During the fitting procedure, the imposed  $\Lambda$ CDM prior includes the HMC relation and the SHM relation, detailed in equations 28 and 29 respectively. This subsection will investigate whether these relations are recovered in the results. Figure 3.6 compares the best-fit initial Einasto dark matter halo parameters  $M_{200}, C_{200}$  with the HMC relation predicted by DMO simulations. The data points, represented by filled circles, distinguish the optimal-fit parameters from the rest. The regression line of the best-fit parameters, indicated by a black dashed line in Figure 3.6, is given by

$$\log(C_{200}) = 0.86 - 0.31 \log(M_{200}/[10^{12}h^{-1}M_\odot]). \quad (31)$$

With a slope of -0.31 and an intrinsic scatter of  $\sigma \approx 0.20$ , both are approximately twice the values predicted by Macciò et al. (2008), which are -0.13 and  $\sigma = 0.11$ , respectively. Notably, the results recover the negative correlation reported by Macciò et al. (2008). The figure clearly shows that the HMC relation is broadly recovered, although there is significant scatter across the entire range of shape parameters. The extent of scatter reduction, if any, for the optimal-fit parameters is not immediately apparent.

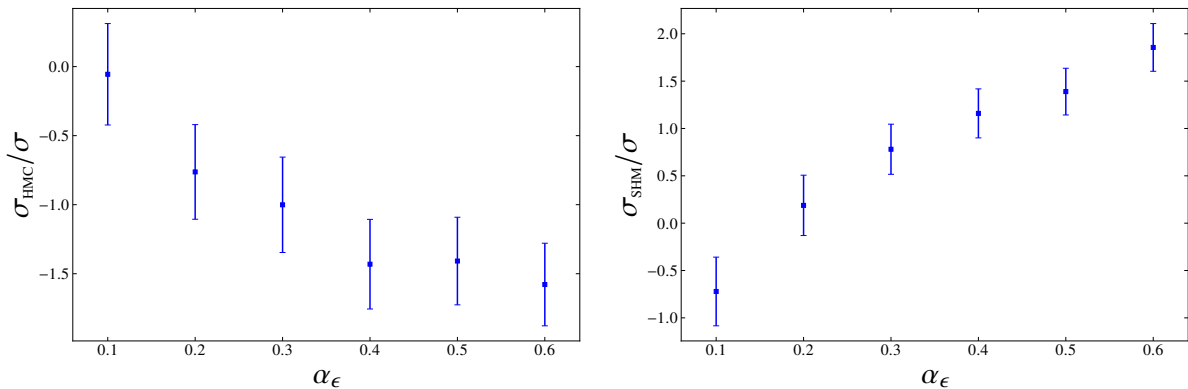


**Figure 3.7:** Left panel plots the mean deviation of the best-fit concentrations from the expected concentrations as a function of  $\alpha_\epsilon$ .  $\sigma_{\text{HMC}}$  is plotted in units of the predicted standard deviation  $\sigma = 0.11$  highlighted as the dark grey band in Figure 3.6. Error bars denote the standard error of the mean. Right panel plots the mean deviation of the best-fit halo masses from the expected halo masses as a function of  $\alpha_\epsilon$ .  $\sigma_{\text{SHM}}$  is plotted in units of the predicted standard deviation  $\sigma = 0.15$  highlighted as the dark grey band in Figure 3.8.

Notably, a significant proportion of the initially less cuspy halos ( $\alpha_\epsilon \geq 0.4$  exhibit lower concentrations than expected.

To quantitatively assess the scatter in the results, the mean deviation of the best-fit concentrations from the expected concentrations (equation 28), denoted by  $\sigma_{\text{HMC}}$ , was calculated. In terms of the intrinsic scatter,  $\sigma = 0.11$ , of the predicted HMC relation (Macciò et al., 2008), the best-fit parameters deviate from expectation by approximately  $\sigma_{\text{HMC}} = -1.04\sigma \pm 0.35\sigma$ . This indicates that the HMC relation has broadly been recovered. For the optimal-fit parameters, this deviation is slightly higher than the full sample, at  $\sigma_{\text{HMC}} = -1.22\sigma \pm 0.36\sigma$ , yet it still generally aligns with the HMC relation.

The left panel of Figure 3.7 plots  $\sigma_{\text{HMC}}$  as a function of  $\alpha_\epsilon$ . It is evident, from this representation of the results, that the HMC relation is better recovered by the cuspy halo models. Notably, the best results corresponds to  $\alpha_\epsilon = 0.1$  and  $\alpha_\epsilon = 0.2$ , aligning closely with the shape parameter value of  $\alpha_\epsilon = 0.17$  predicted by DMO simulations (Dutton and Maccio, 2014). Primordial halos with larger  $\alpha_\epsilon$  values deviate more significantly from the HMC relation than those with smaller values. This is not surprising, since the more cored a dark matter halo is, the lower its concentration is. As DMO simulations, which predict cuspy halos, were employed to construct the HMC relation, a closer alignment with the cuspy models in this project is not surprising.

However, it is crucial to consider that the scatter observed in the results could be attributed to intrinsic limitations in the dataset and fitting process. The galaxies in the sample exhibit a range of inclinations and distances, which were fixed to the fiducial values provided by SPARC (Lelli et al., 2016). Moreover, the rotation curves have been compiled from various sources over many years, potentially introducing inconsistencies and variability in the data quality. These factors should contribute to a larger observed scatter than the intrinsic scatter. With this consideration, even the more cored Einasto dark matter halo configurations are broadly aligning with the HMC relation predicted by DMO simulations.

Figure 3.8 examines whether the SHM relation is recovered in the resulting best-fit primordial Einasto halo mass,  $M_{200}$  and the resulting best-fit stellar mass,  $M_\star$ . The relation appears to be upheld, with more cored halos tending to overshoot the predicted value, while the cuspiest initial dark matter halos fall below the predicted values. This is in agreement with the trend in the overall data that the mass-to-light ratio tend to increase with increasing  $\alpha_\epsilon$  values.

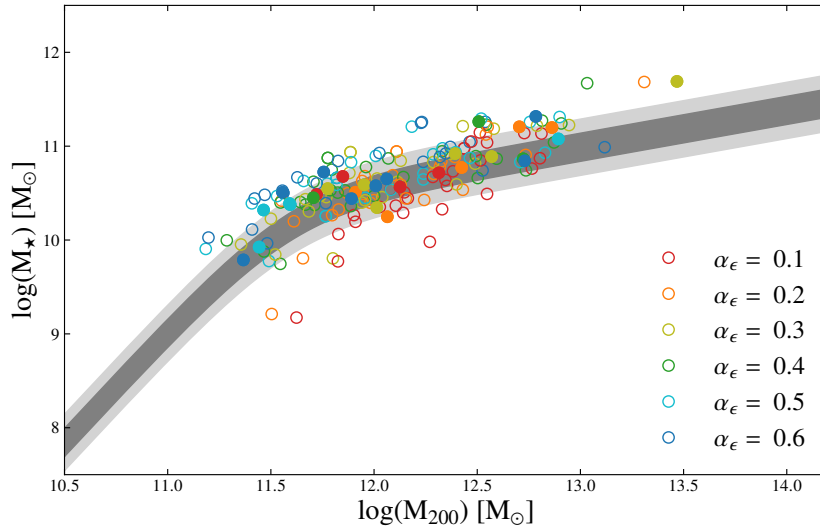


**Figure 3.8:** Comparison of the best-fit mass of the initial dark matter halos,  $M_{\text{halo}}$ , and the stellar mass  $M_*$ , derived using the best-fit  $\Upsilon_{\text{disk}}$  and  $\Upsilon_{\text{bulge}}$  from the rotation curve fitting procedure, to the stellar-to-halo mass relation, as detailed in equation 29. The shaded areas represent the  $1\sigma$  and  $2\sigma$  prediction intervals, respectively, with a standard deviation of  $\sigma = 0.15$  (Moster et al., 2013). The colour scheme is the same as Figure 3.6

Analogously to the HMC relation, the scatter in this context can be quantified by calculating the deviation of the stellar masses from the predicted values using equation 29, denoted by  $\sigma_{\text{SHM}}$ . The predicted scatter in the SHM relation is  $\sigma = 0.15$  (Dutton and Maccio, 2014). The best-fit parameters show a deviation from the expected values by approximately  $\sigma_{\text{SHM}} = 0.78\sigma \pm 0.25\sigma$ , indicating a good recovery of the SHM relation. For the optimal-fit parameters, this deviation is slightly greater, at  $\sigma_{\text{SHM}} = 0.98\sigma \pm 0.23\sigma$ , but it still indicates that the optimal-fit results recover the SHM relation.

The right panel of Figure 3.7 plots  $\sigma_{\text{SHM}}$  as a function of  $\alpha_\epsilon$ . The best recovery of the SHM relation is observed at  $\alpha_\epsilon = 0.2$ , closely aligning with the  $\alpha_\epsilon = 0.17$  value predicted by DMO simulations (Dutton and Maccio, 2014). It is apparent that the cuspy halos more accurately reflect the SHM relation compared to the more cored halos. Nevertheless, similar to the HMC relation, greater scatter than intrinsically expected is likely due to the limitations already mentioned. Thus, even the more cored Einasto models broadly conform to the SHM relation, with each cored model falling within two standard deviations ( $\sigma_{\text{SHM}} = 2\sigma$ ) of the predicted values.

Both relations imposed as a  $\Lambda$ CDM prior appear to have broadly been recovered in the results. As illustrated in Figure 3.7, in both cases the three cuspy halos ( $\alpha_\epsilon \leq 0.3$ ) are within one standard deviation of the predicted scatter, whereas the more cored halos are within two standard deviations. Regarding the HMC relation this outcome is logically consistent, as both cuspy halos and the HMC relation are direct predictions of DMO simulations. While the SHM relation also incorporates empirical data, it is also grounded in DMO simulations and as such finding that the more cuspy Einasto configuration better recover the relation than more cored configurations is indicative of consistency between the fitting procedure and the predictions of DMO simulations.

### 3.3 Properties of Compressed Halos

This subsection will focus on the resulting best-fit compressed halos, specifically examining how the inner structure of the halo has changed under the impact of baryonic compression. The first part of this analysis will address changes in the density pro-

files between the best-fit compressed halos and the primordial halos from which they derived. To gain a deeper understanding of how baryonic compression affects the primordial halos, the fitting procedure was conducted for all galaxies and each primordial halo configurations again, but with the mass-to-light ratios fixed at their fiducial values,  $\Upsilon_{\text{disk}} = 0.5$  and  $\Upsilon_{\text{bulge}} = 0.7$  (Lelli et al., 2016). Results from this additional test will also be presented. Subsequently, attention will shift to the inner structure of the resulting prior- and post-compression halos. To aid this investigation, the density slope for each of the prior- and post-compression halos was measured. The density slope is defined as the logarithmic slope measured at radius  $r = 1.5\% R_{200}$ . This quantity will be denoted by the symbol  $\Gamma$ , to distinguish it from the lowercase  $\gamma$ , which is used to describe the power-law behaviour characterising the cuspieness of the inner slope of dark matter halos.

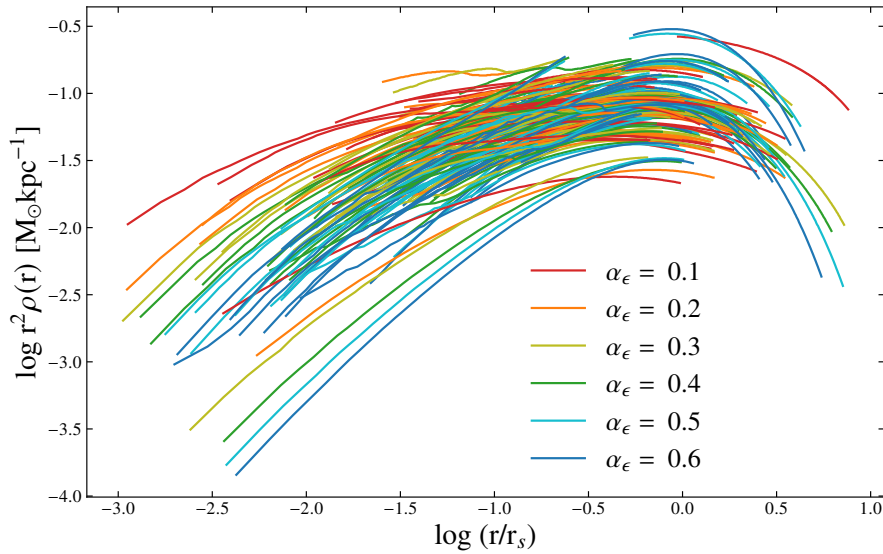


**Figure 3.9:** Density of compressed halos: There are 186 curves corresponding to 31 galaxies and 6 different values of the shape parameter in the Einasto model, each distinguished by colour.

### 3.3.1 Halo Evolution

Figure 3.9 displays the density profiles of the resulting best-fit compressed halos. A consistent pattern emerges across the configurations: halos with smaller  $\alpha_\epsilon$  values tend to exhibit higher central densities compared to those derived from larger  $\alpha_\epsilon$  values. This trend mirrors the characteristics of the primordial halos, which also show similar variations in central density based on different  $\alpha_\epsilon$  values. Thus, the inherent density pattern of the primordial halos is largely preserved in their compressed forms.

The density ratio, defined as the ratio of the compressed dark matter halo density to the density of the primordial halo, provides a valuable visualisation of the extent of baryonic compression. Figure 3.10 plots these density ratios for the best-fit halos as a function of radius, where the dashed line denotes parity between the prior- and post-compression halos. It shows results from a sample of 31 galaxies and six different values of the Einasto shape parameter, with each curve coloured according to its  $\alpha_\epsilon$  value. This figure visually demonstrates the varying impacts of baryonic compression on the primordial halos across different  $\alpha_\epsilon$  values. Post-compression, it is observed that the dark matter density profiles are denser at smaller radii compared to their antecedents across the entire range of  $\alpha_\epsilon$  values, with larger  $\alpha_\epsilon$  values coinciding with a greater

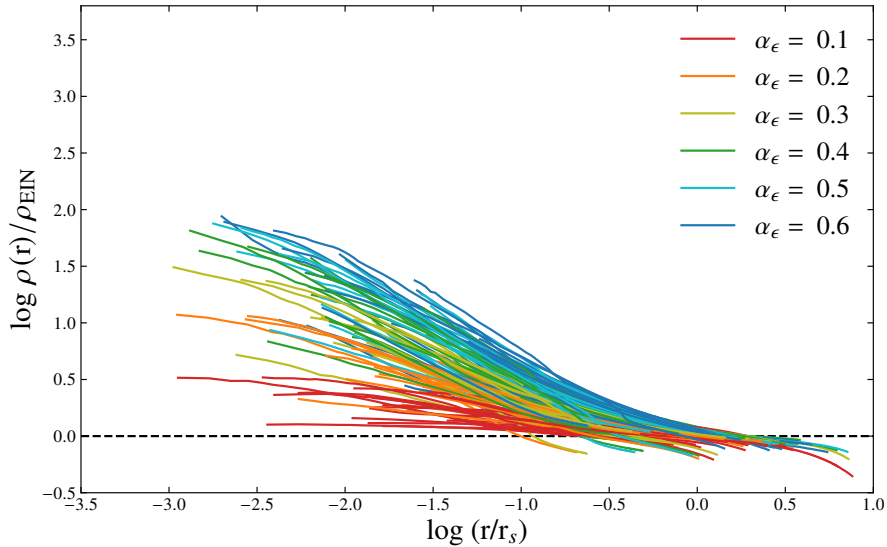


**Figure 3.10:** Density ratios of compressed halos to their antecedent Einasto halos. The 1:1 ratio (black dashed line) is plotted as a reference to highlight deviations from parity between the prior- and post-compression densities.

increase in the central densities of the primordial halos. There is a clear trend where initially more cuspy halos exhibit a lesser degree of compression compared to their more cored counterparts. Contrasting this observation with Figure 3.9, it is evident that while the cuspy halos are less impacted by baryonic compression, they nevertheless tend to remain cuspy than the cored models post-compression.

Quantitatively, as seen in Figure 3.10, the cuspy primordial halos undergo a three to tenfold increase in central density due to baryonic compression, while the more cored profiles exhibit up to a hundredfold increase in central density. The latter increase is far greater than the tenfold increase in central density observed in Li et al. (2022a), investigating the effects of baryonic compression using the NFW profile as the primordial halo model. This difference arises because the cored halos allow more room for baryonic matter, resulting in a larger SHM ratio and, consequently, a greater impact of baryonic compression. Consequently, it is the interplay between the cuspieness of the primordial halo and the SHM ratio that determines the impact of baryonic compression. To investigate this further, a test was conducted using fixed mass-to-light ratios during the fitting procedure. This approach was employed to examine the evolution of different initial halos under consistent gravitational conditions. Specifically, the fitting procedure was executed with the mass-to-light ratios fixed at the fiducial values of  $\Upsilon_{\text{disk}} = 0.5$  and  $\Upsilon_{\text{bulge}} = 0.7$  (Lelli et al., 2016). This setup allowed for a direct assessment of the impact of baryonic compression on various initial halo structures.

Figure 3.11 plots the density ratios of the best-fit halos from the fitting procedure conducted with fixed mass-to-light ratios. Similarly to the free mass-to-light ratio scenario, all configurations demonstrate an increase in density at smaller radii, indicating that the primordial halos have generally become more cuspy due to compression. The same trend, albeit to a lesser degree, is still observed whereby initially more cuspy halos exhibit a lesser degree of compression compared to their more cored counterparts. The reduced impact of compression observed in cuspy halos in the fixed mass-to-light ratio scenario underscores the critical role of the SHM ratio, rather than baryonic mass alone, in driving baryonic compression of dark matter halos. This phenomenon is primarily due to their high initial central densities, which result in lower SHM ratios in the inner regions of the galaxy, thereby diminishing the impact of baryonic compression on these

densely packed primordial halos.

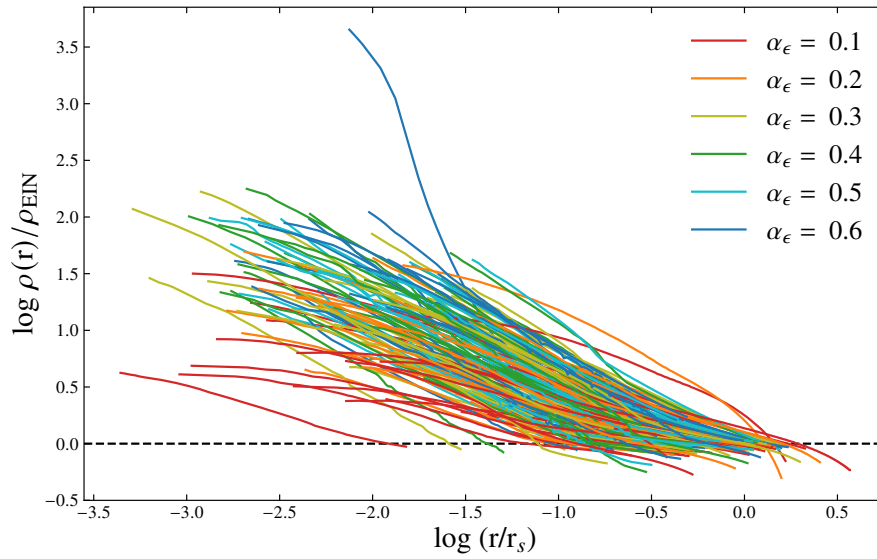


**Figure 3.11:** Same as Figure 3.10 but utilising fixed mass-to-light ratios during the fitting procedure. Identical axis boundaries are used to facilitate easier visual comparison between the two figures.

A closer examination of the plot reveals significant variations in the effects of baryonic compression: halos with an initial  $\alpha_\epsilon = 0.1$  configuration typically exhibit an increase in central density by an order of magnitude, whereas more cored halos can experience increases of up to two orders of magnitude. This effect is much greater than that illustrated in Figure 3.10, as the best-fit mass-to-light ratios generally fall below the fiducial values used in the fixed mass-to-light ratio scenario. Although the fixed mass-to-light ratio scenario shows a greater increase in the central density of post-compression halos, the free mass-to-light ratio conditions in Figure 3.10 reveal a more predictable shift across the  $\alpha_\epsilon$  range. This is evidenced by the smooth transition in colours from red to blue, indicating a systematic change in the effects of baryonic compression. This behaviour contrasts with the outcomes from the fixed mass-to-light ratio scenario, where a greater overlap of colours indicates less distinction in the compression effects between different halos. Previously, it was noted that rotation curves modelled with more cored halos, due to higher SHM ratios, experienced a greater impact from baryonic compression compared to cuspy halos with lower SHM ratios. This observation, combined with the trend that rotation curve fits using larger  $\alpha_\epsilon$  values tend to result in larger best-fit mass-to-light ratios, explains the smoother gradient in increasing density ratios with larger  $\alpha_\epsilon$  values. The fact that there is a much smoother transition for the free mass-to-light ratios scenario compared to the fixed scenario underscores that the observed greater increase in baryonic compression in this project compared to the work of Li et al. (2022a) is due to both a combination of differing mass-to-light ratios as well as the more cored character of some of the profiles used in this project.

### 3.3.2 Inner Halo Structure

In this subsection the density slopes, of the prior- and post-compressed halos, measured at a radius  $r = 1.5\% R_{200}$ , are assessed for their correlation with each other, the SHM ratio and  $\alpha_\epsilon$ . Further analysis in this subsection involves segmenting the best-fit parameters into six bins according to SHM ratios, thus facilitating a deeper understanding of the relationship between halo characteristics and baryonic effects.

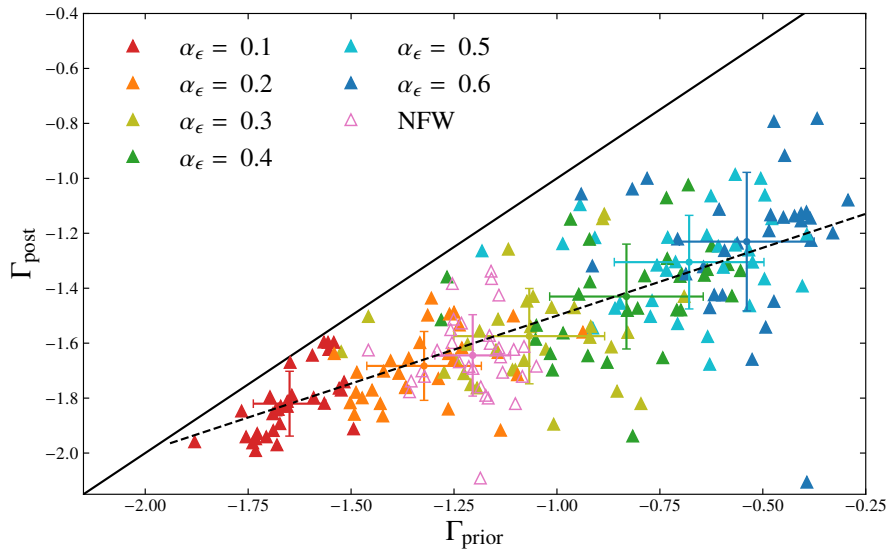


**Figure 3.12:** Density slopes prior- vs. post-compression, measured at radius  $r = 1.5\% R_{200}$ . The mean density slopes of density slopes for both NFW and Einasto data, grouped by  $\alpha_\epsilon$  value, are over-plotted. The black solid line represents the line of parity, while the dashed line is the regression line derived from the 186 data points corresponding to results derived from the Einasto model only.

Figure 3.12 shows the density slopes of the best-fit compressed halos ( $\Gamma_{\text{post}}$ ) plotted against the density slopes of the initial halos ( $\Gamma_{\text{prior}}$ ). Data points are colour-coded to differentiate between various Einasto configurations and the NFW profile, with mean values for each configuration overlaid. The line of parity helps compare the prior- and post-compression states, while the dashed line represents the regression line derived from the Einasto-related data only. This plot serves to illustrate the correlation between the density slopes of prior- and post-compression halos, the cuspsiness of post-compression halos and the extent of baryonic compression across various halo configurations. The regression line,  $\Gamma_{\text{post}} = 0.49\Gamma_{\text{prior}} - 1.01$ , demonstrates the proportional relationship between  $\Gamma_{\text{prior}}$  and  $\Gamma_{\text{post}}$ . Interestingly, the density slopes for the NFW profile align closely with the Einasto configurations characterised by  $\alpha_\epsilon = 0.2$  and  $\alpha_\epsilon = 0.3$ . The mean density slopes for the NFW-related data ( $\Gamma_{\text{prior}}, \Gamma_{\text{post}}$ )  $\approx (-1.20, -1.64)$ , align within one standard deviation of the regression line, indicating that the NFW model follows a similar trend to the Einasto model.

Two trends noted in Figures 3.9 and 3.10 are reflected in Figure 3.12. Firstly,  $\Gamma_{\text{post}}$  consistently falls below the line of parity, indicating that the central density of all dark matter halos increased due to baryonic compression. Secondly, larger  $\alpha_\epsilon$  values correspond to greater departures from the line of parity in  $\Gamma_{\text{post}}$ , supporting the previous statements that more cored initial halos undergo a greater degree of compression than their cuspy counterparts. The post-compression halos range from cuspy to super-cuspy, with  $\Gamma_{\text{post}} \in (-2.1, -0.8)$ . The mean value of  $\Delta\Gamma = \Gamma_{\text{post}} - \Gamma_{\text{prior}}$  shifts from  $-0.17 \pm 0.02$  to  $-0.69 \pm 0.05$  as  $\alpha_\epsilon$  increases from 0.1 to 0.6, quantitatively demonstrating that baryonic compression has a reduced impact on cuspy halos. The mean value,  $\Delta\Gamma(\alpha_\epsilon = 0.6) \approx -0.7$ , with an associated standard deviation of  $\sigma \approx 0.3$ , is significant as it demonstrates that starting with a characteristically cored primordial halo can, through baryonic compression, result in halos with a regular cusp ( $\Gamma_{\text{post}} = -1$ ). This indicates the extent to which feedback mechanisms must act to prevent the cuspy primordial halos predicted by DMO simulations from becoming super-cuspy during the formative stages of galaxy formation. A deeper discussion of this theme will be provided in the next

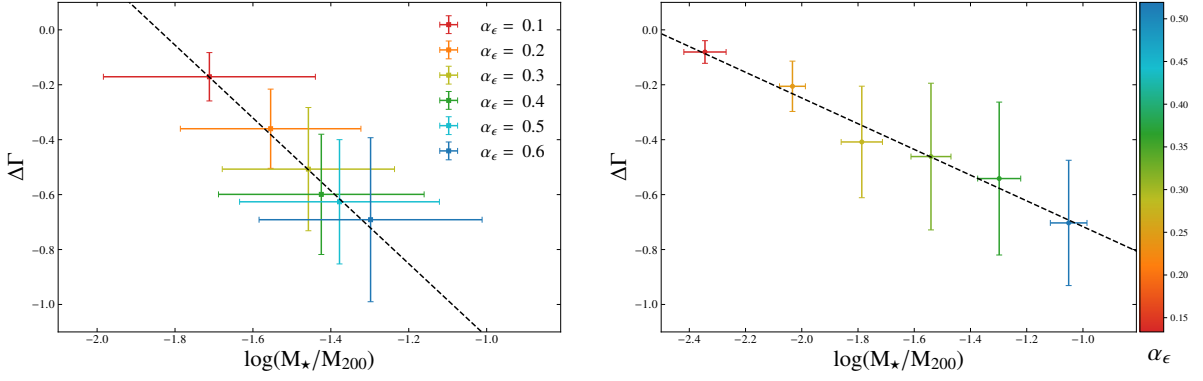


**Figure 3.13:** Left panel: Relationship between the change in density slope and SHM ratios, averaged over different  $\alpha_\epsilon$  values. The best-fit line (dashed) shows a decrease in  $\Delta\Gamma$  with increasing SHM ratio, characterised by a slope of  $-1.33$ . Error bars denote the standard deviation. Right panel: Analysis of density slope changes across six SHM ratio bins, presented with mean values for each bin and colour-coded by the mean  $\alpha_\epsilon$ . The dashed line, representing the best-fit, reveals a trend with a slope of  $-0.47$ , underscoring the relationship between SHM ratios and changes in halo density.

section.

Lastly, Figure 3.12 delineates a clear correlation between prior- and post-compression density slopes, further demonstrating a trend whereby both prior- and post-compression density slopes increase alongside  $\alpha_\epsilon$  values. Given that  $\Gamma_{\text{prior}}$  is defined by the Einasto halo parameters and in particular  $\alpha_\epsilon$  determines the profile's cuspsiness, it is logical that the mean values of  $\Gamma_{\text{prior}}$  monotonically increase with increasing  $\alpha_\epsilon$  values. The same ascending pattern is observed for the mean values of  $\Gamma_{\text{post}}$ , but previous observations of the rotation curves and the density ratios indicate that the SHM ratio significantly influences the effect of baryonic compression, consequently affecting the mean values of  $\Gamma_{\text{post}}$ .

The left panel of Figure 3.13 plots the mean change in density slope against the mean SHM ratio, averaged across different  $\alpha_\epsilon$  values. Error bars denote the standard deviation. The regression line (dashed line) indicates a correlation between the variables,  $\Delta\Gamma \propto -1.33 \log(M_\star/M_{200})$ , whereby an increase in the mean SHM ratio is associated with a greater change in the density slope. The substantial standard deviation accompanying the SHM ratios somewhat weakens the strength of this observed relationship. Despite the large scatter, it is evident that larger mean SHM ratios, which correlate with higher  $\alpha_\epsilon$  values, are linked to more pronounced changes in the density slope. This plot captures how the impact of baryonic compression on the density slope of primordial halos is dependent on the interplay between the shape parameter and the SHM ratio.

The right panel of Figure 3.13 plots the mean change in density slope against the mean logarithmic SHM ratio, with data grouped into six bins based on SHM ratio values. The mean of each bin is colour-coded according to the average  $\alpha_\epsilon$  value within the bin. This method of data aggregation reduces scatter within the SHM ratios, effectively transferring it to the shape parameter. This analytic approach continues to illustrate the correlation between ascending SHM ratios and increasing  $\alpha_\epsilon$  values. Moreover, this representation highlights a more distinct trend between the mean values of  $\log(M_\star/M_{200})$  and  $\Delta\Gamma$ , revealing a correlation with slope  $-0.47$ . This tighter relationship confirms previous inferences that larger SHM ratios correspond to a greater impact baryonic compression.

### 3.4 Possible Solution With Baryonic Feedback: Comparison With Simulations

In section 3.2.1, the analysis corroborated a problem identified by Li et al. (2022a), whereby the resulting best-fit mass-to-light ratios are systematically lower than prediction (Schombert et al., 2019; Lelli et al., 2016), once baryonic compression is accounted for in modelling rotation curves of massive galaxies. The analysis suggested that more cored configurations yield moderately larger mass-to-light ratios, indicating that employing even more core-like primordial halos might address this discrepancy. However, this approach has significant implications for the nature of dark matter, as DMO simulations, which assume a specific nature of dark matter particles, predict cuspy primordial halos. The findings support Li et al. (2022a)'s assertion that the cusp-core problem may be broader than previously thought, such that observations of massive galaxies, as well as dwarf galaxies, are in tension with the predictions of DMO simulations.

However, cored primordial halos are not the only potential solution to this problem. Baryonic feedback, potentially driven by processes such as supernova explosions, stellar winds or an AGN (active galactic nucleus), can expand a dark matter halo, thereby accommodating more baryons. Such feedback can redistribute dark matter, potentially transforming central cusps into cores by injecting energy back into the interstellar medium. This subsection will explore baryonic feedback mechanisms as a potential solution, conducting the investigation within the framework of hydrodynamical simulations that integrate these mechanisms during galaxy evolution, complemented by insights from observational studies.

The discussion initially revolves around hydrodynamical simulations that integrate stellar feedback mechanisms, including star formation, supernova feedback, and primary cooling and heating actions. It then shifts focus to more comprehensive hydrodynamical simulations, which incorporate a broader array of astrophysical phenomena, particularly both stellar and AGN feedback mechanisms.

#### 3.4.1 Stellar Feedback

Di Cintio et al. (2014) demonstrate that incorporating stellar feedback mechanisms in hydrodynamical simulations can significantly modify the central density of dark matter halos in dwarf galaxies. Although this project focuses on massive galaxies, many of the resulting stellar masses fall within the range studied by Di Cintio et al. (2014), due to the resulting systematically low best-fit mass-to-light ratios. Their research used 31 simulated galaxies from the McMaster Unbiased Galaxy Simulations (MUGS) (Stinson et al., 2010), covering a mass range from dwarf galaxies to  $L^*$  galaxies (a galaxy with a luminosity comparable to that of the Milky Way). MUGS include stellar feedback mechanisms during simulated galaxy evolution. However, a drawback of MUGS is that it bypasses the initial phase of gas accretion in galaxy formation. Instead, it converts a fraction of dark matter particles from a pre-existing DMO simulated halo (NFW profile) into gas particles at an approximate redshift of  $z \approx 4$  (12 billion years ago), in line with the cosmological baryonic-to-dark matter ratio (Stinson et al., 2010). This approach may inadvertently omit the effects of baryonic compression during the formative stages of galaxy evolution, which is central to this project. Consequently, this project scrutinises an aspect often overlooked by hydrodynamical simulations.

Di Cintio et al. (2014) analysed the density slopes of dark matter halos that had evolved within the MUGS framework. By plotting these density slopes against the SHM ratio for each simulated galaxy, they identified a correlation between the density slope

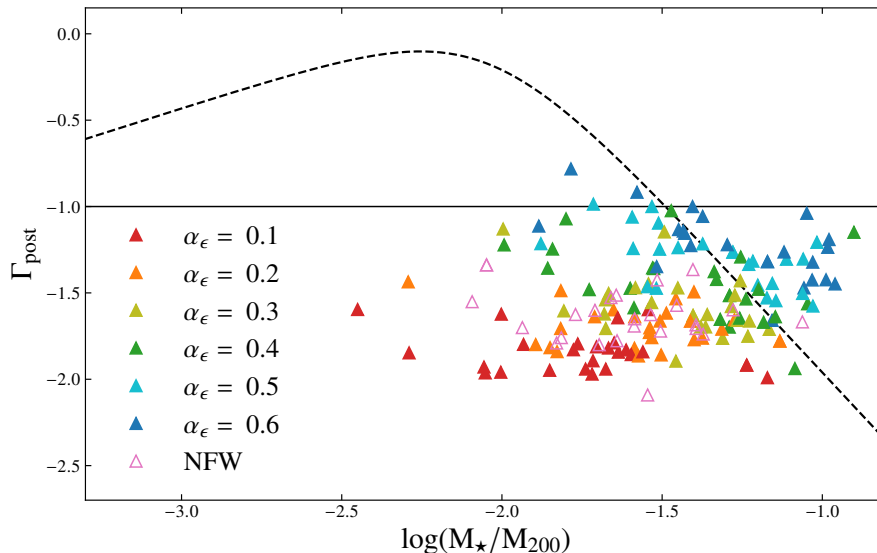


**Figure 3.14:** Post-compression density slopes measured at radius  $r = 1.5\%$   $R_{200}$  plotted against the stellar-to-halo mass ratio. The black dashed curve is the best-fit curve defined by the equation 3 of Di Cintio et al. (2014). The black solid line is the density slope of the primordial dark matter halos used in their study. Only results from this project that fall within the stellar mass range and halo mass range used by Di Cintio et al. (2014) are plotted.

of the dark matter halos and the SHM ratio in these evolved galaxies.<sup>8</sup> Figure 3.14 presents the post-compression density slopes ( $\Gamma_{\text{post}}$ ) plotted against the SHM ratio, focusing specifically on results that fall within the stellar mass range analysed by Di Cintio et al. (2014). The dashed curve depicts the best-fit from Di Cintio et al. (2014), peaking at  $\log(M_{\star}/M_{200}) = -2.3$ . This peak identifies the point where baryonic feedback is most effective in transforming cuspy dark matter halos into cores. The solid line shows the initial density slope of the MUGS primordial NFW halos, illustrating the impact of feedback on the structural evolution of dark matter halos as documented in Di Cintio et al. (2014).

The dashed curve indicates that including stellar feedback mechanisms into hydrodynamical simulations results in halo expansion for SHM ratios less than  $-1.48$ . However, compression occurs for larger SHM ratios, because the gravitational well becomes too deep and feedback is no longer effective at expanding the halo. The post-compression halo density slopes predominantly fall below  $-1$ , with a few exceptions. The mean post-compression density slopes for each  $\alpha_{\epsilon}$  configuration fall below  $-1$ , as evidenced in Figure 3.12. Only the  $\alpha_{\epsilon} = 0.6$  configuration has a mean post-compression density slope ( $\bar{\Gamma}_{\text{post}} \approx -1.23 \pm 0.25$ ), falling within one standard deviation of  $\Gamma_{\text{post}} = -1$ . The findings underscore that hydrodynamical simulations, in which the accretion of baryons during the early stages of galaxy formation is not accounted for, underestimate the central densities of the initial dark matter halos.

Focusing on the results that fall below  $\log(M_{\star}/M_{200}) = -1.48$ , where the dashed curve indicates potential for halo expansion. In this range, the configurations that are cuspiest, aligning with DMO predictions, exhibit super cuspy characteristics. Even if peak feedback effects were applied to these halos, a regular cusp would still be the outcome. This suggests that, had the accretion of baryonic been incorporating into MUGS, stellar feedback would be ineffective at transforming a cusp into a core. The plot suggests that only more cored configurations, resulting in post-compression halos with a regular cusp, could potentially be transformed into cored halos by stellar feedback.

<sup>8</sup>This study was introduced in section 1.5, Figure 1.12

Considering the results corresponding to  $\log(M_\star/M_{200}) > -1.48$ , the range in which Di Cintio et al. (2014)’s study predicts compression. In this range, the results suggest that if hydrodynamical simulations included both stellar feedback mechanisms and the accretion of baryons during early galaxy formation, they could result in super-cuspy halos, even when starting from cored primordial halos. However, as noted by Di Cintio et al. (2014), this SHM ratio range at which AGN feedback becomes significant.

The outcomes of this project, which solely account for halo compression in the fitting procedure, may yield more cuspy halos than would be the case if feedback effects were somehow included. Di Cintio et al. (2014)’s study suggests that incorporating stellar feedback mechanisms into the fitting procedure could lead to halo expansion for galaxies with  $\log(M_\star/M_{200}) < -1.48$ . Ignoring the impracticality of incorporating feedback processes into the rotation curve fitting procedure, any halo expansion would reduce the amount dark matter in the galaxy while simultaneously facilitating greater baryonic matter resulting in a larger SHM ratio. As evidenced in Figure 3.13, SHM ratio is instrumental in driving baryonic compression of dark matter halos. Thus, expansion induced by feedback would likely be countered by the subsequent increasing effects of baryonic compression, making it improbable that stellar feedback alone could systematically increase the mass-to-light ratio for galaxies in this SHM ratio range.

Although Di Cintio et al. (2014) shows that stellar feedback can potentially expand halos, thereby increasing the systematically low best-fit mass-to-light ratios for a minority of cases, the majority of results have SHM ratios too high for stellar feedback alone to solve the problem. Additionally, the methodology in Di Cintio et al. (2014), which involves starting with a NFW halo and converting some of its mass into baryonic matter, neglects the affects of baryonic compression on dark matter halo during the formative stage of a galaxy. The results here suggest that assuming a pristine NFW halo, with a density slope of -1, as their starting point for galaxy evolution is inaccurate unless a cored primordial halo is assumed. This assumption compromises the predicted effects of baryonic feedback on halo structure by Di Cintio et al. (2014). Thus, it is concluded that stellar feedback is an ineffective solution to the systematically low best-fit mass-to-light ratios found in this study. Consequently, more potent feedback processes, such as those from AGN, or the use of more cored primordial halos, are necessary to address the systematically low best-fit mass-to-light ratios observed in this study.

### 3.4.2 AGN Feedback

This subsection will investigate the potential of AGN feedback mechanisms to systematically increase the best-fit mass-to-light ratio in the results by contextualising the results within the context of findings from IllustrisTNG (Pillepich et al., 2018; Weinberger et al., 2016) and observational data from the Mapping Nearby Galaxies at Apache Point Observatory (MaNGA) (Abdurro’uf et al., 2022). The IllustrisTNG project is a comprehensive suite of cosmological simulations designed to investigate the formation and evolution of galaxies across a broad range of environments within the universe. Utilising advanced models, the TNG (The Next Generation) simulations integrate the dynamics of dark matter and gas, magneto-hydrodynamics, radiative processes, star formation, feedback mechanisms from stars and AGNs, and chemical enrichment to provide an in-depth look at galaxy formation and evolution (Weinberger et al., 2016). In contrast to MUGS (Stinson et al., 2010), the TNG simulations also model the accretion of gas into dark matter halos during the formative stage of a galaxy. As such the dark matter halos of TNG simulated galaxies include the effects of baryonic compression and baryonic feedback during galaxy formation and evolution.

In the TNG suite, there are three different simulations, TNG50 (Pillepich et al., 2019), TNG100, and TNG300 (Nelson et al., 2019). They cover volumes of  $51.7^3$  Mpc<sup>3</sup>,  $110.7^3$  Mpc<sup>3</sup>, and  $302.6^3$  Mpc<sup>3</sup>, respectively, with the smaller volumes allowing for higher resolution. These simulations are crucial for linking theoretical predictions to observable galactic phenomena. Consequently, they establish a robust benchmark for comparing the results obtained in this project.

The MaNGA project, an integral part of the Sloan Digital Sky Survey, investigated nearly 10,000 nearby galaxies (Zhu et al., 2023). These galaxies were carefully chosen to cover a wide range of stellar masses, spanning nearly three orders of magnitude. The selection process did not discriminate based on size, inclination, morphology, or environment, ensuring that the sample accurately represents the diversity of the local galaxy population. In a departure from previous studies that focused only on the central spectra of galaxies, MaNGA employed a novel approach using a two-dimensional array of optical fibres. This innovative technology enabled spatially resolved spectroscopy, allowing for the construction of detailed maps across the entire face of each galaxy. These maps provide in-depth analyses of galaxy structures, revealing radial velocities and regions of star formation, offering new insights into the dynamic processes within galaxies.

The following analysis will compare the result of this project with a study by Wang et al. (2020) drawing on early-type galaxies modelled in the TNG100 simulations.<sup>9</sup> Subsequently, the focus will shift to contextualising the results by comparing them with a study by Li et al. (2023), which uses a broader dataset encompassing both early and late-type galaxies from TNG50 and TNG100 simulations alongside observational data from MaNGA.

### TNG100

Wang et al. (2020) studied a sample of 559 simulated galaxies drawn from the TNG100 simulations (Nelson et al., 2019). They measured the density slope of the evolved dark matter halos at a radius  $0.4R_{1/2} < r < R_{1/2}$ , where  $R_{1/2}$  denotes the stellar half-radius, the radius enclosing half of the galaxy's stellar mass. To differentiate this density slope from previous measurements in the project, it will always be written with the radius at which it was measured. They reported a mean density slope for the entire sample of  $\bar{\Gamma}(0.4R_{1/2} < r < R_{1/2}) \approx 1.71 \pm 0.19$ . The notably steep density profiles derived from the TNG100 simulations underscore the importance of baryonic accretion in the evolution of galaxy formation, suggesting it has a profound effect on altering the structure of dark matter halos. Furthermore, Wang et al. (2020) approximated the inner slope,  $\gamma$ , of the fully evolved dark matter halos by fitting their density profiles using a generalised NFW profile defined as

$$\rho(r) = \frac{\rho_s}{\left(\frac{r}{r_s}\right)^\gamma \left(1 + \frac{r}{r_s}\right)^{3-\gamma}}. \quad (32)$$

A NFW profile is characterised by an inner slope,  $\gamma = 1$ , and as such the generalised NFW profile allows freedom for the dark matter profile to be more or less cuspy than the regular NFW profile. They plotted the resulting inner slopes against the halo mass and reported that the regression line has a slope of  $-0.21$ .

To facilitate a relevant comparison, the density slopes,  $\Gamma(0.4R_{1/2} < r < R_{1/2})$ , of the post-compressed halos in this research were evaluated. An attempt was made to fit the compressed halos from this project using the generalised NFW profile, but it did not produce adequate fits. Since only the power-law behaviour of the inner slope is of interest,

<sup>9</sup>Early-type galaxies encompass various elliptical forms, whereas late-type includes a spectrum of spiral and barred spiral galaxies.

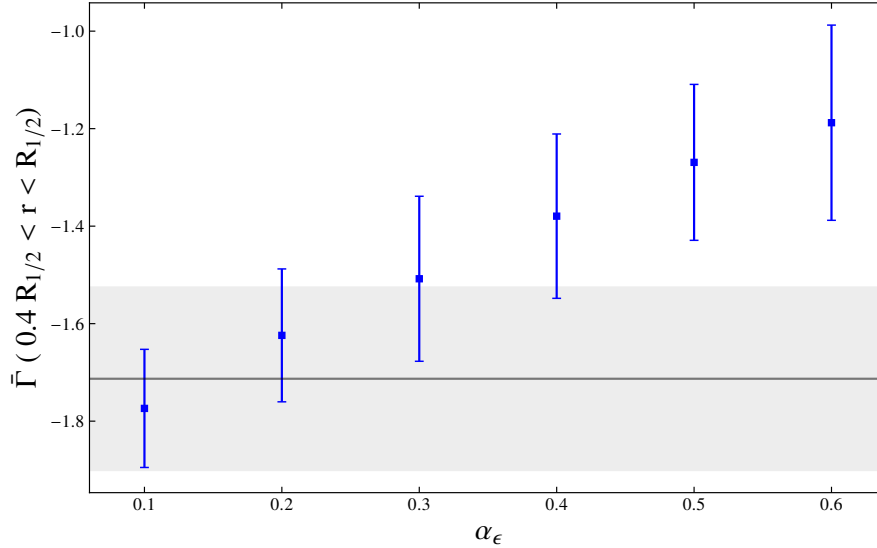


**Figure 3.15:** This figure depicts the mean density slopes of the best-fit compressed halos measured between radii  $0.4R_{1/2}$  and  $R_{1/2}$ , corresponding to each Einasto model configuration. Error bars represent the standard deviation. The horizontal line denotes the mean density slope derived by Wang et al. (2020) from a sample of 559 early-type galaxies drawn from TNG100 simulation (Nelson et al., 2019), with the grey shaded area denoting the dispersion around the mean.

$\gamma$  was determined by fitting each compressed halo with the  $(\alpha, \beta, \gamma)$  density profile, given in equation 12. Due to potential parameter degeneracy in this five-parameter profile, the  $\alpha$  parameter was fixed at  $\alpha = 1$ , and the scale radius was set to match that of the initial halo, providing a more reliable estimation of the inner slopes. The resulting best-fit parameters using the  $(\alpha, \beta, \gamma)$  density profile are collected in Table A.2 in the appendix.

Comparing the results of this project with Wang et al. (2020)’s research should be interpreted with caution, as they draw a sample of early-type galaxies from TNG100 simulations, while this study concentrates on late-type galaxies. Nevertheless, massive spiral galaxies possess masses comparable to those of early-type galaxies. Theoretically, the dark matter halos of both galaxy types are expected to follow an NFW profile or an Einasto profile with  $\alpha_\epsilon \approx 0.17$ . Therefore, the insights derived from the TNG100 simulations of early-type galaxies, which include the two primary baryonic effects that can affect dark matter halo structure, should provide a robust indication of the expected behaviours in massive spirals.

Figure 3.15 displays the average density slopes of the best-fit compressed halos for various Einasto configurations. The horizontal line represents the mean density slope reported by Wang et al. (2020), with the grey shaded area indicating the standard deviation. The mean density slopes,  $\bar{\Gamma}(0.4R_{1/2} < r < R_{1/2})$ , separated by  $\alpha_\epsilon$  value, are plotted with error bars denoting the standard deviation. Notably, the resulting scatter of the mean density slopes is similar to that reported by Wang et al. (2020). The figure clearly shows that the most cored models are in tension with the results derived from the TNG100 simulations, as the standard deviation of the density slopes for configurations  $\alpha_\epsilon \geq 0.5$  shows no overlap with the standard deviation reported by Wang et al. (2020). In contrast, the configurations with  $\alpha_\epsilon \leq 0.3$  are in agreement with the results reported by Wang et al. (2020). The NFW data has a mean density slope of  $\bar{\Gamma}(0.4R_{1/2} < r < R_{1/2}) = -1.61 \pm 0.14$ , which is consistent with both the cuspier Einasto models and the results derived from TNG100 simulations.

The cusplier profiles from this project agree with the results derived from the TNG100

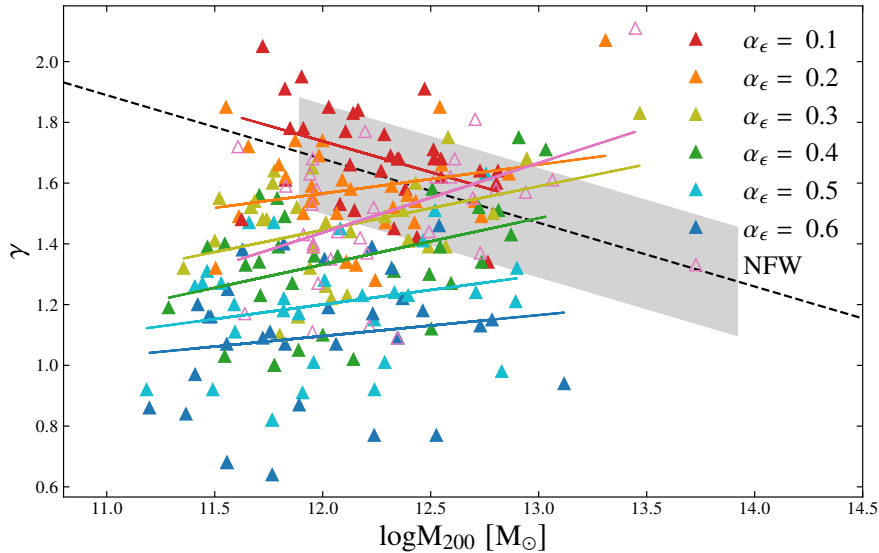


**Figure 3.16:** Post-compression dark matter halo inner slopes plotted against the best-fit halo masses.  $\gamma$  was determined by fitting the post-compression halos using the  $(\alpha, \beta, \gamma)$  density profile. The dashed line represents the extrapolated regression line derived in Wang et al. (2020) from the measurements of inner slopes for a sample of 559 galaxies drawn from the TNG100 simulations (Nelson et al., 2019). The grey band represents the scatter reported in Wang et al. (2020), as well as the halo mass range utilised in their study. Regression lines for the individual Einasto configurations and NFW data are also plotted.

simulations because both start with dark matter halos predicted by DMO simulations, based on  $\Lambda$ CDM model. The TNG100 simulations, while including stellar feedback and AGN feedback mechanisms, still result in super-cuspy evolved dark matter halos. The results here indicate that the super-cuspy dark matter halos in the TNG100 simulation are due to baryonic-driven contraction of dark matter halos.

The TNG simulations incorporate AGN feedback, which is one potential solution for reducing the cuspieness of the dark matter halos identified in this research. However, Wang et al. (2020) still report super-cuspy halos in the TNG100 simulations, suggesting that AGN feedback is insufficient to prevent DMO-predicted halos from evolving into super-cuspy halos. Thus, if baryonic feedback cannot be used to address the systematically lower mass-to-light ratios derived in this project, the only path to increase the best-fit mass-to-light ratios is to start with inherently cored profiles, which would require a modification of the nature of dark matter particles.

Figure 3.16 presents the relationship between the inner slopes, derived using the  $(\alpha, \beta, \gamma)$  density profile as a fitting function, of the best-fit compressed halos and their corresponding best-fit halo masses. For the NFW data and the Einasto data, separated by  $\alpha_\epsilon$  values, the separated regression lines are also over-plotted. This plot serves not only to show how the halo mass range studied by Wang et al. (2020) compares to the best-fit halo masses derived here but also to demonstrate the consistency in the measurements of the inner structure of the best-fit compressed halos. Analogous to post-compression density slopes shown in Figure 3.12, there is markedly less scatter for the more cuspy models. This is attributed to the fact that the cuspy models leave less room for baryonic mass, resulting in lower SHM ratios, thereby diminishing the effect of baryonic compression and consequently resulting in less variation in the post-compression inner slopes. Importantly, the inner slope and density slope measurements of post-compression halos demonstrate consistency across the different configurations, validating previous discussion and analysis centred on the measured density slopes.

In Figure 3.16, it is apparent that the more cored models result in inner slope values

( $\gamma$ ) that significantly deviate from those derived from TNG100 simulations. Specifically, mean values of  $\bar{\gamma}(\alpha_\epsilon = 0.5) \approx 1.09$  and  $\bar{\gamma}(\alpha_\epsilon = 0.6) \approx 1.2$ , with respective scatters of 0.20 and 0.21, show no overlap with the scatter reported by Wang et al. (2020). Only configurations with  $\alpha_\epsilon \leq 0.4$  fall within one standard deviation of the scatter reported by Wang et al. (2020). Moreover, the regression line for the configuration  $\alpha_\epsilon = 0.1$  results in inner slopes that exhibit a similar negative correlation with halo mass as those reported by Wang et al. (2020). While other models with characteristically cuspy configurations align within two standard deviations of the best-fit line from Wang et al. (2020), the more cored models are inconsistent with the results from the TNG100 simulations.

The findings that both the inner slopes and density slopes of the cuspiest configurations align well with the analogous values derived from TNG100 simulation results—even though baryonic feedback is not considered in the fitting procedure—might initially suggest mere self-consistency, as both models start with cuspy configurations. However, this alignment could indicate that in hydrodynamical simulations, feedback processes are not as instrumental in altering the dark matter halo structure as baryonic compression is. Nevertheless, the results in this project indicate that starting from cuspy halos results in super-cuspy halos after baryonic compression is considered. Although feedback is not included in the fitting procedure, this gives an indication of the magnitude of cuspiest that other potential feedback processes have to counteract. Thus, a rotation curve fitting procedure that incorporates only baryonic compression might be adequate for modelling observed galaxies in such a way that the resultant halo structures are consistent with those derived from hydrodynamical simulations, including both stellar and AGN feedback mechanisms. However, this consistency comes at the price of having systematically lower mass-to-light ratios that are incompatible with stellar population synthesis models Schombert et al. (2019). This incompatibility can only be resolved by using cored dark matter halos, which requires a fundamental change in the nature of dark matter particles.

### TNG50, TNG100 & MaNGA Observations

To check how the results of this project match with other observable data a study by Li et al. (2023) will be introduced. They investigated the differences between dark matter halo properties derived from TNG simulations (Weinberger et al., 2016; Pillepich et al., 2018) and observations from the MaNGA project (Abdurro'uf et al., 2022). Li et al. (2023) utilised a sample of 1733 galaxies from TNG50 simulations (Nelson et al., 2019), 11363 galaxies from TNG100 simulations (Pillepich et al., 2019), and a subsample of 5,688 galaxies from the MaNGA project (Abdurro'uf et al., 2022; Zhu et al., 2023). Both the TNG samples and the MaNGA subsample included a range of galaxy types from early- to late-type galaxies.

In Li et al. (2023)'s analysis they used the mass-weighted inner slopes of the dark matter halos. This is measured by integrating a dark matter density profile,  $\rho$ , from a radius of  $0.3R_{1/2}$  to  $R_{1/2}$ , where  $R_{1/2}$ . The mass-weighted inner slope is given by

$$\gamma_{\text{MW}} = -\frac{1}{M(0.3R_{1/2} < r < R_{1/2})} \int_{0.3R_{1/2}}^{R_{1/2}} 4\pi r^2 \rho(r) \frac{d \log \rho}{d \log r} dr \quad (33)$$

where  $M(0.3R_{1/2} < r < R_{1/2})$  is the halo mass enclosed within that radius range. This calculation is relatively straightforward for the simulated galaxies. For the MaNGA galaxy subsample, Li et al. (2023) used the mass-weighted inner slopes, as measured by Zhu et al. (2023). To measure  $\gamma_{\text{MW}}$  for the MaNGA galaxy subsample, Zhu et al. (2023) inferred the dark matter halo profile using a fitting process. The technicalities of this fitting procedure is detailed in subsections 3.1 and 3.3 of Zhu et al. (2023). Crucially, they used a generalised NFW profile defined as

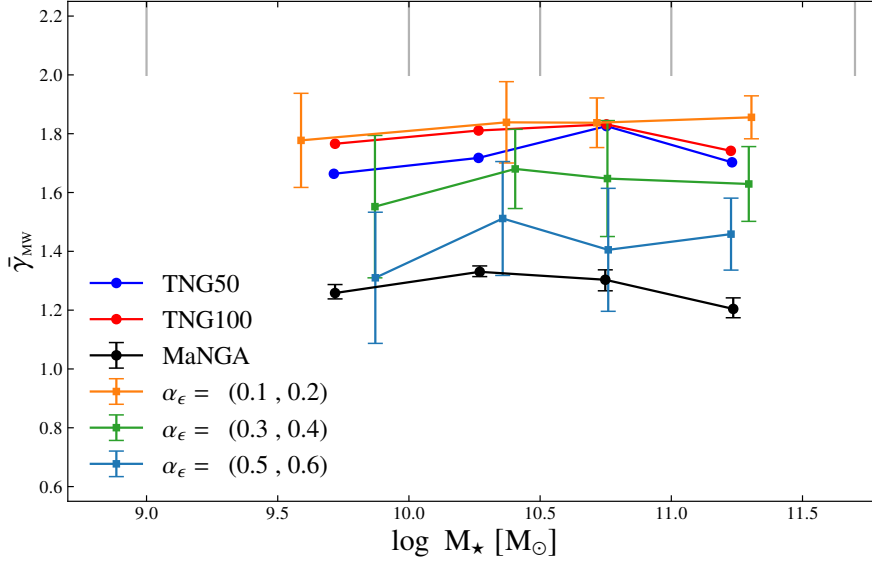


**Figure 3.17:** Mean mass-weighted inner slopes of grouped  $\alpha_\epsilon$  configurations plotted against the corresponding mean best-fit stellar masses for four mass bins. The results by Li et al. (2023) derived from MaNGA observation, TNG50 and TNG100 simulations are plotted in black, blue and red respectively. Error bars, where shown, denote the  $1\sigma$  scatter. Vertical grey lines indicate the stellar mass bins.

$$\rho(r) = \frac{\rho_s}{\left(\frac{r}{r_s}\right)^\gamma \left(\frac{1}{2} + \frac{r}{2r_s}\right)^{3-\gamma}} \quad (34)$$

to model the dark matter halo in the galaxy, from which they integrated out the mass-weighted inner slope according to equation 33.

Li et al. (2023) separated the mass-weighted inner slopes, as measure by from the three datasets (TNG50, TNG100, MaNGA) into four stellar mass bins. To facilitate a comparison with their analysis, the mass-weighted inner slopes of the best-fit compressed dark matter halos in this project were measured according to equation 33. The resulting  $\bar{\gamma}_{\text{MW}}$  values showed a significant variation across different Einasto configurations. Therefore, rather than grouping the resulting  $\bar{\gamma}_{\text{MW}}$  values into stellar mass bins, which is statistically unsound, the Einasto configurations were divided into three groups based on  $\alpha_\epsilon$  values: (0.1, 0.2), (0.3, 0.4), and (0.5, 0.6). Grouping the Einasto configurations in this manner is necessary due to sample size constraints, and is justified by the consistent similarity observed in the results within each group throughout the preceding analysis. The grouped data was divided into the same mass bins used by Li et al. (2023), and  $\bar{\gamma}_{\text{MW}}$  was subsequently computed. It is important to note that the galaxies in this project are late-type galaxies, whereas Li et al. (2023) considered a combined range of galaxy types.

Figure 3.17 plots  $\bar{\gamma}_{\text{MW}}$  separated into four stellar mass bins. The results reported by Li et al. (2023), derived from TNG50, TNG100, and MaNGA observations, are plotted in blue, red, and black, respectively. The  $1\sigma$  error bars for data derived from the TNG simulations are too small to be discernible in the Figure 11 of Li et al. (2023).<sup>10</sup> Therefore, the  $1\sigma$  error is no greater than the plotted points. According to Li et al. (2023)'s results, the TNG simulations yield characteristically super-cuspy dark matter halos, whereas the observational data suggest halos with a regular cusp. Their findings support the

<sup>10</sup>The data analysed by Li et al. (2023) was not directly accessible; it was extracted from Figure 11 in their study using <https://plotdigitizer.com/app>.

assertion by [Li et al. \(2022a\)](#), and corroborated in this study, that the core-cusp problem is broader than previously thought, potentially including massive galaxies.

The results from this project, displayed in [Figure 3.17](#), show no correlation between the mean mass-weighted inner slopes and stellar mass, in agreement with the findings of [Li et al. \(2023\)](#). Among the grouped Einasto configurations, the two cuspiest groups ((0.1, 0.2), (0.3, 0.4)) have mean mass-weighted inner slopes that fall within the  $1\sigma$  range of the data derived from the TNG simulations, with the only exception being the largest mass bin for the (0.1, 0.2) grouping. The cuspiest grouping, (0.1, 0.2), which aligns closest with the DMO simulations' predicted value for  $\alpha_\epsilon = 0.17$  ([Navarro et al., 2004](#); [Dutton and Maccio, 2014](#)), is incompatible with the MaNGA data, adding further weight to the assertion that the cusp-core problem also encompasses massive galaxies. In contrast, the most cored grouping, (0.5, 0.6), falls within a standard deviation of the observable data, reported by [Li et al. \(2023\)](#), except in the largest stellar mass bin. Considering that the mean value in the of the stellar mass bins result in  $\bar{\gamma}_{MW}$  values greater than the MaNGA data, this intriguingly suggests that even larger values of  $\alpha_\epsilon$ , when used in the rotation curve fitting procedure, might be better suited to align with MaNGA observations.

The results derived from TNG simulations ([Wang et al., 2020](#); [Li et al., 2023](#)), which incorporate both stellar and AGN feedback mechanisms, indicate that AGN feedback alone is insufficient to flatten the cusps in massive galaxies. If neither stellar nor AGN feedback can address the systematically low mass-to-light ratios observed in this study, then employing more cored profiles may be the solution. The analysis in [section 3.2.1](#) demonstrates that more cored profiles can accommodate greater amounts of baryonic matter. In conjunction with the analysis of MaNGA observations ([Li et al., 2023](#)), this suggests that using more cored configurations in the rotation curve fitting procedure could align with the MaNGA observations while systematically increasing the best-fit mass-to-light ratios.

## 4 Discussion & Outlook

This thesis was motivated by [Li et al. \(2022a\)](#)'s research, which incorporated baryonic compression of dark matter halos into the rotation curve fitting procedure. [Li et al. \(2022a\)](#) numerically solved the baryonic compression of NFW halos in response to a baryonic distribution matching that of real-world galaxies. By using these compressed dark matter halos in the rotation curve fitting process, they deviated from the traditional approach where dark matter and baryonic matter are treated independently. Their findings indicated that the most massive galaxies resulted in super-cuspy halos with best-fit mass-to-light ratios systematically lower than those predicted by stellar population synthesis models ([Schombert et al., 2019](#)). This suggests that achieving best-fit mass-to-light ratios consistent with predictions requires either a less cuspy primordial halo or feedback processes must be demonstrated to have sufficient power to expand the dark matter halo of massive galaxies, in order to accommodate more baryons in the galaxy.

The cusp-core problem involves a discrepancy between dwarf galaxy observations, which indicate a core, and simulations predicting a cusp. If a cored halo is required to model massive galaxies to align fitting parameters with predictions, it implies that the cusp-core problem extends beyond dwarf galaxies to include massive galaxies. This has significant implications for the nature of dark matter particles, as cuspy primordial halos are a prediction of DMO simulation, grounded in  $\Lambda$ CDM, which relies on dark matter particles being cold (GeV scale) with no self-interaction.

Using a subsample of the 31 most massive galaxies drawn from the SPARC database ([Lelli et al., 2016](#)), the aim of this project was to further investigate the problem identified in by [Li et al. \(2022a\)](#). For the first time, the Einasto dark matter profile was utilised as the primordial halo in the novel rotation curve fitting procedure introduced by [Li et al. \(2022a\)](#). Additionally, this study aimed to examine whether the best-fit parameter and compressed dark matter halos, resulting from the rotation curve fitting process, align with predictions from the  $\Lambda$ CDM cosmological framework and observational data.

The Einasto profile has three free parameters: halo mass, concentration, and shape parameter  $\{M_{200}, C_{200}, \alpha_\epsilon\}$ . Each galaxy in the subsample comprises both bulge and disk components, each requiring a mass-to-light ratio as a free parameter in the fitting procedure, denoted as  $\{\Upsilon_{\text{disk}}, \Upsilon_{\text{bulge}}\}$ . Due to the computational demand of the fitting procedure,  $\alpha_\epsilon$  was fixed at six different values in the range  $[0.1, 0.6]$  with a step size of 0.1, rather than treated as a free parameter. The rotation curve fitting procedure was conducted for each of the 31 galaxies seven times: six times using the Einasto profile and once using the NFW profile. During the fitting procedure,  $\Lambda$ CDM priors were imposed on the dark matter halo parameters in the form of the SHM and HMC relations, while flat priors were imposed on the mass-to-light ratios.

The Einasto model is an inherently cored density profile, but at the smallest resolvable radii of both observations and simulations, it is practically cuspy for the predicted value of  $\alpha_\epsilon \approx 0.17$  ([Dutton and Maccio, 2014](#)). Since  $\alpha_\epsilon$  controls the cuspieness of the Einasto profile, using six configurations of the Einasto profile in the fitting procedure effectively facilitated the testing of six degrees of cuspieness, ranging from super-cuspy ( $\alpha_\epsilon = 0.1$ ) to characteristically cored ( $\alpha_\epsilon = 0.6$ ). The cusp-core problem is central to the motivation for this project. Thus, using six variations of the Einasto profile allowed a comprehensive exploration of the dynamical effects of baryonic compression on dark matter halos and tested the compatibility of these compressed halos with both predictions from simulations and observations.

The rotation curve fitting procedure was executed successfully using all halo configurations. However, analysis of the results showed that particularly flat rotation curves

can lead to scenarios where the best-fit models suggest that galactic dynamics could be predominantly explained by dark matter alone. This was particularly effective for observed rotation curves where the innermost data point had a relatively small velocity, thereby minimising the role of the bulge in the galactic dynamics.

The analysis of best-fit post-compression halos revealed that they ranged from cuspy to super-cuspy, with only the more cored initial halos resulting in compressed halos with a regular cusp. The characteristically cored initial dark matter halos were impacted by baryonic compression far more than their cuspiers counterparts. Further analysis showed that the impact of baryonic compression on primordial halos depends on the interplay between the shape parameter value and the SHM ratio. The impact of these factors cannot be separated, as a more cored halo allows for more baryonic matter and invariably leads to a larger SHM ratio, a correlation also identified in the analysis.

The analysis of the best-fit parameters was conducted in the context of the imposed priors. The halo parameters were examined within the framework of the imposed SHM and HMC relations (Dutton and Maccio, 2014; Macciò et al., 2008). While both relations were recovered in the results across all Einasto profile configurations, the cuspiers configurations better recovered the relations than the cored configurations. This was not surprising since cuspy halos, the SHM and HMC relations are all derived from the  $\Lambda$ CDM framework. The more cored configurations resulted in mean best-fit mass-to-light ratios that were moderately closer to the expected fiducial values (Schombert et al., 2019; Lelli et al., 2016) than the cuspiers configurations. The best-fit mass-to-light ratios across all halo configurations were systematically lower than the fiducial values predicted by stellar population synthesis models (Schombert et al., 2019). Two ways to solve this problem were identified: including feedback mechanisms could expand a dark matter halo facilitating greater baryonic matter or modelling massive galaxies with cored dark matter profiles.

The analysis did not identify stellar feedback as a viable solution for the systematically low best-fit mass-to-light ratios found in this study. Firstly, most results did not fall within the SHM ratio range where stellar feedback could potentially expand the halo. Secondly, the predicted impact of stellar feedback, as proposed by Di Cintio et al. (2014), was questioned during the analysis of post-compression halo density slopes. This analysis demonstrated that neglecting the accretion of baryons during the early stages of galaxy formation in hydrodynamical simulations (Stinson et al., 2010; Di Cintio et al., 2014) underestimates the cuspieness of the initial dark matter halos used in such studies. Moreover, comparisons with TNG simulations (Pillepich et al., 2018, 2019; Nelson et al., 2019; Weinberger et al., 2016; Stinson et al., 2010) indicated that the effects of AGN feedback could not offset the systematically low best-fit mass-to-light ratios found in this study. Therefore, the remaining solution identified was the use of cored primordial halos when model the rotation curves of massive galaxies.

The results derived from configurations that were more cored were shown to best align with MaNGA observations (Abdurro'uf et al., 2022). Further analysis suggested that modelling the rotation curves of massive galaxies with even more cored configurations could also match MaNGA observations. This finding, combined with the observation that mass-to-light ratios derived from more cored configurations are higher than those from cuspiers configurations, suggests an optimal solution for addressing systematically low best-fit mass-to-light ratios in this study. Assuming an even more cored primordial halo profile to model the rotation curves of massive galaxies could yield results more consistent with predictions. However, primordial cored halos contradict predictions from DMO simulations under  $\Lambda$ CDM cosmology, which expect cuspy halos. To accommodate primordial cored halos, a reevaluation of dark matter particle properties

may be necessary.

To briefly recap, the key takeaways from the study are as follows:

1. Incorporating baryonic compression of dark matter halos into the rotation curve fitting procedure adequately modeled the galactic dynamics of massive galaxies, using both cuspy and cored primordial halos.
2. The SHM (Dutton and Maccio, 2014) and HMC (Macciò et al., 2008) relations were both successfully recovered in the results.
3. The best-fit mass-to-light ratios were systematically lower than those predicted by stellar synthesis models (Schombert et al., 2019).
4. Post-compression halos ranged from cuspy to super-cuspy; more cored primordial halos typically resulted in regular cusps, whereas cuspiest initial halos often led to super-cuspy configurations. Consequently, more cored halos allowed for more baryonic matter post-compression, resulting in moderately larger mean best-fit mass-to-light ratios.
5. Results from cuspiest configurations aligned better with the predictions of DMO simulations (Macciò et al., 2008; Dutton and Maccio, 2014) and hydrodynamical simulations (Pillepich et al., 2019; Nelson et al., 2019) compared to those from cored configurations. Despite the self-consistency between the predictions of  $\Lambda$ CDM and the cuspiest models, the cored configurations showed a better alignment with observational data (Abdurro'uf et al., 2022).
6. Comparative analysis suggests that stellar and AGN feedback are insufficient for transforming cusps of massive galaxies into cores, as such feedback mechanisms have not been identified as a solution to systematically improve the best-fit mass-to-light ratios to align with those predicted by stellar population synthesis models (Schombert et al., 2019). Consequently, the only viable approach to reconcile the discrepancy between the best-fit mass-to-light ratios and predictions is to use more cored primordial halos in the fitting procedure.

A cored primordial halo necessitates a fundamental change in the properties of dark matter particles used in the well-established  $\Lambda$ CDM framework. As such, it would be prudent to first raise questions about potential shortcomings in the fitting procedure. However, the robustness of the fitting methodology is supported by the consistency of the compressed halos derived from cuspiest models with the predictions from TNG simulations (Pillepich et al., 2019; Nelson et al., 2019). Additionally, the cored models align better with observational data, demonstrating their effectiveness in modelling the rotation curves of massive galaxies when accounting for the effects of baryonic compression. This evidence suggests that the assumptions underlying the predictions of inherently cuspy halos might be incorrect, challenging the fundamental nature of dark matter particles in these simulations.

### **Potential Resolutions: Self-Interaction or Lighter Particles**

To generate primordial halos with cored profiles from DMO simulations, altering the properties of dark matter particles is essential. One strategy involves altering dark matter particles to exhibit self-interactions that prevent the formation of dense cusps in primordial halos. Such self-interactions could reduce central densities, resulting in cored density profiles aligning more closely with observational data. For example, self-interacting dark matter (SIDM), first proposed by Spergel and Steinhardt (2000), could

produce cored profiles that transform into regular cuspy profiles during galaxy formation and evolution due to baryonic compression of the cored halo. SIDM introduces an attractive force; when dark matter particles collapse towards the centre, their interactions increase kinetic energy significantly (warming them), preventing them from staying within a small region and thus avoiding cusp formation. Moreover, SIDM with subtle enough interactions would not alter the large-scale structure described by  $\Lambda$ CDM.

Another approach to modifying primordial halo structures involves hypothesising that lighter dark matter particles can prevent dense cusp formation. Particles on the MeV scale are "warmer," which, like self-interactions, prevents them from remaining highly localised, thus avoiding cusp formation. Even ultralight models have been proposed such as is fuzzy dark matter (FDM), proposed by [Hu et al. \(2000\)](#), which consists of ultralight particles in the  $10^{-22}$  eV range. FDM stabilises gravitational collapse through its quantum wave properties, effectively preventing the formation of dense, cuspy centres in halos and leading to the creation of cored rather than cuspy primordial halos.

Beyond SIDM and FDM, other models featuring lighter dark matter particles or variations in their interactions could also be potential solutions. These models, while differing in specifics, share the commonality of trying to produce cored dark matter halo through modifications to dark matter properties such that they are consistent with cosmological observations.

### **Future Research Directions**

Looking ahead, several research avenues could expand on the findings of this project. One potential approach is to broaden the sample size to include a wider range of galaxy masses, which would enhance the statistical robustness of the results. Additionally, refining the rotation curve fitting procedure by incorporating disk inclination and galaxy distance as free parameters could improve the accuracy of the fits. Another promising avenue involves conducting the rotation curve fitting using dark matter profiles that are distinctly cored at resolvable radii. This could include models like the empirical pseudo-isothermal model, known for its effectiveness in modelling dwarf galaxies ([Adams et al., 2014](#)), or the Burkert model ([Burkert, 1995](#)), both of which feature a constant density core. Further, implementing density profiles derived from various dark matter models such as SIDM and FDM as the primordial halos in the rotation curve fitting procedure would allow for a comprehensive evaluation of these models. This approach could provide valuable insights into the structural dynamics of dark matter halos under different theoretical frameworks.

## Bibliography

- Abdurro'uf, N., Accetta, K., Aerts, C., Silva Aguirre, V., Ahumada, R., Ajgaonkar, N., Filiz Ak, N., Alam, S., Allende Prieto, C., Almeida, A., et al. (2022). The seventeenth data release of the sloan digital sky surveys: Complete release of manga, mastar, and apogee-2 data. *The Astrophysical Journal. Supplement Series*, 259(2).
- Adam, R., Ade, P. A., Aghanim, N., Akrami, Y., Alves, M., Argüeso, F., Arnaud, M., Arroja, F., Ashdown, M., Aumont, J., et al. (2016). Planck 2015 results-i. overview of products and scientific results. *Astronomy & Astrophysics*, 594:A1.
- Adams, J. J., Simon, J. D., Fabricius, M. H., van den Bosch, R. C., Barentine, J. C., Bender, R., Gebhardt, K., Hill, G. J., Murphy, J. D., Swaters, R., et al. (2014). Dwarf galaxy dark matter density profiles inferred from stellar and gas kinematics. *The Astrophysical Journal*, 789(1):63.
- Aghanim, N., Akrami, Y., Ashdown, M., Aumont, J., Baccigalupi, C., Ballardini, M., Banday, A., Barreiro, R., Bartolo, N., Basak, S., et al. (2020). Planck 2018 results-vi. cosmological parameters. *Astronomy & Astrophysics*, 641:A6.
- Alcock, C., Allsman, R., Alves, D. R., Axelrod, T., Becker, A. C., Bennett, D., Cook, K. H., Dalal, N., Drake, A. J., Freeman, K., et al. (2000). The macho project: microlensing results from 5.7 years of large magellanic cloud observations. *The Astrophysical Journal*, 542(1):281.
- Andernach, H. and Zwicky, F. (2017). English and spanish translation of zwicky's (1933) the redshift of extragalactic nebulae.
- Angulo, R., Springel, V., White, S., Jenkins, A., Baugh, C., and Frenk, C. (2012). Scaling relations for galaxy clusters in the millennium-xxl simulation. *Monthly Notices of the Royal Astronomical Society*, 426(3):2046–2062.
- Arcadi, G., Dutra, M., Ghosh, P., Lindner, M., Mambrini, Y., Pierre, M., Profumo, S., and Queiroz, F. S. (2018). The waning of the wimp? a review of models, searches, and constraints. *The European Physical Journal C*, 78:1–57.
- Baer, H., Barger, V., and Serce, H. (2016). Susy under siege from direct and indirect wimp detection experiments. *Physical Review D*, 94(11):115019.
- Bell, E. F. and de Jong, R. S. (2001). Stellar mass-to-light ratios and the tully-fisher relation. *The Astrophysical Journal*, 550(1):212.
- Boylan-Kolchin, M., Springel, V., White, S. D., Jenkins, A., and Lemson, G. (2009). Resolving cosmic structure formation with the millennium-ii simulation. *Monthly Notices of the Royal Astronomical Society*, 398(3):1150–1164.
- Bullock, J. (2013). Notes on the missing satellites problem. *Local Group Cosmology*, 20:95.
- Burkert, A. (1995). The structure of dark matter halos in dwarf galaxies. *The Astrophysical Journal*, 447(1):L25.
- Colless, M., Dalton, G., Maddox, S., Sutherland, W., Norberg, P., Cole, S., Bland-Hawthorn, J., Bridges, T., Cannon, R., Collins, C., et al. (2001). The 2df galaxy redshift survey: spectra and redshifts. *Monthly Notices of the Royal Astronomical Society*, 328(4):1039–1063.

- Colless, M. and Dunn, A. M. (1995). Structure and dynamics of the coma cluster. *arXiv preprint astro-ph/9508070*.
- De Blok, W., McGaugh, S., and Van der Hulst, J. (1996). H I observations of low surface brightness galaxies: probing low-density galaxies. *Monthly Notices of the Royal Astronomical Society*, 283(1):18–54.
- Di Cintio, A., Brook, C. B., Maccio, A. V., Stinson, G. S., Knebe, A., Dutton, A. A., and Wadsley, J. (2014). The dependence of dark matter profiles on the stellar-to-halo mass ratio: a prediction for cusps versus cores. *Monthly Notices of the Royal Astronomical Society*, 437(1):415–423.
- Dubinski, J. and Carlberg, R. (1991). The structure of cold dark matter halos. *Astrophysical Journal, Part 1 (ISSN 0004-637X)*, vol. 378, Sept. 10, 1991, p. 496–503. *Research supported by Pittsburgh Supercomputing Center and NSERC.*, 378:496–503.
- Dutton, A. A. and Maccio, A. V. (2014). Cold dark matter haloes in the planck era: evolution of structural parameters for einasto and nfw profiles. *Monthly Notices of the Royal Astronomical Society*, 441(4):3359–3374.
- Einasto, J. (1965). Kinematics and dynamics of stellar systems. *Trudy Inst. Astrofiz. Alma-Ata*, 51:87.
- Geller, M. J. and Huchra, J. P. (1989). Mapping the universe. *Science*, 246(4932):897–903.
- Gott III, J. R., Jurić, M., Schlegel, D., Hoyle, F., Vogeley, M., Tegmark, M., Bahcall, N., and Brinkmann, J. (2005). A map of the universe. *The Astrophysical Journal*, 624(2):463.
- Hu, W., Barkana, R., and Gruzinov, A. (2000). Fuzzy cold dark matter: the wave properties of ultralight particles. *Physical Review Letters*, 85(6):1158.
- Katz, H., Lelli, F., McGaugh, S. S., Di Cintio, A., Brook, C. B., and Schombert, J. M. (2017). Testing feedback-modified dark matter haloes with galaxy rotation curves: estimation of halo parameters and consistency with  $\Lambda$ CDM scaling relations. *Monthly Notices of the Royal Astronomical Society*, 466(2):1648–1668.
- Kubo, J. M., Stebbins, A., Annis, J., Dell’Antonio, I. P., Lin, H., Khiabani, H., and Frieman, J. A. (2007). The mass of the coma cluster from weak lensing in the sloan digital sky survey. *The Astrophysical Journal*, 671(2):1466.
- Lelli, F., McGaugh, S. S., and Schombert, J. M. (2016). Sparc: mass models for 175 disk galaxies with spitzer photometry and accurate rotation curves. *The Astronomical Journal*, 152(6):157.
- Li, P., McGaugh, S. S., Lelli, F., Schombert, J. M., and Pawlowski, M. S. (2022a). Incorporating baryon-driven contraction of dark matter halos in rotation curve fits. *Astronomy & Astrophysics*, 665:A143.
- Li, P., McGaugh, S. S., Lelli, F., Tian, Y., Schombert, J. M., and Ko, C.-M. (2022b). The effect of adiabatic compression on dark matter halos and the radial acceleration relation. *The Astrophysical Journal*, 927(2):198.

- Li, S., Li, R., Zhu, K., Lu, S., Cappellari, M., Mao, S., Wang, C., and Gao, L. (2023). Manga dynpop–vi. matter density slopes from dynamical models of 6000 galaxies vs cosmological simulations: the interplay between baryonic and dark matter. *arXiv preprint arXiv:2310.13278*.
- Lovell, M. R., Eke, V., Frenk, C. S., Gao, L., Jenkins, A., Theuns, T., Wang, J., White, S. D. M., Boyarsky, A., and Ruchayskiy, O. (2012). The haloes of bright satellite galaxies in a warm dark matter universe. *Monthly Notices of the Royal Astronomical Society*, 420(3):2318–2324.
- Macciò, A. V., Dutton, A. A., and Van Den Bosch, F. C. (2008). Concentration, spin and shape of dark matter haloes as a function of the cosmological model: Wmap 1, wmap 3 and wmap 5 results. *Monthly Notices of the Royal Astronomical Society*, 391(4):1940–1954.
- McGaugh, S. S., Lelli, F., and Schombert, J. M. (2016). Radial acceleration relation in rotationally supported galaxies. *Physical Review Letters*, 117(20):201101.
- McGaugh, S. S., Rubin, V. C., and De Blok, W. (2001). High-resolution rotation curves of low surface brightness galaxies. i. data. *The Astronomical Journal*, 122(5):2381.
- McGaugh, S. S. and Schombert, J. M. (2015). Weighing galaxy disks with the baryonic tully–fisher relation. *The Astrophysical Journal*, 802(1):18.
- Moore, B., Quinn, T., Governato, F., Stadel, J., and Lake, G. (1999). Cold collapse and the core catastrophe. *Monthly Notices of the Royal Astronomical Society*, 310(4):1147–1152.
- Moster, B. P., Naab, T., and White, S. D. (2013). Galactic star formation and accretion histories from matching galaxies to dark matter haloes. *Monthly Notices of the Royal Astronomical Society*, 428(4):3121–3138.
- Navarro, J. F., Frenk, C. S., and White, S. D. (1997). A universal density profile from hierarchical clustering. *The Astrophysical Journal*, 490(2):493.
- Navarro, J. F., Frenk, C. S., and White, S. D. M. (1996). The structure of cold dark matter halos. *The Astrophysical Journal*, 462:563.
- Navarro, J. F., Hayashi, E., Power, C., Jenkins, A., Frenk, C. S., White, S. D., Springel, V., Stadel, J., and Quinn, T. R. (2004). The inner structure of  $\lambda$ cdm haloes–iii. universality and asymptotic slopes. *Monthly Notices of the Royal Astronomical Society*, 349(3):1039–1051.
- Nelson, D., Springel, V., Pillepich, A., Rodriguez-Gomez, V., Torrey, P., Genel, S., Vogelsberger, M., Pakmor, R., Marinacci, F., Weinberger, R., et al. (2019). The illustrating simulations: public data release. *Computational Astrophysics and Cosmology*, 6:1–29.
- Noordermeer, E., Van Der Hulst, J., Sancisi, R., Swaters, R., and Van Albada, T. (2007). The mass distribution in early-type disc galaxies: declining rotation curves and correlations with optical properties. *Monthly Notices of the Royal Astronomical Society*, 376(4):1513–1546.
- Paczynski, B. (1986). Gravitational microlensing by the galactic halo. *The Astrophysical Journal*, 304:1–5.

- Paczynski, B. (1996). Gravitational microlensing in the local group. *Annual Review of Astronomy and Astrophysics*, 34(1):419–459.
- Pillepich, A., Nelson, D., Springel, V., Pakmor, R., Torrey, P., Weinberger, R., Vogelsberger, M., Marinacci, F., Genel, S., van der Wel, A., et al. (2019). First results from the tng50 simulation: the evolution of stellar and gaseous discs across cosmic time. *Monthly Notices of the Royal Astronomical Society*, 490(3):3196–3233.
- Pillepich, A., Springel, V., Nelson, D., Genel, S., Naiman, J., Pakmor, R., Hernquist, L., Torrey, P., Vogelsberger, M., Weinberger, R., et al. (2018). Simulating galaxy formation with the illustris model. *Monthly Notices of the Royal Astronomical Society*, 473(3):4077–4106.
- Popowski, P., Nelson, C., Bennett, D., Drake, A., Vandehei, T., Griest, K., Cook, K., Alcock, C., Allsman, R., Alves, D., et al. (2003). Recent microlensing results from the macho project. *arXiv preprint astro-ph/0304464*.
- Rubin, V. C., Ford Jr, W. K., and Thonnard, N. (1980). Rotational properties of 21 sc galaxies with a large range of luminosities and radii, from ngc 4605/r= 4kpc/to ugc 2885/r= 122 kpc. *Astrophysical Journal, Part 1, vol. 238, June 1, 1980, p. 471-487.*, 238:471–487.
- Schombert, J., McGaugh, S., and Lelli, F. (2019). The mass-to-light ratios and the star formation histories of disc galaxies. *Monthly Notices of the Royal Astronomical Society*, 483(2):1496–1512.
- Sellwood, J. (2014). Galaxy package for n-body simulation. *arXiv preprint arXiv:1406.6606*.
- Sellwood, J. and McGaugh, S. S. (2005). The compression of dark matter halos by baryonic infall. *The Astrophysical Journal*, 634(1):70.
- Spergel, D. N. and Steinhardt, P. J. (2000). Observational evidence for self-interacting cold dark matter. *Physical review letters*, 84(17):3760.
- Springel, V., Frenk, C. S., and White, S. D. (2006). The large-scale structure of the universe. *nature*, 440(7088):1137–1144.
- Springel, V., White, S. D., Jenkins, A., Frenk, C. S., Yoshida, N., Gao, L., Navarro, J., Thacker, R., Croton, D., Helly, J., et al. (2005). Simulations of the formation, evolution and clustering of galaxies and quasars. *nature*, 435(7042):629–636.
- Stinson, G., Bailin, J., Couchman, H., Wadsley, J., Shen, S., Nickerson, S., Brook, C., and Quinn, T. (2010). Cosmological galaxy formation simulations using smoothed particle hydrodynamics. *Monthly Notices of the Royal Astronomical Society*, 408(2):812–826.
- Tisserand, P., Le Guillou, L., Afonso, C., Albert, J., Andersen, J., Ansari, R., Aubourg, É., Bareyre, P., Beaulieu, J., Charlot, X., et al. (2007). Limits on the macho content of the galactic halo from the eros-2 survey of the magellanic clouds. *Astronomy & Astrophysics*, 469(2):387–404.
- Van Albada, T. S., Bahcall, J. N., Begeman, K., and Sancisi, R. (1985). Distribution of dark matter in the spiral galaxy ngc 3198. *Astrophysical Journal, Part 1 (ISSN 0004-637X)*, vol. 295, Aug. 15, 1985, p. 305-313., 295:305–313.

- Wang, Y., Vogelsberger, M., Xu, D., Mao, S., Springel, V., Li, H., Barnes, D., Hernquist, L., Pillepich, A., Marinacci, F., et al. (2020). Early-type galaxy density profiles from illustrating–i. galaxy correlations and the impact of baryons. *Monthly Notices of the Royal Astronomical Society*, 491(4):5188–5215.
- Weinberger, R., Springel, V., Hernquist, L., Pillepich, A., Marinacci, F., Pakmor, R., Nelson, D., Genel, S., Vogelsberger, M., Naiman, J., et al. (2016). Simulating galaxy formation with black hole driven thermal and kinetic feedback. *Monthly Notices of the Royal Astronomical Society*, 465(3):3291–3308.
- Young, P. (1980). Numerical models of star clusters with a central black hole. i-adiabatic models. *The Astrophysical Journal*, 242:1232–1237.
- Zhu, K., Lu, S., Cappellari, M., Li, R., Mao, S., and Gao, L. (2023). Manga dynpop–i. quality-assessed stellar dynamical modelling from integral-field spectroscopy of 10k nearby galaxies: a catalogue of masses, mass-to-light ratios, density profiles, and dark matter. *Monthly Notices of the Royal Astronomical Society*, 522(4):6326–6353.
- Zwicky, F. (1933). Die rotverschiebung von extragalaktischen nebeln. *Helvetica Physica Acta*, Vol. 6, p. 110-127, 6:110–127.

## A Appendix

The appendix includes two tables and 29 figures. The tables present the best-fit halo parameters, rotation curve fit quality, and additional quantities derived from the best-fit parameters and the prior- and post-compression halos. Table A.1 corresponds to results derived using the NFW profile as the primordial halo model, while Table A.2 corresponds to the Einasto profile. Figures 3.1 and 3.2 are the rotation curves for galaxies UGC 08699 and IC 4202, respectively, that were presented in the results. The rotation curves for the remaining 29 galaxies are included in this appendix following the tables.

| Galaxy<br>Name | $\Upsilon_{\text{disk}}$<br>$\left[\frac{M_{\odot}}{L_{\odot}}\right]$ | $\Upsilon_{\text{bulge}}$<br>$\left[\frac{M_{\odot}}{L_{\odot}}\right]$ | $V_{200}$<br>$\left[\frac{\text{km}}{\text{s}}\right]$ | $C_{200}$ | $\chi_{\nu}^2$ | $\Upsilon_{\text{eff}}$<br>$\left[\frac{M_{\odot}}{L_{\odot}}\right]$ | $\Gamma_{\text{prior}}$ | $\Gamma_{\text{post}}$ | $\gamma$ | $\beta$ | $r_s$<br>[kpc] | $\log \rho_s$<br>$\left[\frac{M_{\odot}}{\text{kpc}^3}\right]$ |
|----------------|--|---|--|-----------|----------------|---|-------------------------|------------------------|----------|---------|----------------|--|
| IC4202         | 0.61   | 0.1   | 141.1  | 9.2       | 16.85          | 0.5   | -1.25                   | -1.38                  | 1.11     | 3.81    | 20.92          | 7.01   |
| NGC0891        | 0.11   | 0.44  | 143.31   | 13.81     | 3.73           | 0.16  | -1.36                   | -1.78                  | 1.58     | 2.64    | 14.21          | 6.9  |
| NGC2683        | 0.45   | 0.25  | 108.35   | 8.5       | 2.21           | 0.44  | -1.24                   | -1.67                  | 1.72     | 2.93    | 17.47          | 6.44   |
| NGC2841        | 1.0  | 0.55  | 331.2  | 3.35      | 1.35           | 0.89  | -1.1                    | -1.82                  | 1.61     | 1.6     | 135.45         | 5.12   |
| NGC2955        | 0.1  | 0.35  | 154.28   | 13.62     | 2.35           | 0.16  | -1.35                   | -1.74                  | 1.44     | 2.99    | 15.52          | 7.07   |
| NGC4013        | 0.35   | 0.61  | 141.5  | 5.63      | 1.61           | 0.4   | -1.16                   | -1.57                  | 1.39     | 3.08    | 34.44          | 6.1  |
| NGC4157        | 0.36   | 0.1   | 143.96   | 5.45      | 0.49           | 0.36  | -1.16                   | -1.36                  | 1.27     | 3.36    | 36.06          | 6.19   |
| NGC4217        | 1.0  | 0.1   | 150.61   | 8.28      | 3.18           | 0.28  | -1.23                   | -1.53                  | 1.35     | 2.97    | 24.82          | 6.48   |
| NGC5005        | 0.41   | 0.41  | 249.48   | 5.96      | 0.07           | 0.41  | -1.17                   | -1.79                  | 1.55     | 1.89    | 57.27          | 5.82   |
| NGC5033        | 0.49   | 0.23  | 141.57   | 9.24      | 3.77           | 0.43  | -1.25                   | -1.6                   | 1.4      | 3.12    | 21.0           | 6.68   |
| NGC5985        | 0.15   | 0.76  | 190.73   | 18.83     | 2.75           | 0.18  | -1.46                   | -1.62                  | 1.09     | 3.1     | 13.88          | 7.53   |
| NGC6195        | 0.11   | 0.5   | 230.52   | 4.79      | 2.19           | 0.21  | -1.14                   | -1.62                  | 1.62     | 1.96    | 65.88          | 5.59   |
| NGC6674        | 0.73   | 0.85  | 251.69   | 2.6       | 5.49           | 0.74  | -1.08                   | -1.61                  | 1.81     | 1.76    | 132.7          | 4.77   |
| NGC6946        | 0.42   | 0.29  | 141.02   | 4.77      | 1.72           | 0.41  | -1.14                   | -1.42                  | 1.53     | 2.52    | 40.53          | 5.76   |
| NGC7331        | 0.33   | 0.15  | 213.65   | 4.62      | 0.64           | 0.32  | -1.14                   | -1.65                  | 1.44     | 2.61    | 63.28          | 5.76   |
| NGC7814        | 0.89   | 0.38  | 170.21   | 7.17      | 0.46           | 0.55  | -1.2                    | -1.69                  | 1.77     | 1.87    | 32.5           | 5.94   |
| UGC02487       | 1.0  | 0.97  | 444.62   | 1.59      | 5.43           | 0.99  | -1.05                   | -1.68                  | 2.11     | -0.84   | 383.25         | 3.75   |
| UGC02885       | 0.13   | 0.74  | 256.27   | 6.42      | 1.16           | 0.2   | -1.18                   | -1.76                  | 1.37     | 2.79    | 54.65          | 6.16   |
| UGC02916       | 0.13   | 0.26  | 136.71   | 12.13     | 9.14           | 0.21  | -1.32                   | -1.72                  | 1.43     | 2.98    | 15.44          | 6.93   |
| UGC02953       | 0.66   | 0.43  | 300.99   | 3.49      | 9.29           | 0.63  | -1.1                    | -1.62                  | 1.57     | 1.98    | 118.24         | 5.24   |
| UGC03205       | 0.57   | 0.84  | 175.43   | 4.45      | 2.64           | 0.61  | -1.13                   | -1.71                  | 1.52     | 2.67    | 53.97          | 5.71   |
| UGC03546       | 0.39   | 0.27  | 141.29   | 7.56      | 1.11           | 0.36  | -1.21                   | -1.68                  | 1.68     | 2.61    | 25.6           | 6.21   |
| UGC03580       | 0.35   | 0.12  | 110.98   | 5.47      | 2.89           | 0.29  | -1.16                   | -1.34                  | 1.17     | 3.26    | 27.79          | 6.17   |
| UGC05253       | 0.15   | 0.42  | 167.25   | 10.77     | 3.5            | 0.25  | -1.29                   | -1.63                  | 1.42     | 2.95    | 21.28          | 6.77   |
| UGC06614       | 0.29   | 0.23  | 172.78   | 5.55      | 0.63           | 0.26  | -1.16                   | -1.6                   | 1.13     | 3.32    | 42.66          | 6.23   |
| UGC06786       | 0.52   | 0.43  | 171.39   | 9.06      | 1.0            | 0.5   | -1.25                   | -1.51                  | 1.37     | 2.95    | 25.91          | 6.58   |
| UGC06787       | 0.99   | 0.36  | 218.83   | 5.75      | 22.97          | 0.68  | -1.17                   | -1.8                   | 1.62     | 2.03    | 52.09          | 5.79   |
| UGC06973       | 0.13   | 0.24  | 128.38   | 12.42     | 0.99           | 0.14  | -1.33                   | -1.7                   | 1.59     | 2.19    | 14.16          | 6.66   |
| UGC08699       | 0.5  | 0.48  | 139.9  | 6.48      | 0.69           | 0.49  | -1.19                   | -2.09                  | 1.63     | 2.57    | 29.56          | 6.04   |
| UGC09133       | 0.66   | 0.39  | 233.97   | 2.73      | 7.7            | 0.58  | -1.08                   | -1.72                  | 1.68     | 2.62    | 117.25         | 5.04   |
| UGC11914       | 0.22   | 0.71  | 271.05   | 9.35      | 0.98           | 0.34  | -1.26                   | -1.55                  | 1.58     | 1.12    | 39.61          | 6.22   |

**Table A.1:** Best-fit parameters for stellar disks, bulges, primordial NFW halos, and compressed halos, along with additional values derived during the analysis.  $V_{200}$  and  $C_{200}$  pertain to the primordial NFW halo.  $\chi_{\nu}^2$  indicates the quality of the rotation curve fit.  $\Upsilon_{\text{eff}}$  represents the effective mass-to-light ratio.  $\Gamma_{\text{prior}}$  and  $\Gamma_{\text{post}}$  are the dark matter halo density slopes before and after compression, measured at 1.5% of  $R_{200}$ . Parameters  $\gamma$ ,  $\beta$ ,  $r_s$ , and  $\rho_s$  describe the compressed halos when fitted with  $(\alpha, \beta, \gamma)$  models, with the transition parameter fixed at  $\alpha = 1$ .

**Table A.2:** Best-fit parameters for stellar disks, bulges, primordial Einasto halos, and compressed halos, along with additional values derived during the analysis.  $V_{200}$ ,  $C_{200}$  and  $\alpha_\epsilon$  pertain to the primordial Einasto halo.  $\chi_\nu^2$  indicates the quality of the rotation curve fit.  $\Upsilon_{\text{eff}}$  represents the effective mass-to-light ratio.  $\Gamma_{\text{prior}}$  and  $\Gamma_{\text{post}}$  are the dark matter halo density slopes before and after compression, measured at 1.5% of  $R_{200}$ . Parameters  $\gamma$ ,  $\beta$ ,  $r_s$ , and  $\rho_s$  describe the compressed halos when fitted with  $(\alpha, \beta, \gamma)$  models, with the transition parameter fixed at  $\alpha = 1$ .

| Galaxy<br>Name | $\Upsilon_{\text{disk}}$<br>$\left[\frac{M_\odot}{L_\odot}\right]$ | $\Upsilon_{\text{bulge}}$<br>$\left[\frac{M_\odot}{L_\odot}\right]$ | $V_{200}$<br>$\left[\frac{\text{km}}{\text{s}}\right]$ | $C_{200}$    | $\alpha_\epsilon$ | $\chi_\nu^2$ | $\Upsilon_{\text{eff}}$<br>$\left[\frac{M_\odot}{L_\odot}\right]$ | $\Gamma_{\text{prior}}$ | $\Gamma_{\text{post}}$ | $\gamma$    | $\beta$      | $r_s$<br>[kpc] | $\log \rho_s$<br>$\left[\frac{M_\odot}{\text{kpc}^3}\right]$ |
|----------------|--|---|--|--------------|-------------------|--------------|---|-------------------------|------------------------|-------------|--------------|----------------|--|
| IC4202         | 0.64   | 0.1   | 204.64   | 5.09         | 0.1               | 23.95        | 0.53  | -1.56                   | -1.6                   | 1.42        | 3.48         | 49.52          | 6.08   |
| IC4202         | 0.59   | 0.1   | 159.22   | 7.73         | 0.2               | 19.22        | 0.49  | -1.31                   | -1.5                   | 1.34        | 5.21         | 62.34          | 6.11   |
| IC4202         | 0.58   | 0.1   | 134.1  | 9.13         | 0.3               | 15.69        | 0.48  | -1.12                   | -1.26                  | 1.16        | 6.99         | 68.1           | 6.33   |
| IC4202         | 0.5  | 0.1   | 123.29   | 10.35        | 0.4               | 15.93        | 0.42  | -0.97                   | -1.15                  | 1.0         | 8.25         | 68.53          | 6.6  |
| IC4202         | 0.1  | 0.1   | 122.34   | 14.21        | 0.5               | 14.35        | 0.1   | -0.94                   | -1.1                   | 0.82        | 8.41         | 58.33          | 7.02   |
| <b>IC4202</b>  | <b>0.2</b>   | <b>0.1</b>  | <b>104.18</b>  | <b>14.35</b> | <b>0.6</b>        | <b>11.33</b> | <b>0.18</b>   | <b>-0.82</b>            | <b>-1.04</b>           | <b>0.68</b> | <b>11.53</b> | <b>60.89</b>   | <b>7.26</b>  |
| NGC0891        | 0.13   | 0.21  | 163.15   | 14.93        | 0.1               | 3.81         | 0.14  | -1.73                   | -1.95                  | 1.83        | 2.94         | 34.39          | 6.01   |
| NGC0891        | 0.15   | 0.37  | 144.48   | 11.81        | 0.2               | 3.91         | 0.18  | -1.43                   | -1.82                  | 1.69        | 3.58         | 48.76          | 5.86   |
| NGC0891        | 0.18   | 0.38  | 122.6  | 11.42        | 0.3               | 3.86         | 0.21  | -1.19                   | -1.76                  | 1.6         | 4.49         | 54.44          | 5.9  |
| NGC0891        | 0.1  | 0.63  | 113.47   | 11.6         | 0.4               | 4.28         | 0.17  | -1.01                   | -1.7                   | 1.52        | 5.0          | 57.16          | 5.99   |
| <b>NGC0891</b> | <b>0.11</b>  | <b>0.41</b>   | <b>97.08</b>   | <b>13.3</b>  | <b>0.5</b>        | <b>2.47</b>  | <b>0.15</b>   | <b>-0.91</b>            | <b>-1.54</b>           | <b>1.31</b> | <b>7.04</b>  | <b>49.55</b>   | <b>6.45</b>  |
| NGC0891        | 0.2  | 0.42  | 104.46   | 9.28         | 0.6               | 3.94         | 0.23  | -0.63                   | -1.47                  | 1.25        | 8.91         | 94.5           | 6.03   |
| <b>NGC2683</b> | <b>0.4</b>   | <b>0.11</b>   | <b>118.26</b>  | <b>11.61</b> | <b>0.1</b>        | <b>2.19</b>  | <b>0.38</b>   | <b>-1.69</b>            | <b>-1.92</b>           | <b>2.05</b> | <b>2.88</b>  | <b>33.73</b>   | <b>5.62</b>  |
| NGC2683        | 0.33   | 0.28  | 103.81   | 14.45        | 0.2               | 2.31         | 0.33  | -1.49                   | -1.78                  | 1.85        | 3.87         | 36.0           | 5.86   |
| NGC2683        | 0.1  | 0.27  | 89.29  | 25.8         | 0.3               | 1.65         | 0.11  | -1.52                   | -1.63                  | 1.32        | 5.37         | 19.77          | 7.09   |
| NGC2683        | 0.1  | 0.45  | 84.67  | 20.96        | 0.4               | 1.82         | 0.12  | -1.28                   | -1.52                  | 1.19        | 6.31         | 23.92          | 7.1  |
| NGC2683        | 0.1  | 0.1   | 78.3   | 22.3         | 0.5               | 1.29         | 0.1   | -1.18                   | -1.26                  | 0.92        | 8.15         | 23.86          | 7.5  |
| NGC2683        | 0.1  | 0.58  | 79.09  | 17.32        | 0.6               | 1.72         | 0.13  | -0.91                   | -1.32                  | 0.86        | 10.66        | 38.36          | 7.28   |
| NGC2841        | 0.81   | 0.46  | 272.88   | 4.27         | 0.1               | 1.31         | 0.72  | -1.53                   | -1.76                  | 1.64        | 2.46         | 55.19          | 5.88   |
| <b>NGC2841</b> | <b>0.95</b>  | <b>0.5</b>  | <b>283.78</b>  | <b>3.72</b>  | <b>0.2</b>        | <b>1.18</b>  | <b>0.84</b>   | <b>-1.14</b>            | <b>-1.92</b>           | <b>1.63</b> | <b>2.24</b>  | <b>96.6</b>    | <b>5.41</b>  |
| NGC2841        | 0.98   | 0.62  | 302.39   | 3.7          | 0.3               | 1.36         | 0.89  | -0.85                   | -1.78                  | 1.68        | 1.39         | 145.03         | 4.99   |
| NGC2841        | 0.98   | 0.77  | 293.82   | 3.69         | 0.4               | 1.29         | 0.93  | -0.64                   | -1.35                  | 1.75        | 0.6          | 202.91         | 4.64   |
| NGC2841        | 1.0  | 0.85  | 261.51   | 3.9          | 0.5               | 1.15         | 0.96  | -0.5                    | -1.37                  | 1.63        | 1.5          | 267.61         | 4.61   |
| NGC2841        | 0.99   | 0.89  | 221.42   | 4.22         | 0.6               | 1.25         | 0.97  | -0.39                   | -2.11                  | 1.46        | 4.13         | 339.7          | 4.74   |
| <b>NGC2955</b> | <b>0.13</b>  | <b>0.28</b>   | <b>186.31</b>  | <b>11.7</b>  | <b>0.1</b>        | <b>2.3</b>   | <b>0.16</b>   | <b>-1.69</b>            | <b>-1.86</b>           | <b>1.69</b> | <b>3.21</b>  | <b>38.63</b>   | <b>6.16</b>  |
| NGC2955        | 0.1  | 0.34  | 156.91   | 12.67        | 0.2               | 2.48         | 0.15  | -1.45                   | -1.77                  | 1.61        | 3.95         | 49.09          | 6.09   |
| NGC2955        | 0.1  | 0.38  | 133.57   | 12.46        | 0.3               | 2.75         | 0.16  | -1.23                   | -1.71                  | 1.52        | 4.93         | 54.36          | 6.14   |
| NGC2955        | 0.1  | 0.44  | 125.08   | 10.85        | 0.4               | 3.14         | 0.18  | -0.98                   | -1.56                  | 1.39        | 6.17         | 66.55          | 6.16   |
| NGC2955        | 0.1  | 0.6   | 134.42   | 8.09         | 0.5               | 3.51         | 0.21  | -0.71                   | -1.3                   | 1.17        | 8.23         | 111.04         | 6.05   |
| NGC2955        | 0.1  | 0.63  | 128.07   | 7.7          | 0.6               | 3.48         | 0.22  | -0.56                   | -1.24                  | 1.07        | 10.9         | 139.3          | 6.1  |
| NGC4013        | 0.2  | 0.37  | 135.83   | 11.23        | 0.1               | 2.24         | 0.23  | -1.68                   | -1.84                  | 1.95        | 2.75         | 35.62          | 5.7  |
| NGC4013        | 0.4  | 0.36  | 140.78   | 5.71         | 0.2               | 1.84         | 0.39  | -1.24                   | -1.53                  | 1.59        | 3.6          | 67.13          | 5.47   |
| NGC4013        | 0.63   | 0.1   | 159.67   | 4.23         | 0.3               | 1.48         | 0.53  | -0.89                   | -1.15                  | 1.23        | 4.65         | 111.87         | 5.45   |
| NGC4013        | 0.66   | 0.24  | 215.32   | 3.44         | 0.4               | 0.97         | 0.58  | -0.62                   | -1.25                  | 1.12        | 3.58         | 187.8          | 5.17   |
| NGC4013        | 0.58   | 0.47  | 175.85   | 3.89         | 0.5               | 0.89         | 0.56  | -0.5                    | -1.06                  | 1.15        | 4.29         | 226.55         | 5.06   |
| <b>NGC4013</b> | <b>0.49</b>  | <b>0.88</b>   | <b>153.5</b>   | <b>4.03</b>  | <b>0.6</b>        | <b>0.86</b>  | <b>0.57</b>   | <b>-0.38</b>            | <b>-1.23</b>           | <b>1.07</b> | <b>7.12</b>  | <b>283.25</b>  | <b>5.1</b>   |
| NGC4157        | 0.33   | 0.1   | 155.65   | 4.66         | 0.1               | 0.83         | 0.33  | -1.54                   | -1.6                   | 1.53        | 3.36         | 47.29          | 5.79   |

Table A.2 – continued from previous page

| Galaxy<br>Name | $\Upsilon_{\text{disk}}$<br>$\left[\frac{M_{\odot}}{L_{\odot}}\right]$ | $\Upsilon_{\text{bulge}}$<br>$\left[\frac{M_{\odot}}{L_{\odot}}\right]$ | $V_{200}$<br>$\left[\frac{\text{km}}{\text{s}}\right]$ | $C_{200}$    | $\alpha_{\epsilon}$ | $\chi_{\nu}^2$ | $\Upsilon_{\text{eff}}$<br>$\left[\frac{M_{\odot}}{L_{\odot}}\right]$ | $\Gamma_{\text{prior}}$ | $\Gamma_{\text{post}}$ | $\gamma$    | $\beta$     | $r_s$<br>[kpc] | $\log \rho_s$<br>$\left[\frac{M_{\odot}}{\text{kpc}^3}\right]$ |
|----------------|--|---|--|--------------|---------------------|----------------|---|-------------------------|------------------------|-------------|-------------|----------------|--|
| <b>NGC4157</b> | <b>0.31</b>  | <b>0.1</b>  | <b>136.67</b>  | <b>6.3</b>   | <b>0.2</b>          | <b>0.7</b>     | <b>0.31</b>   | <b>-1.26</b>            | <b>-1.49</b>           | <b>1.5</b>  | <b>4.22</b> | <b>63.74</b>   | <b>5.66</b>  |
| NGC4157        | 0.28   | 0.1   | 118.25   | 7.59         | 0.3                 | 0.75           | 0.28  | -1.06                   | -1.43                  | 1.48        | 4.97        | 70.79          | 5.66   |
| NGC4157        | 0.45   | 0.11  | 163.29   | 4.28         | 0.4                 | 0.32           | 0.44  | -0.68                   | -1.02                  | 1.02        | 6.21        | 153.34         | 5.55   |
| NGC4157        | 0.49   | 0.12  | 175.96   | 4.05         | 0.5                 | 0.26           | 0.48  | -0.5                    | -1.0                   | 0.92        | 7.04        | 222.04         | 5.46   |
| NGC4157        | 0.53   | 0.1   | 219.23   | 3.78         | 0.6                 | 0.23           | 0.52  | -0.37                   | -0.78                  | 0.77        | 7.86        | 356.14         | 5.42   |
| NGC4217        | 0.85   | 0.1   | 188.61   | 5.03         | 0.1                 | 4.19           | 0.25  | -1.55                   | -1.62                  | 1.45        | 3.59        | 48.68          | 5.96   |
| NGC4217        | 0.97   | 0.15  | 176.45   | 6.03         | 0.2                 | 3.34           | 0.31  | -1.25                   | -1.49                  | 1.28        | 4.75        | 71.7           | 5.89   |
| NGC4217        | 0.99   | 0.12  | 139.93   | 7.96         | 0.3                 | 2.94           | 0.29  | -1.07                   | -1.45                  | 1.32        | 5.36        | 76.33          | 5.84   |
| NGC4217        | 0.99   | 0.1   | 117.33   | 9.14         | 0.4                 | 2.76           | 0.28  | -0.92                   | -1.38                  | 1.23        | 6.45        | 73.3           | 6.04   |
| <b>NGC4217</b> | <b>1.0</b>   | <b>0.1</b>  | <b>107.2</b>   | <b>9.13</b>  | <b>0.5</b>          | <b>2.52</b>    | <b>0.28</b>   | <b>-0.76</b>            | <b>-1.32</b>           | <b>1.11</b> | <b>7.82</b> | <b>79.44</b>   | <b>6.17</b>  |
| NGC4217        | 0.36   | 0.1   | 93.02  | 11.27        | 0.6                 | 2.64           | 0.15  | -0.71                   | -1.22                  | 0.97        | 9.81        | 69.31          | 6.56   |
| NGC5005        | 0.3  | 0.32  | 196.35   | 8.87         | 0.1                 | 0.1            | 0.3   | -1.64                   | -1.79                  | 1.58        | 3.92        | 42.44          | 6.19   |
| <b>NGC5005</b> | <b>0.32</b>  | <b>0.42</b>   | <b>202.81</b>  | <b>8.3</b>   | <b>0.2</b>          | <b>0.09</b>    | <b>0.33</b>   | <b>-1.33</b>            | <b>-1.6</b>            | <b>1.47</b> | <b>3.9</b>  | <b>66.88</b>   | <b>5.96</b>  |
| NGC5005        | 0.35   | 0.47  | 213.26   | 7.74         | 0.3                 | 0.1            | 0.36  | -1.06                   | -1.54                  | 1.39        | 3.33        | 97.32          | 5.77   |
| NGC5005        | 0.4  | 0.5   | 231.03   | 7.03         | 0.4                 | 0.11           | 0.41  | -0.83                   | -1.48                  | 1.27        | 3.93        | 142.35         | 5.67   |
| NGC5005        | 0.47   | 0.52  | 276.55   | 6.24         | 0.5                 | 0.11           | 0.48  | -0.63                   | -1.06                  | 0.98        | 10.42       | 224.32         | 5.89   |
| NGC5005        | 0.55   | 0.51  | 345.25   | 5.77         | 0.6                 | 0.09           | 0.55  | -0.47                   | -0.79                  | 0.94        | 0.85        | 361.01         | 5.55   |
| NGC5033        | 0.24   | 0.11  | 158.76   | 17.13        | 0.1                 | 3.96           | 0.21  | -1.76                   | -1.94                  | 1.77        | 3.18        | 32.59          | 6.14   |
| NGC5033        | 0.52   | 0.14  | 141.41   | 9.2          | 0.2                 | 4.23           | 0.43  | -1.36                   | -1.66                  | 1.55        | 4.09        | 54.64          | 5.88   |
| NGC5033        | 0.29   | 0.2   | 119.97   | 13.14        | 0.3                 | 2.75           | 0.27  | -1.25                   | -1.66                  | 1.48        | 4.9         | 47.87          | 6.18   |
| NGC5033        | 0.2  | 0.33  | 111.28   | 12.74        | 0.4                 | 2.28           | 0.23  | -1.05                   | -1.54                  | 1.33        | 6.01        | 51.27          | 6.35   |
| <b>NGC5033</b> | <b>0.16</b>  | <b>0.43</b>   | <b>106.91</b>  | <b>11.46</b> | <b>0.5</b>          | <b>2.14</b>    | <b>0.22</b>   | <b>-0.85</b>            | <b>-1.46</b>           | <b>1.2</b>  | <b>7.52</b> | <b>63.31</b>   | <b>6.38</b>  |
| NGC5033        | 0.29   | 0.35  | 104.11   | 9.66         | 0.6                 | 2.02           | 0.3   | -0.64                   | -1.32                  | 1.07        | 10.28       | 90.53          | 6.33   |
| NGC5985        | 0.51   | 0.81  | 222.93   | 9.1          | 0.1                 | 2.93           | 0.52  | -1.65                   | -1.67                  | 1.62        | 3.14        | 43.62          | 6.2  |
| NGC5985        | 0.23   | 0.49  | 182.93   | 17.26        | 0.2                 | 2.67           | 0.24  | -1.54                   | -1.64                  | 1.47        | 4.1         | 45.16          | 6.45   |
| <b>NGC5985</b> | <b>0.1</b>   | <b>0.23</b>   | <b>147.92</b>  | <b>22.25</b> | <b>0.3</b>          | <b>2.11</b>    | <b>0.11</b>   | <b>-1.46</b>            | <b>-1.5</b>            | <b>1.26</b> | <b>5.18</b> | <b>36.42</b>   | <b>6.94</b>  |
| NGC5985        | 0.1  | 0.31  | 134.35   | 20.39        | 0.4                 | 2.75           | 0.11  | -1.27                   | -1.36                  | 1.05        | 6.35        | 38.8           | 7.16   |
| NGC5985        | 0.1  | 0.86  | 136.28   | 15.53        | 0.5                 | 4.52           | 0.14  | -0.99                   | -1.24                  | 0.91        | 7.99        | 59.46          | 7.02   |
| NGC5985        | 0.11   | 0.28  | 122.35   | 18.19        | 0.6                 | 5.22           | 0.12  | -0.94                   | -1.06                  | 0.64        | 10.88       | 56.5           | 7.53   |
| NGC6195        | 0.1  | 0.4   | 217.48   | 5.39         | 0.1                 | 2.45           | 0.18  | -1.56                   | -1.82                  | 1.68        | 2.57        | 49.55          | 5.84   |
| NGC6195        | 0.1  | 0.46  | 197.78   | 6.06         | 0.2                 | 2.58           | 0.2   | -1.25                   | -1.66                  | 1.56        | 3.12        | 74.62          | 5.65   |
| NGC6195        | 0.1  | 0.52  | 194.54   | 5.44         | 0.3                 | 2.48           | 0.21  | -0.96                   | -1.47                  | 1.51        | 3.25        | 109.36         | 5.4  |
| NGC6195        | 0.16   | 0.61  | 285.93   | 3.59         | 0.4                 | 2.0            | 0.28  | -0.64                   | -1.33                  | 1.43        | 2.36        | 203.05         | 4.97   |
| <b>NGC6195</b> | <b>0.18</b>  | <b>0.65</b>   | <b>290.6</b>   | <b>3.61</b>  | <b>0.5</b>          | <b>1.97</b>    | <b>0.31</b>   | <b>-0.48</b>            | <b>-1.15</b>           | <b>1.21</b> | <b>4.59</b> | <b>284.56</b>  | <b>5.08</b>  |
| NGC6195        | 0.15   | 0.65  | 208.93   | 4.24         | 0.6                 | 1.92           | 0.28  | -0.39                   | -1.12                  | 1.18        | 6.6         | 329.19         | 5.09   |
| NGC6674        | 0.48   | 1.0   | 210.26   | 4.14         | 0.1                 | 8.71           | 0.52  | -1.52                   | -1.77                  | 1.91        | 2.32        | 52.41          | 5.58   |
| NGC6674        | 0.59   | 0.97  | 221.95   | 3.25         | 0.2                 | 7.35           | 0.62  | -1.11                   | -1.5                   | 1.85        | 2.18        | 93.84          | 5.09   |
| NGC6674        | 0.69   | 1.0   | 228.55   | 2.91         | 0.3                 | 6.81           | 0.71  | -0.8                    | -1.82                  | 1.75        | 2.28        | 143.33         | 4.82   |
| NGC6674        | 0.89   | 0.66  | 273.45   | 2.53         | 0.4                 | 6.61           | 0.87  | -0.55                   | -1.34                  | 1.51        | 2.55        | 220.65         | 4.7  |
| NGC6674        | 0.97   | 0.76  | 291.95   | 2.43         | 0.5                 | 6.61           | 0.95  | -0.39                   | -1.2                   | 1.32        | 4.02        | 318.13         | 4.69   |
| <b>NGC6674</b> | <b>0.99</b>  | <b>0.69</b>   | <b>267.22</b>  | <b>2.57</b>  | <b>0.6</b>          | <b>8.08</b>    | <b>0.97</b>   | <b>-0.29</b>            | <b>-1.08</b>           | <b>1.15</b> | <b>6.21</b> | <b>437.73</b>  | <b>4.74</b>  |
| NGC6946        | 0.18   | 0.1   | 128.23   | 12.2         | 0.1                 | 4.07           | 0.18  | -1.7                    | -1.8                   | 1.61        | 3.87        | 33.96          | 6.06   |

Table A.2 – continued from previous page

| Galaxy<br>Name  | $\Upsilon_{\text{disk}}$<br>$\left[\frac{M_{\odot}}{L_{\odot}}\right]$ | $\Upsilon_{\text{bulge}}$<br>$\left[\frac{M_{\odot}}{L_{\odot}}\right]$ | $V_{200}$<br>$\left[\frac{\text{km}}{\text{s}}\right]$ | $C_{200}$    | $\alpha_{\epsilon}$ | $\chi_{\nu}^2$ | $\Upsilon_{\text{eff}}$<br>$\left[\frac{M_{\odot}}{L_{\odot}}\right]$ | $\Gamma_{\text{prior}}$ | $\Gamma_{\text{post}}$ | $\gamma$    | $\beta$     | $r_s$<br>[kpc] | $\log \rho_s$<br>$\left[\frac{M_{\odot}}{\text{kpc}^3}\right]$ |
|-----------------|--|---|--|--------------|---------------------|----------------|---|-------------------------|------------------------|-------------|-------------|----------------|--|
| NGC6946         | 0.24   | 0.23  | 108.67   | 10.78        | 0.2                 | 2.53           | 0.24  | -1.4                    | -1.66                  | 1.49        | 4.85        | 43.92          | 5.98   |
| NGC6946         | 0.25   | 0.33  | 99.77  | 9.86         | 0.3                 | 2.04           | 0.25  | -1.14                   | -1.51                  | 1.41        | 5.58        | 52.0           | 5.97   |
| <b>NGC6946</b>  | <b>0.43</b>  | <b>0.38</b>   | <b>116.82</b>  | <b>5.14</b>  | <b>0.4</b>          | <b>1.63</b>    | <b>0.43</b>   | <b>-0.73</b>            | <b>-1.29</b>           | <b>1.34</b> | <b>6.17</b> | <b>114.52</b>  | <b>5.35</b>  |
| NGC6946         | 0.37   | 0.4   | 92.95  | 6.43         | 0.5                 | 1.59           | 0.37  | -0.64                   | -1.21                  | 1.26        | 8.33        | 97.28          | 5.67   |
| NGC6946         | 0.42   | 0.39  | 93.9   | 6.01         | 0.6                 | 1.7            | 0.42  | -0.48                   | -1.19                  | 1.2         | 9.54        | 130.98         | 5.54   |
| NGC7331         | 0.19   | 0.14  | 182.19   | 9.45         | 0.1                 | 1.76           | 0.19  | -1.66                   | -1.83                  | 1.76        | 2.98        | 40.82          | 5.97   |
| NGC7331         | 0.27   | 0.39  | 188.04   | 5.57         | 0.2                 | 1.1            | 0.28  | -1.23                   | -1.62                  | 1.52        | 3.5         | 75.5           | 5.65   |
| <b>NGC7331</b>  | <b>0.34</b>  | <b>0.19</b>   | <b>197.95</b>  | <b>4.71</b>  | <b>0.3</b>          | <b>0.67</b>    | <b>0.33</b>   | <b>-0.92</b>            | <b>-1.54</b>           | <b>1.41</b> | <b>3.55</b> | <b>116.73</b>  | <b>5.4</b>   |
| NGC7331         | 0.36   | 0.17  | 188.58   | 4.74         | 0.4                 | 0.65           | 0.35  | -0.71                   | -1.48                  | 1.31        | 4.34        | 156.46         | 5.33   |
| NGC7331         | 0.39   | 0.14  | 188.87   | 4.52         | 0.5                 | 0.67           | 0.38  | -0.53                   | -1.26                  | 1.24        | 4.82        | 217.67         | 5.2  |
| NGC7331         | 0.4  | 0.22  | 194.43   | 4.47         | 0.6                 | 0.82           | 0.39  | -0.41                   | -1.13                  | 1.22        | 4.66        | 307.48         | 5.0  |
| NGC7814         | 0.57   | 0.28  | 166.02   | 11.03        | 0.1                 | 0.77           | 0.37  | -1.68                   | -1.97                  | 1.84        | 2.88        | 37.98          | 5.88   |
| NGC7814         | 0.35   | 0.36  | 146.27   | 11.55        | 0.2                 | 0.53           | 0.36  | -1.42                   | -1.86                  | 1.74        | 3.28        | 49.64          | 5.78   |
| <b>NGC7814</b>  | <b>0.81</b>  | <b>0.38</b>   | <b>141.12</b>  | <b>8.69</b>  | <b>0.3</b>          | <b>0.48</b>    | <b>0.52</b>   | <b>-1.1</b>             | <b>-1.7</b>            | <b>1.65</b> | <b>3.59</b> | <b>72.77</b>   | <b>5.54</b>  |
| NGC7814         | 0.49   | 0.44  | 124.56   | 9.27         | 0.4                 | 0.55           | 0.46  | -0.92                   | -1.65                  | 1.55        | 4.64        | 76.37          | 5.68   |
| NGC7814         | 0.69   | 0.46  | 123.02   | 7.97         | 0.5                 | 0.6            | 0.53  | -0.71                   | -1.53                  | 1.47        | 5.31        | 103.7          | 5.53   |
| NGC7814         | 0.88   | 0.49  | 127.42   | 6.89         | 0.6                 | 0.8            | 0.62  | -0.53                   | -1.66                  | 1.4         | 5.84        | 154.74         | 5.33   |
| UGC02487        | 0.12   | 0.11  | 263.39   | 34.14        | 0.1                 | 6.61           | 0.12  | -1.88                   | -1.96                  | 1.34        | 3.85        | 30.72          | 7.07   |
| UGC02487        | 0.99   | 0.97  | 399.97   | 1.4          | 0.2                 | 5.32           | 0.99  | -0.94                   | -1.56                  | 2.07        | 1.37        | 126.43         | 4.83   |
| <b>UGC02487</b> | <b>1.0</b>   | <b>1.0</b>  | <b>451.74</b>  | <b>1.81</b>  | <b>0.3</b>          | <b>5.37</b>    | <b>1.0</b>  | <b>-0.69</b>            | <b>-1.43</b>           | <b>1.83</b> | <b>1.66</b> | <b>184.13</b>  | <b>4.75</b>  |
| UGC02487        | 0.97   | 0.91  | 323.45   | 2.92         | 0.4                 | 7.23           | 0.96  | -0.58                   | -1.31                  | 1.71        | 2.29        | 222.14         | 4.76   |
| UGC02487        | 0.1  | 0.41  | 182.47   | 13.16        | 0.5                 | 10.64          | 0.17  | -0.91                   | -1.22                  | 1.01        | 7.84        | 93.6           | 6.73   |
| UGC02487        | 0.1  | 0.28  | 175.8  | 13.31        | 0.6                 | 10.82          | 0.14  | -0.78                   | -1.0                   | 0.77        | 10.62       | 110.92         | 7.0  |
| UGC02885        | 0.13   | 0.58  | 271.38   | 6.38         | 0.1                 | 1.59           | 0.18  | -1.59                   | -1.8                   | 1.6         | 2.64        | 50.28          | 6.07   |
| UGC02885        | 0.13   | 0.71  | 257.35   | 6.38         | 0.2                 | 1.31           | 0.2   | -1.26                   | -1.84                  | 1.49        | 3.01        | 80.32          | 5.82   |
| <b>UGC02885</b> | <b>0.11</b>  | <b>0.79</b>   | <b>226.74</b>  | <b>6.87</b>  | <b>0.3</b>          | <b>1.21</b>    | <b>0.19</b>   | <b>-1.03</b>            | <b>-1.62</b>           | <b>1.39</b> | <b>3.85</b> | <b>105.79</b>  | <b>5.76</b>  |
| UGC02885        | 0.1  | 0.88  | 213.84   | 6.52         | 0.4                 | 1.17           | 0.19  | -0.8                    | -1.47                  | 1.3         | 4.73        | 142.32         | 5.66   |
| UGC02885        | 0.11   | 0.97  | 198.35   | 6.3          | 0.5                 | 1.16           | 0.21  | -0.63                   | -1.68                  | 1.23        | 6.19        | 184.79         | 5.61   |
| UGC02885        | 0.1  | 0.99  | 191.26   | 6.18         | 0.6                 | 1.17           | 0.21  | -0.49                   | -1.54                  | 1.09        | 8.64        | 244.54         | 5.67   |
| <b>UGC02916</b> | <b>0.66</b>  | <b>0.18</b>   | <b>130.36</b>  | <b>14.98</b> | <b>0.1</b>          | <b>6.22</b>    | <b>0.38</b>   | <b>-1.73</b>            | <b>-1.99</b>           | <b>1.78</b> | <b>3.47</b> | <b>31.91</b>   | <b>6.07</b>  |
| UGC02916        | 0.13   | 0.2   | 128.36   | 14.69        | 0.2                 | 8.11           | 0.17  | -1.49                   | -1.86                  | 1.62        | 4.03        | 40.47          | 6.11   |
| UGC02916        | 0.15   | 0.27  | 113.42   | 11.9         | 0.3                 | 9.05           | 0.22  | -1.21                   | -1.75                  | 1.52        | 4.93        | 49.57          | 6.06   |
| UGC02916        | 0.11   | 0.27  | 103.38   | 11.72        | 0.4                 | 9.68           | 0.2   | -1.02                   | -1.64                  | 1.4         | 6.05        | 51.76          | 6.22   |
| UGC02916        | 0.11   | 0.33  | 102.08   | 9.52         | 0.5                 | 10.19          | 0.24  | -0.77                   | -1.5                   | 1.27        | 7.75        | 72.7           | 6.13   |
| UGC02916        | 0.1  | 0.35  | 97.5   | 9.01         | 0.6                 | 10.44          | 0.24  | -0.62                   | -1.42                  | 1.16        | 10.35       | 90.94          | 6.18   |
| UGC02953        | 0.55   | 0.39  | 256.0  | 3.94         | 0.1                 | 6.79           | 0.53  | -1.52                   | -1.74                  | 1.64        | 2.55        | 55.26          | 5.84   |
| <b>UGC02953</b> | <b>0.65</b>  | <b>0.39</b>   | <b>251.35</b>  | <b>3.83</b>  | <b>0.2</b>          | <b>5.72</b>    | <b>0.62</b>   | <b>-1.14</b>            | <b>-1.63</b>           | <b>1.54</b> | <b>2.77</b> | <b>92.75</b>   | <b>5.5</b>   |
| UGC02953        | 0.65   | 0.53  | 268.42   | 3.9          | 0.3                 | 8.57           | 0.64  | -0.87                   | -1.61                  | 1.5         | 2.57        | 137.98         | 5.24   |
| UGC02953        | 0.67   | 0.52  | 222.17   | 4.55         | 0.4                 | 7.85           | 0.65  | -0.7                    | -1.35                  | 1.39        | 3.79        | 170.98         | 5.26   |
| UGC02953        | 0.63   | 0.56  | 168.5  | 5.65         | 0.5                 | 6.47           | 0.62  | -0.6                    | -1.32                  | 1.23        | 6.98        | 178.42         | 5.55   |
| UGC02953        | 0.72   | 0.52  | 174.91   | 4.77         | 0.6                 | 7.03           | 0.7   | -0.42                   | -1.14                  | 1.17        | 8.34        | 276.45         | 5.32   |
| <b>UGC03205</b> | <b>0.31</b>  | <b>0.4</b>  | <b>161.26</b>  | <b>10.82</b> | <b>0.1</b>          | <b>2.57</b>    | <b>0.32</b>   | <b>-1.68</b>            | <b>-1.84</b>           | <b>1.66</b> | <b>3.37</b> | <b>37.87</b>   | <b>6.07</b>  |

Table A.2 – continued from previous page

| Galaxy<br>Name  | $\Upsilon_{\text{disk}}$<br>$\left[\frac{M_{\odot}}{L_{\odot}}\right]$ | $\Upsilon_{\text{bulge}}$<br>$\left[\frac{M_{\odot}}{L_{\odot}}\right]$ | $V_{200}$<br>$\left[\frac{\text{km}}{\text{s}}\right]$ | $C_{200}$    | $\alpha_{\epsilon}$ | $\chi_{\nu}^2$ | $\Upsilon_{\text{eff}}$<br>$\left[\frac{M_{\odot}}{L_{\odot}}\right]$ | $\Gamma_{\text{prior}}$ | $\Gamma_{\text{post}}$ | $\gamma$    | $\beta$      | $r_s$<br>[kpc] | $\log \rho_s$<br>$\left[\frac{M_{\odot}}{\text{kpc}^3}\right]$ |
|-----------------|--|---|--|--------------|---------------------|----------------|---|-------------------------|------------------------|-------------|--------------|----------------|--|
| UGC03205        | 0.33   | 0.62  | 140.09   | 10.07        | 0.2                 | 2.77           | 0.37  | -1.38                   | -1.71                  | 1.54        | 4.24         | 52.07          | 5.96   |
| UGC03205        | 0.57   | 0.87  | 161.66   | 4.74         | 0.3                 | 2.77           | 0.62  | -0.92                   | -1.58                  | 1.44        | 4.16         | 107.14         | 5.38   |
| UGC03205        | 0.6  | 0.94  | 154.37   | 4.57         | 0.4                 | 2.88           | 0.65  | -0.7                    | -1.48                  | 1.36        | 5.04         | 144.37         | 5.27   |
| UGC03205        | 0.64   | 0.99  | 147.36   | 4.38         | 0.5                 | 3.03           | 0.69  | -0.52                   | -1.3                   | 1.28        | 6.35         | 192.61         | 5.19   |
| UGC03205        | 0.7  | 0.99  | 149.36   | 4.08         | 0.6                 | 3.24           | 0.74  | -0.38                   | -1.14                  | 1.19        | 7.67         | 275.99         | 5.06   |
| UGC03546        | 0.23   | 0.2   | 149.59   | 12.86        | 0.1                 | 1.3            | 0.22  | -1.71                   | -1.94                  | 1.85        | 2.91         | 35.19          | 5.89   |
| UGC03546        | 0.33   | 0.26  | 132.79   | 9.48         | 0.2                 | 1.16           | 0.31  | -1.37                   | -1.76                  | 1.74        | 3.5          | 52.34          | 5.65   |
| <b>UGC03546</b> | <b>0.37</b>  | <b>0.29</b>   | <b>123.23</b>  | <b>8.14</b>  | <b>0.3</b>          | <b>1.06</b>    | <b>0.35</b>   | <b>-1.08</b>            | <b>-1.66</b>           | <b>1.64</b> | <b>4.18</b>  | <b>69.57</b>   | <b>5.53</b>  |
| UGC03546        | 0.45   | 0.31  | 116.88   | 6.76         | 0.4                 | 1.04           | 0.41  | -0.82                   | -1.94                  | 1.56        | 5.1          | 94.12          | 5.38   |
| UGC03546        | 0.45   | 0.34  | 112.68   | 6.4          | 0.5                 | 1.1            | 0.42  | -0.63                   | -1.58                  | 1.47        | 6.33         | 117.12         | 5.36   |
| UGC03546        | 0.5  | 0.35  | 110.08   | 5.77         | 0.6                 | 1.15           | 0.46  | -0.47                   | -1.45                  | 1.38        | 8.23         | 159.56         | 5.27   |
| UGC03580        | 0.11   | 0.12  | 109.73   | 5.44         | 0.1                 | 7.65           | 0.11  | -1.57                   | -1.6                   | 1.48        | 3.77         | 41.36          | 5.69   |
| UGC03580        | 0.13   | 0.1   | 100.06   | 7.49         | 0.2                 | 3.57           | 0.12  | -1.3                    | -1.44                  | 1.32        | 4.71         | 51.02          | 5.76   |
| UGC03580        | 0.6  | 0.11  | 125.64   | 4.17         | 0.3                 | 3.64           | 0.48  | -0.88                   | -1.13                  | 1.1         | 5.59         | 101.47         | 5.49   |
| UGC03580        | 0.52   | 0.11  | 103.33   | 5.17         | 0.4                 | 2.3            | 0.42  | -0.73                   | -1.07                  | 1.03        | 7.05         | 104.65         | 5.61   |
| UGC03580        | 0.56   | 0.11  | 99.05  | 5.11         | 0.5                 | 2.14           | 0.45  | -0.57                   | -0.99                  | 0.92        | 8.6          | 127.62         | 5.66   |
| <b>UGC03580</b> | <b>0.58</b>  | <b>0.1</b>  | <b>90.05</b>   | <b>5.24</b>  | <b>0.6</b>          | <b>2.15</b>    | <b>0.46</b>   | <b>-0.45</b>            | <b>-0.92</b>           | <b>0.84</b> | <b>10.79</b> | <b>144.0</b>   | <b>5.74</b>  |
| UGC05253        | 0.19   | 0.36  | 190.91   | 9.49         | 0.1                 | 3.15           | 0.25  | -1.66                   | -1.81                  | 1.68        | 3.0          | 41.32          | 6.05   |
| UGC05253        | 0.12   | 0.4   | 161.61   | 11.47        | 0.2                 | 3.18           | 0.23  | -1.42                   | -1.7                   | 1.58        | 3.8          | 52.39          | 6.01   |
| UGC05253        | 0.13   | 0.48  | 148.07   | 9.99         | 0.3                 | 3.18           | 0.26  | -1.15                   | -1.62                  | 1.47        | 4.65         | 68.51          | 5.94   |
| UGC05253        | 0.25   | 0.51  | 142.09   | 8.12         | 0.4                 | 2.75           | 0.35  | -0.88                   | -1.67                  | 1.36        | 5.78         | 94.93          | 5.82   |
| UGC05253        | 0.12   | 0.51  | 127.53   | 9.42         | 0.5                 | 1.94           | 0.27  | -0.77                   | -1.44                  | 1.22        | 7.54         | 91.42          | 6.13   |
| <b>UGC05253</b> | <b>0.16</b>  | <b>0.55</b>   | <b>121.42</b>  | <b>8.53</b>  | <b>0.6</b>          | <b>1.28</b>    | <b>0.31</b>   | <b>-0.6</b>             | <b>-1.42</b>           | <b>1.11</b> | <b>10.11</b> | <b>119.51</b>  | <b>6.12</b>  |
| UGC06614        | 0.42   | 0.12  | 163.88   | 6.49         | 0.1                 | 2.21           | 0.26  | -1.59                   | -1.64                  | 1.51        | 3.23         | 44.08          | 5.94   |
| UGC06614        | 0.25   | 0.2   | 164.8  | 6.34         | 0.2                 | 1.11           | 0.22  | -1.26                   | -1.64                  | 1.33        | 3.92         | 68.64          | 5.81   |
| UGC06614        | 0.23   | 0.23  | 150.95   | 6.56         | 0.3                 | 0.92           | 0.23  | -1.01                   | -1.47                  | 1.22        | 4.86         | 88.99          | 5.78   |
| UGC06614        | 0.2  | 0.27  | 146.43   | 6.16         | 0.4                 | 0.63           | 0.24  | -0.79                   | -1.36                  | 1.1         | 6.07         | 117.92         | 5.76   |
| UGC06614        | 0.13   | 0.31  | 141.73   | 5.88         | 0.5                 | 0.4            | 0.23  | -0.61                   | -1.25                  | 1.01        | 7.67         | 152.86         | 5.75   |
| <b>UGC06614</b> | <b>0.11</b>  | <b>0.32</b>   | <b>134.64</b>  | <b>5.92</b>  | <b>0.6</b>          | <b>0.36</b>    | <b>0.22</b>   | <b>-0.48</b>            | <b>-1.13</b>           | <b>0.87</b> | <b>10.32</b> | <b>188.27</b>  | <b>5.87</b>  |
| UGC06786        | 0.12   | 0.16  | 180.19   | 18.15        | 0.1                 | 0.55           | 0.13  | -1.77                   | -1.85                  | 1.64        | 3.28         | 33.34          | 6.3  |
| <b>UGC06786</b> | <b>0.2</b>   | <b>0.36</b>   | <b>153.86</b>  | <b>14.37</b> | <b>0.2</b>          | <b>0.51</b>    | <b>0.24</b>   | <b>-1.49</b>            | <b>-1.71</b>           | <b>1.5</b>  | <b>4.05</b>  | <b>45.42</b>   | <b>6.21</b>  |
| UGC06786        | 0.31   | 0.51  | 141.61   | 11.2         | 0.3                 | 0.71           | 0.36  | -1.19                   | -1.56                  | 1.39        | 4.87         | 61.43          | 6.09   |
| UGC06786        | 0.45   | 0.49  | 131.39   | 9.83         | 0.4                 | 0.83           | 0.46  | -0.95                   | -1.42                  | 1.27        | 6.08         | 75.98          | 6.09   |
| UGC06786        | 0.5  | 0.61  | 127.35   | 8.59         | 0.5                 | 0.94           | 0.53  | -0.73                   | -1.34                  | 1.18        | 7.48         | 99.68          | 6.02   |
| UGC06786        | 0.51   | 0.65  | 118.32   | 8.42         | 0.6                 | 1.03           | 0.55  | -0.59                   | -1.26                  | 1.09        | 9.86         | 117.91         | 6.1  |
| UGC06787        | 0.52   | 0.24  | 192.02   | 10.42        | 0.1                 | 26.27          | 0.38  | -1.67                   | -1.83                  | 1.68        | 3.07         | 40.3           | 6.08   |
| UGC06787        | 0.87   | 0.34  | 187.04   | 7.0          | 0.2                 | 24.64          | 0.61  | -1.29                   | -1.73                  | 1.59        | 3.3          | 69.38          | 5.69   |
| UGC06787        | 1.0  | 0.36  | 182.56   | 6.46         | 0.3                 | 23.8           | 0.69  | -1.01                   | -1.9                   | 1.49        | 3.74         | 98.61          | 5.54   |
| <b>UGC06787</b> | <b>0.99</b>  | <b>0.49</b>   | <b>254.97</b>  | <b>4.6</b>   | <b>0.4</b>          | <b>19.43</b>   | <b>0.75</b>   | <b>-0.7</b>             | <b>-1.36</b>           | <b>1.52</b> | <b>0.91</b>  | <b>179.72</b>  | <b>4.95</b>  |
| UGC06787        | 1.0  | 0.51  | 209.15   | 5.11         | 0.5                 | 20.17          | 0.76  | -0.57                   | -1.24                  | 1.41        | 2.7          | 215.43         | 5.03   |
| UGC06787        | 1.0  | 0.55  | 187.04   | 5.29         | 0.6                 | 21.61          | 0.78  | -0.45                   | -1.14                  | 1.32        | 4.64         | 269.61         | 5.06   |
| UGC06973        | 0.11   | 0.11  | 128.01   | 15.55        | 0.1                 | 2.34           | 0.11  | -1.74                   | -1.96                  | 1.91        | 2.5          | 31.41          | 5.77   |

Table A.2 – continued from previous page

| Galaxy<br>Name  | $\Upsilon_{\text{disk}}$<br>$\left[\frac{M_{\odot}}{L_{\odot}}\right]$ | $\Upsilon_{\text{bulge}}$<br>$\left[\frac{M_{\odot}}{L_{\odot}}\right]$ | $V_{200}$<br>$\left[\frac{\text{km}}{\text{s}}\right]$ | $C_{200}$    | $\alpha_{\epsilon}$ | $\chi_{\nu}^2$ | $\Upsilon_{\text{eff}}$<br>$\left[\frac{M_{\odot}}{L_{\odot}}\right]$ | $\Gamma_{\text{prior}}$ | $\Gamma_{\text{post}}$ | $\gamma$    | $\beta$     | $r_s$<br>[kpc] | $\log \rho_s$<br>$\left[\frac{M_{\odot}}{\text{kpc}^3}\right]$ |
|-----------------|--|---|--|--------------|---------------------|----------------|---|-------------------------|------------------------|-------------|-------------|----------------|--|
| UGC06973        | 0.12   | 0.11  | 112.39   | 15.17        | 0.2                 | 0.92           | 0.12  | -1.5                    | -1.82                  | 1.72        | 3.34        | 36.7           | 5.9  |
| UGC06973        | 0.13   | 0.13  | 101.39   | 14.16        | 0.3                 | 0.48           | 0.13  | -1.27                   | -1.71                  | 1.55        | 4.11        | 39.02          | 6.08   |
| UGC06973        | 0.12   | 0.27  | 97.21  | 12.8         | 0.4                 | 0.37           | 0.14  | -1.05                   | -1.59                  | 1.39        | 4.84        | 44.73          | 6.18   |
| <b>UGC06973</b> | <b>0.14</b>  | <b>0.26</b>   | <b>95.5</b>  | <b>11.77</b> | <b>0.5</b>          | <b>0.34</b>    | <b>0.16</b>   | <b>-0.86</b>            | <b>-1.47</b>           | <b>1.27</b> | <b>5.7</b>  | <b>55.1</b>    | <b>6.21</b>  |
| UGC06973        | 0.14   | 0.37  | 98.38  | 10.76        | 0.6                 | 0.52           | 0.17  | -0.69                   | -1.35                  | 1.16        | 6.59        | 76.79          | 6.14   |
| UGC08699        | 0.27   | 0.41  | 136.64   | 10.57        | 0.1                 | 1.19           | 0.31  | -1.67                   | -1.89                  | 1.78        | 3.15        | 36.26          | 5.83   |
| UGC08699        | 0.31   | 0.5   | 125.28   | 9.43         | 0.2                 | 0.96           | 0.37  | -1.37                   | -1.76                  | 1.66        | 3.79        | 50.88          | 5.7  |
| UGC08699        | 0.34   | 0.55  | 114.91   | 8.88         | 0.3                 | 0.94           | 0.4   | -1.11                   | -1.7                   | 1.54        | 4.59        | 62.43          | 5.69   |
| UGC08699        | 0.68   | 0.53  | 127.9  | 5.34         | 0.4                 | 0.73           | 0.64  | -0.74                   | -1.65                  | 1.49        | 4.57        | 118.49         | 5.17   |
| UGC08699        | 0.72   | 0.59  | 155.83   | 4.49         | 0.5                 | 0.59           | 0.68  | -0.53                   | -1.46                  | 1.45        | 2.91        | 196.17         | 4.81   |
| <b>UGC08699</b> | <b>0.82</b>  | <b>0.59</b>   | <b>147.34</b>  | <b>4.48</b>  | <b>0.6</b>          | <b>0.58</b>    | <b>0.75</b>   | <b>-0.41</b>            | <b>-1.16</b>           | <b>1.35</b> | <b>3.94</b> | <b>256.15</b>  | <b>4.78</b>  |
| UGC09133        | 0.56   | 0.33  | 217.02   | 3.38         | 0.1                 | 7.26           | 0.49  | -1.49                   | -1.91                  | 1.71        | 2.69        | 55.23          | 5.69   |
| UGC09133        | 0.64   | 0.39  | 223.43   | 2.87         | 0.2                 | 7.31           | 0.57  | -1.1                    | -1.72                  | 1.66        | 2.81        | 95.06          | 5.25   |
| UGC09133        | 0.64   | 0.42  | 203.65   | 3.34         | 0.3                 | 6.93           | 0.58  | -0.83                   | -1.56                  | 1.6         | 3.34        | 133.09         | 5.07   |
| <b>UGC09133</b> | <b>0.72</b>  | <b>0.46</b>   | <b>216.15</b>  | <b>2.79</b>  | <b>0.4</b>          | <b>6.8</b>     | <b>0.65</b>   | <b>-0.57</b>            | <b>-1.43</b>           | <b>1.58</b> | <b>3.51</b> | <b>201.37</b>  | <b>4.75</b>  |
| UGC09133        | 0.78   | 0.48  | 218.14   | 2.57         | 0.5                 | 7.25           | 0.69  | -0.4                    | -1.39                  | 1.51        | 4.29        | 289.34         | 4.56   |
| UGC09133        | 0.67   | 0.52  | 174.38   | 3.15         | 0.6                 | 7.07           | 0.63  | -0.33                   | -1.2                   | 1.39        | 7.16        | 348.73         | 4.69   |
| UGC11914        | 0.12   | 0.47  | 222.9  | 14.64        | 0.1                 | 1.51           | 0.21  | -1.73                   | -1.93                  | 1.68        | 3.83        | 38.11          | 6.34   |
| UGC11914        | 0.1  | 0.62  | 203.71   | 13.73        | 0.2                 | 1.1            | 0.23  | -1.47                   | -1.8                   | 1.54        | 4.31        | 53.72          | 6.24   |
| UGC11914        | 0.1  | 0.75  | 198.97   | 12.14        | 0.3                 | 0.92           | 0.26  | -1.22                   | -1.6                   | 1.41        | 4.66        | 73.1           | 6.18   |
| UGC11914        | 0.21   | 0.85  | 257.56   | 9.16         | 0.4                 | 0.75           | 0.37  | -0.92                   | -1.22                  | 1.34        | 0.73        | 130.72         | 5.77   |
| UGC11914        | 0.31   | 0.88  | 252.31   | 8.51         | 0.5                 | 0.74           | 0.45  | -0.73                   | -1.22                  | 1.24        | 0.63        | 177.55         | 5.69   |
| <b>UGC11914</b> | <b>0.32</b>  | <b>0.91</b>   | <b>256.34</b>  | <b>8.73</b>  | <b>0.6</b>          | <b>0.72</b>    | <b>0.47</b>   | <b>-0.61</b>            | <b>-1.11</b>           | <b>1.13</b> | <b>-0.8</b> | <b>234.73</b>  | <b>5.71</b>  |

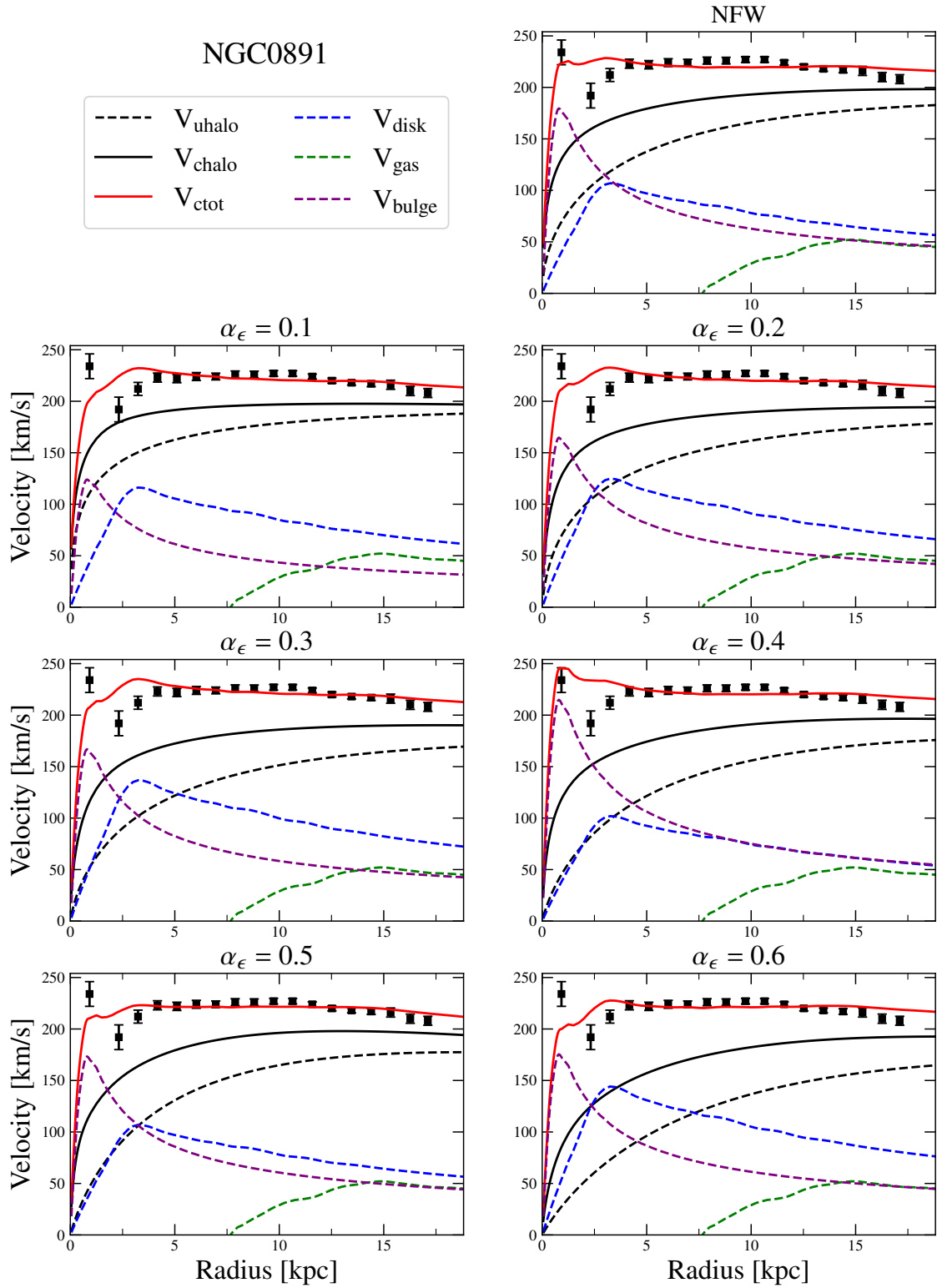


Figure A.1: Same as Figure 3.1, but for galaxy NGC 0891.

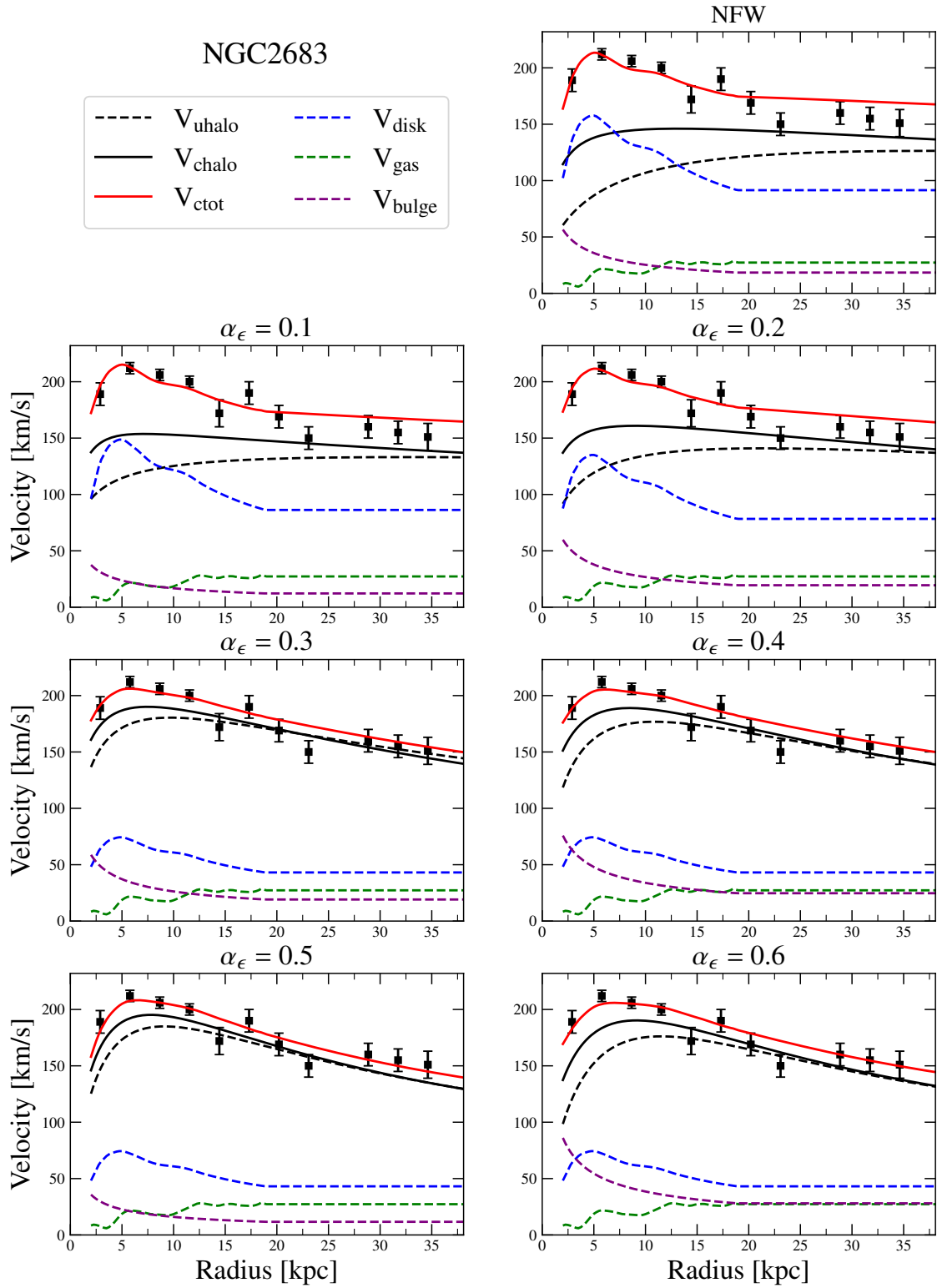


Figure A.2: Same as Figure 3.1, but for galaxy NGC 2683.

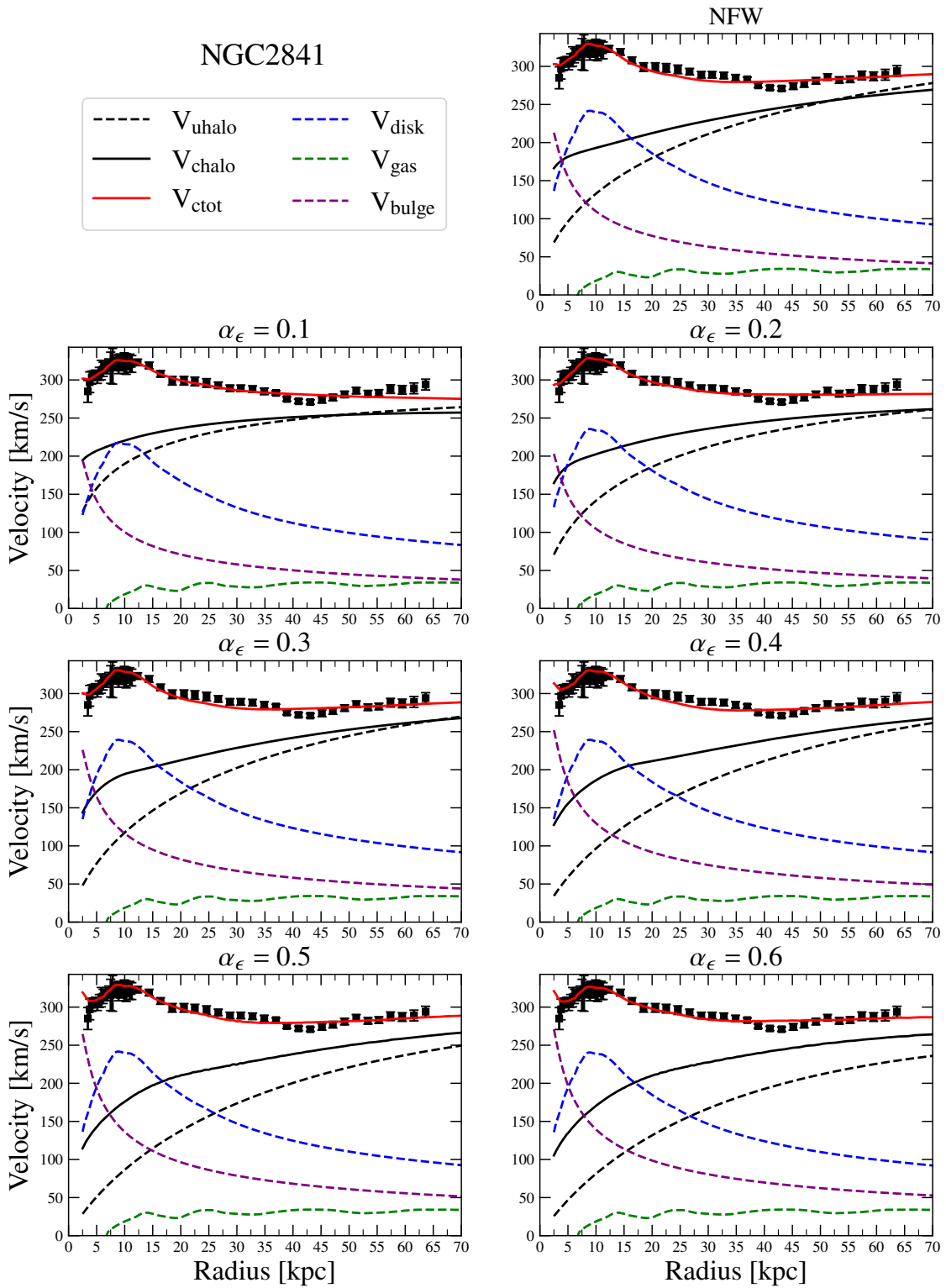


Figure A.3: Same as Figure 3.1, but for galaxy NGC 2841.

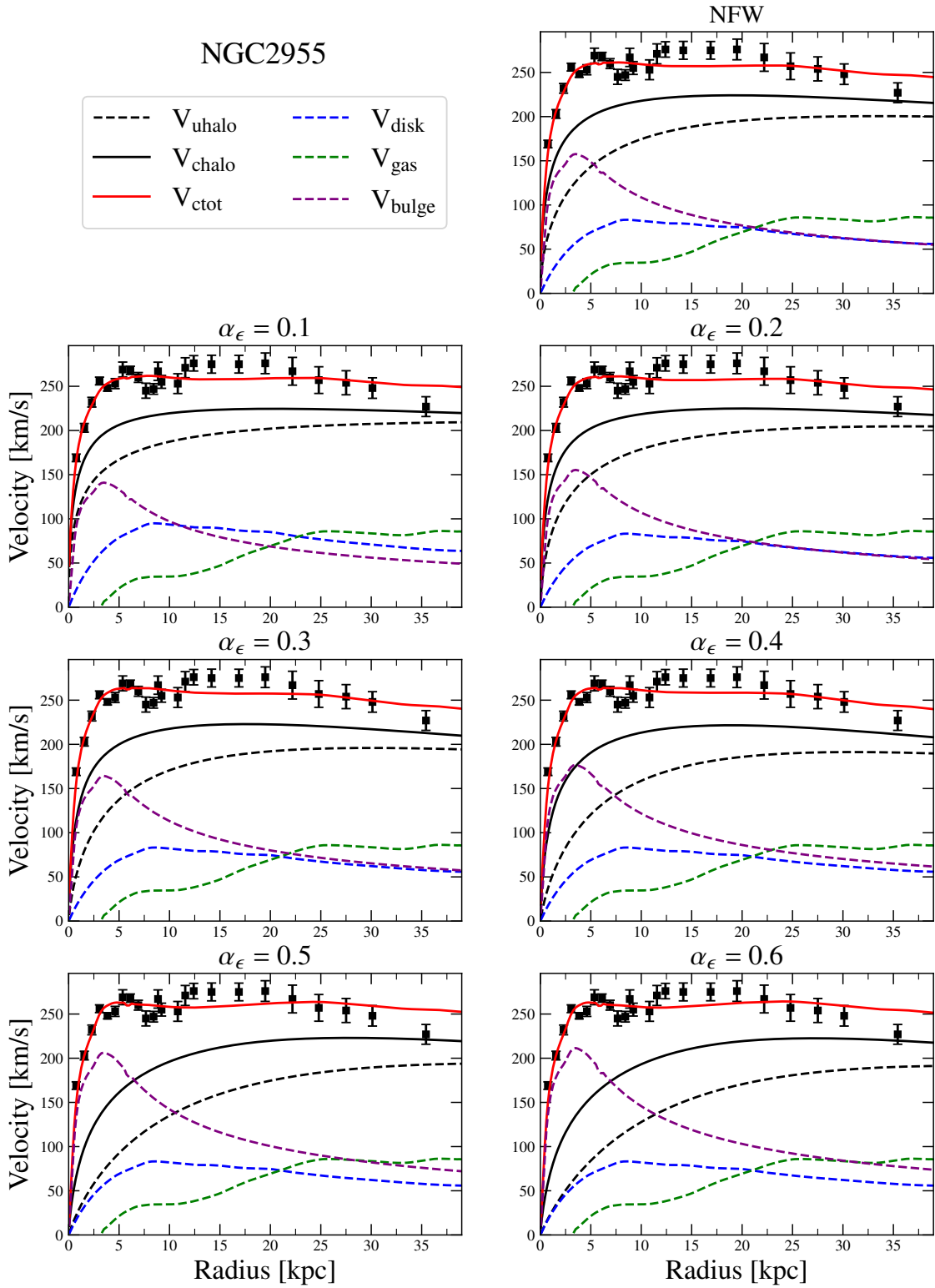


Figure A.4: Same as Figure 3.1, but for galaxy NGC 2955.

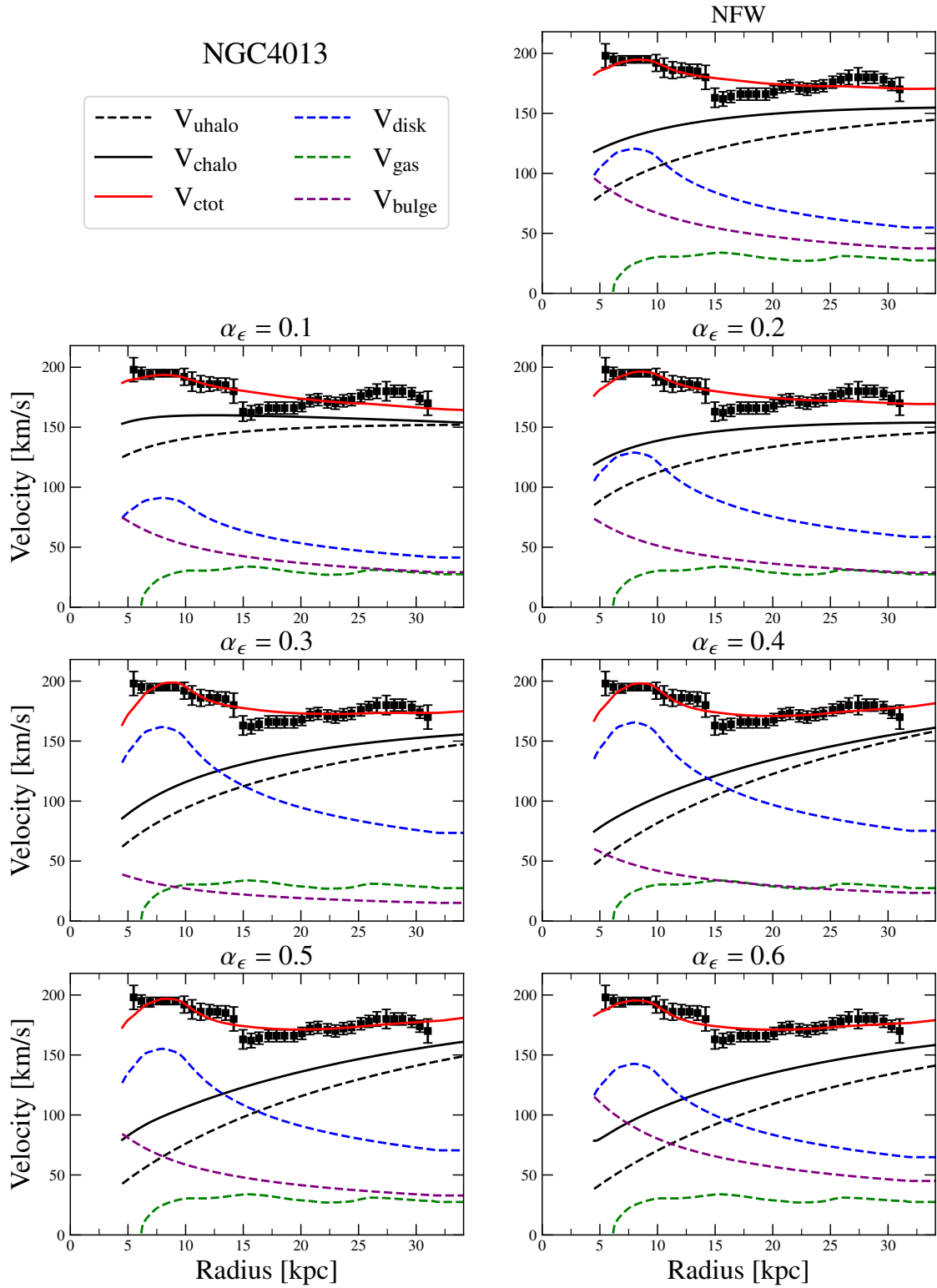


Figure A.5: Same as Figure 3.1, but for galaxy NGC 4013.

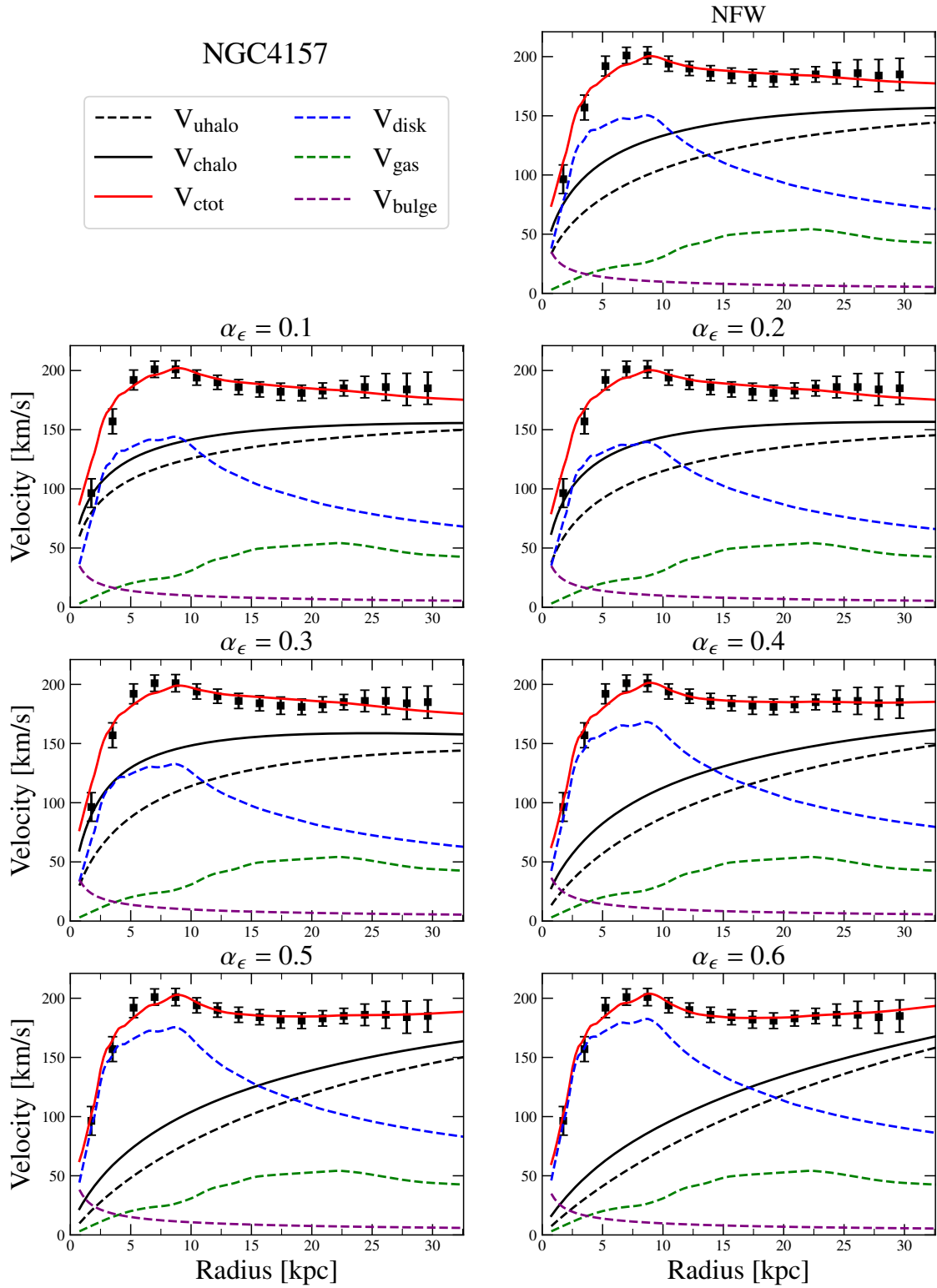


Figure A.6: Same as Figure 3.1, but for galaxy NGC 4157.

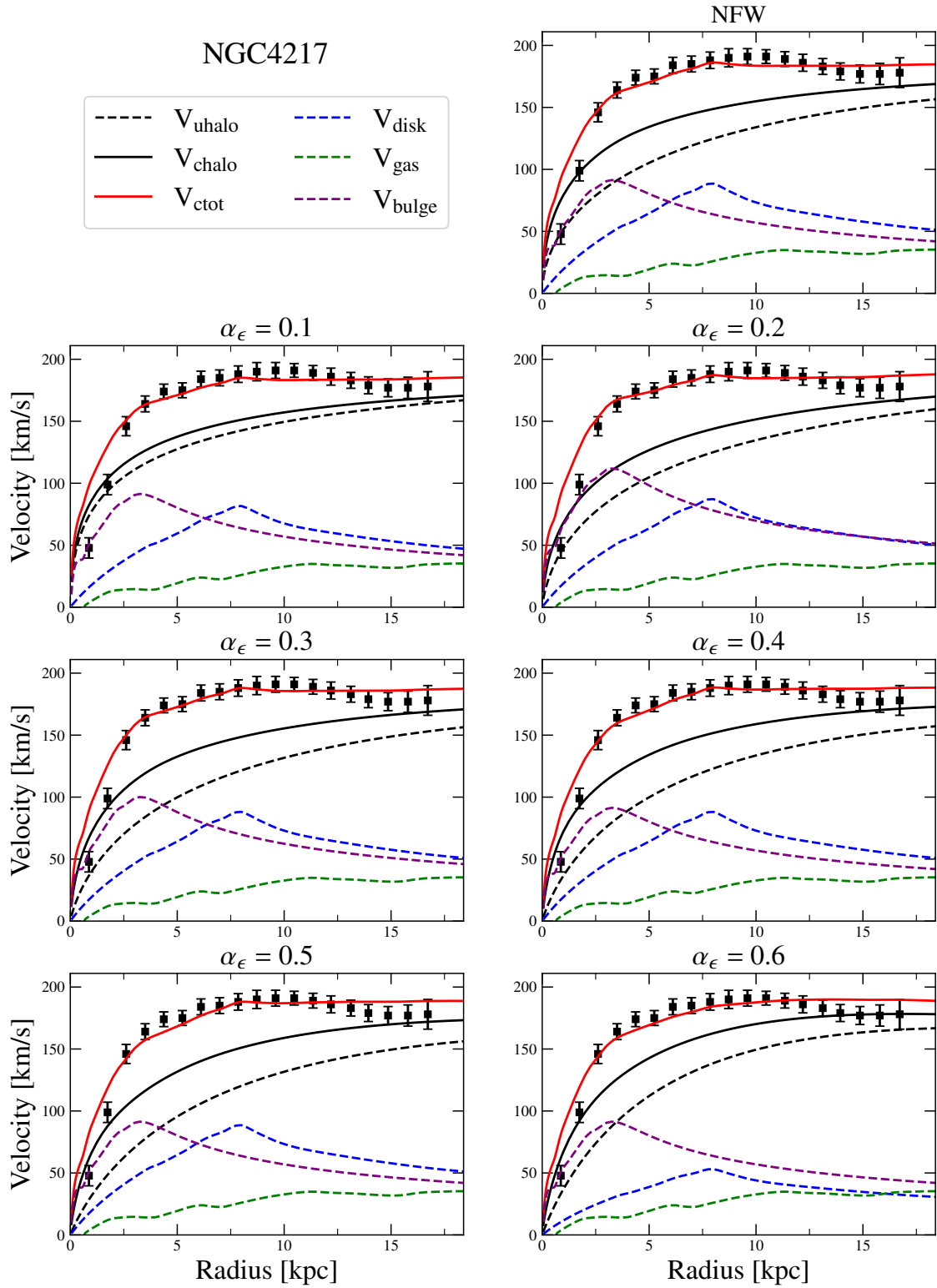


Figure A.7: Same as Figure 3.1, but for galaxy NGC 4217.

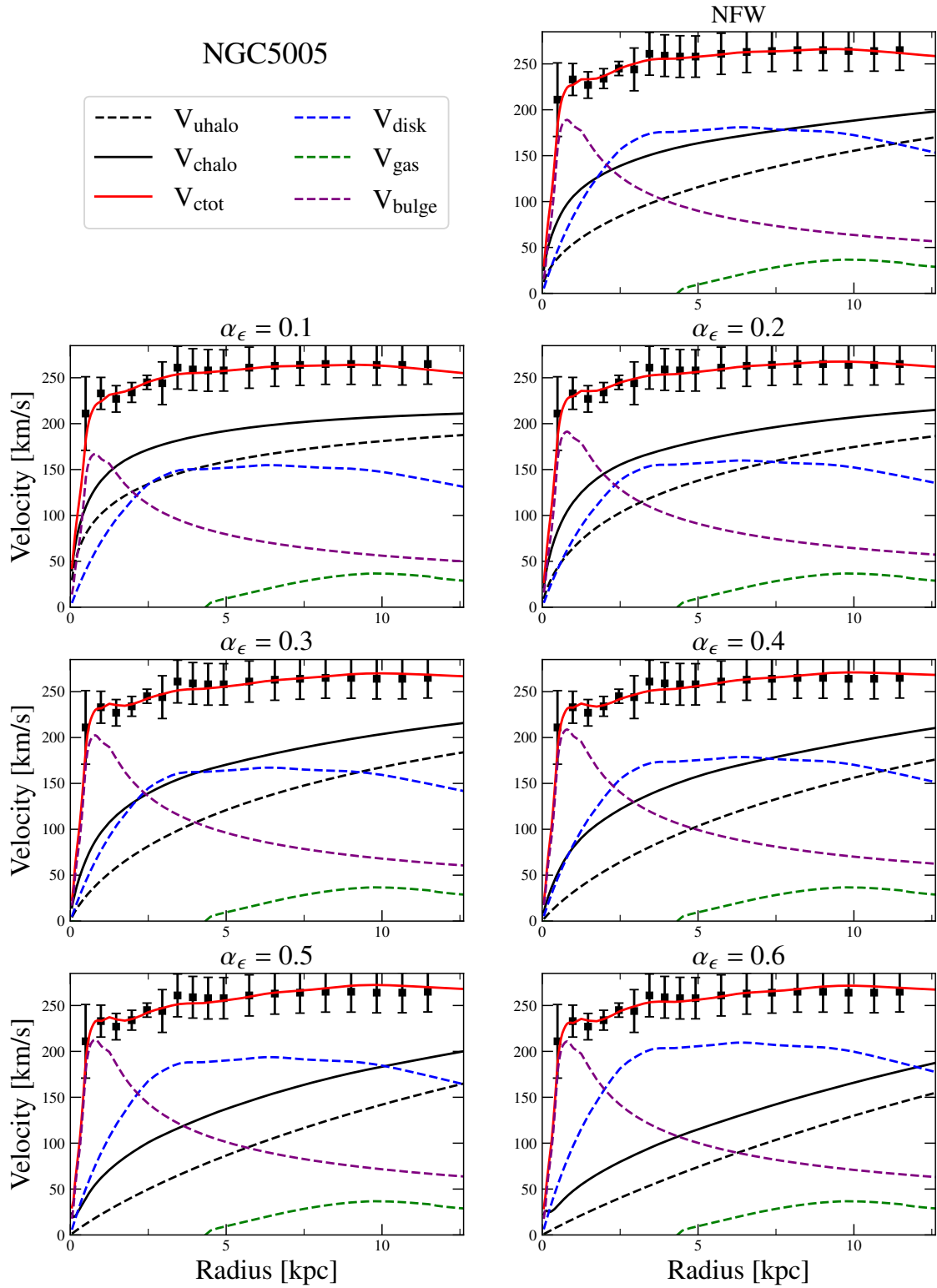


Figure A.8: Same as Figure 3.1, but for galaxy NGC 5005.

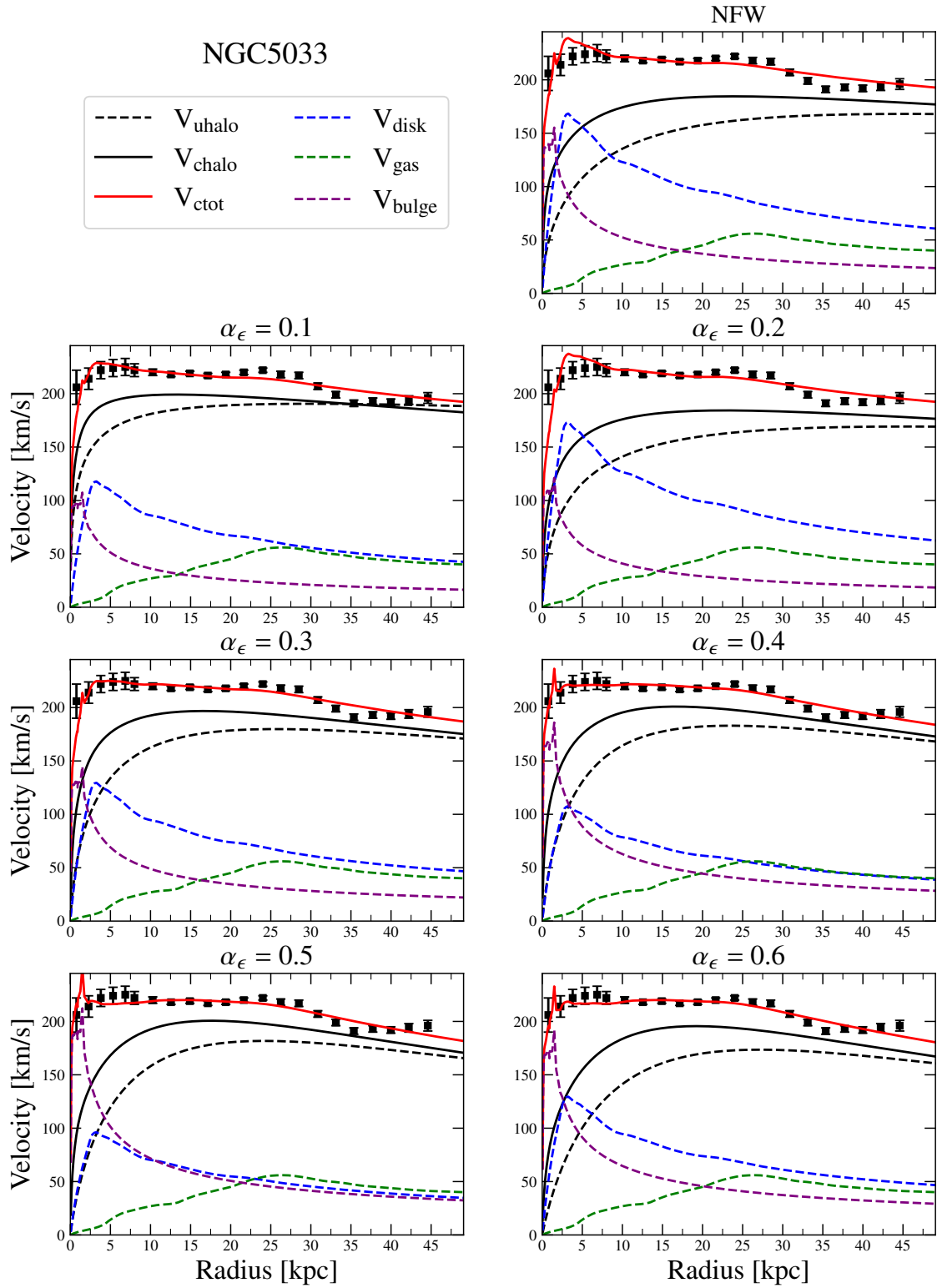


Figure A.9: Same as Figure 3.1, but for galaxy NGC 5033.

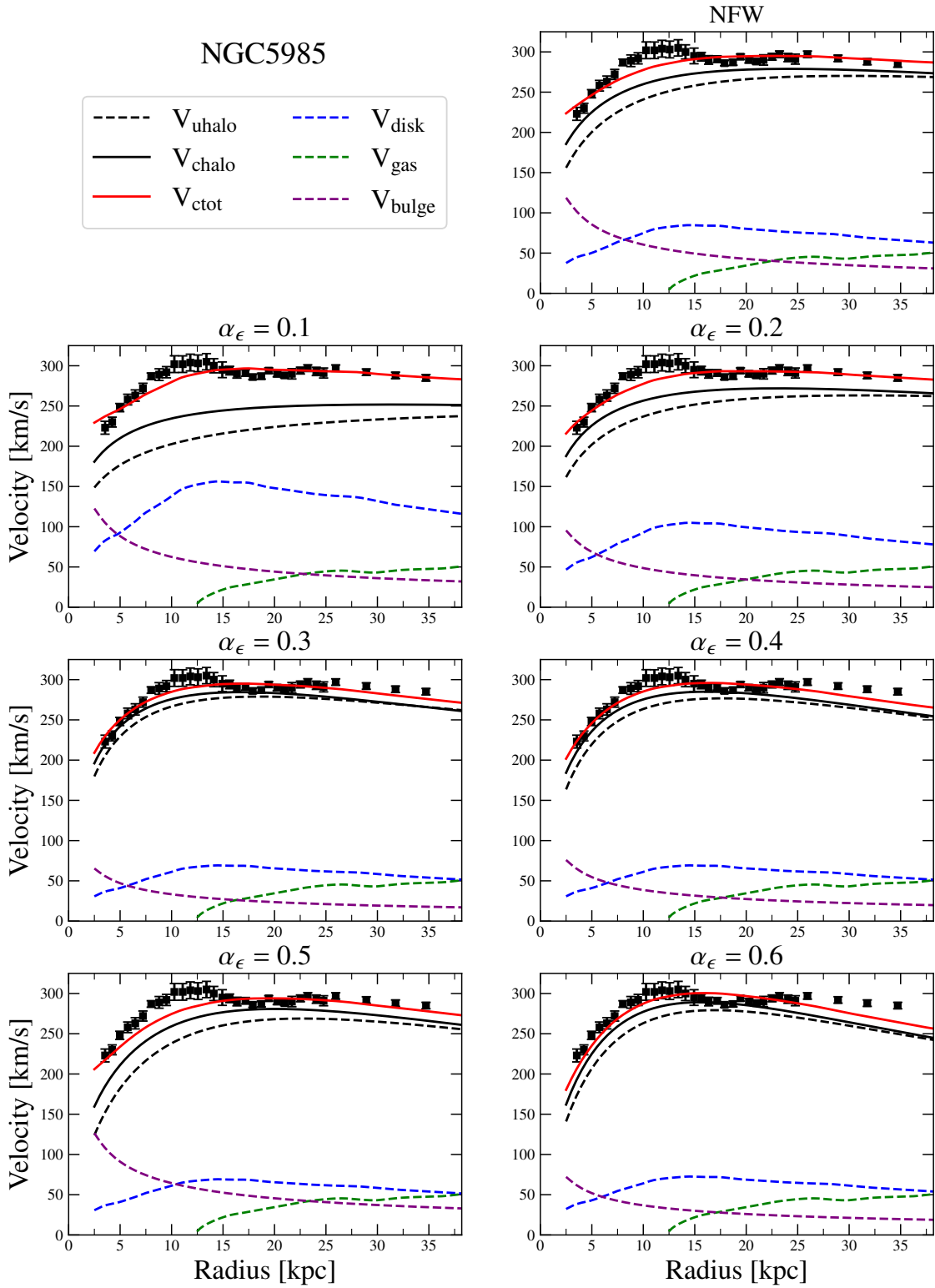


Figure A.10: Same as Figure 3.1, but for galaxy NGC 5985.

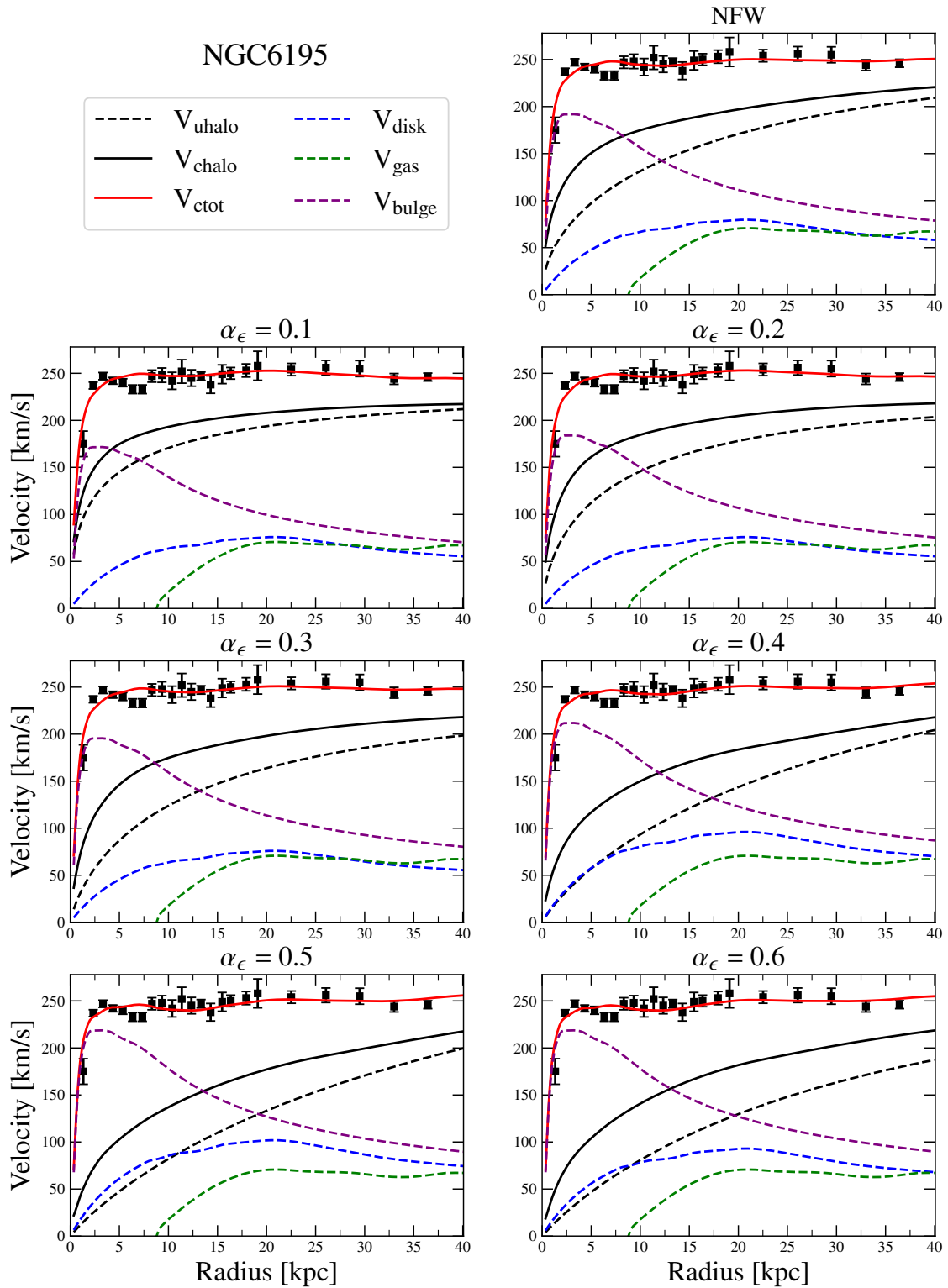


Figure A.11: Same as Figure 3.1, but for galaxy NGC 6195.

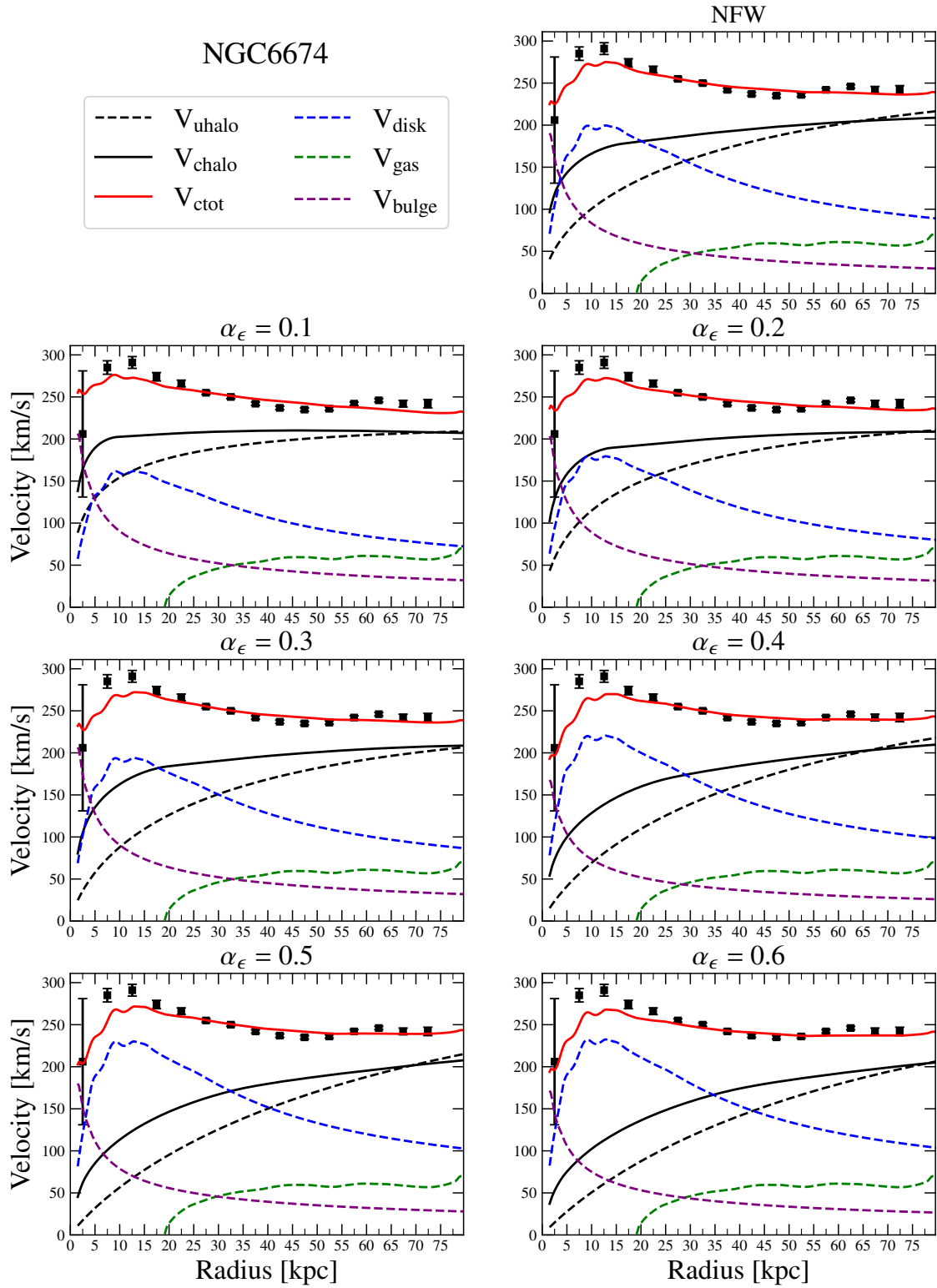


Figure A.12: Same as Figure 3.1, but for galaxy NGC 6674.

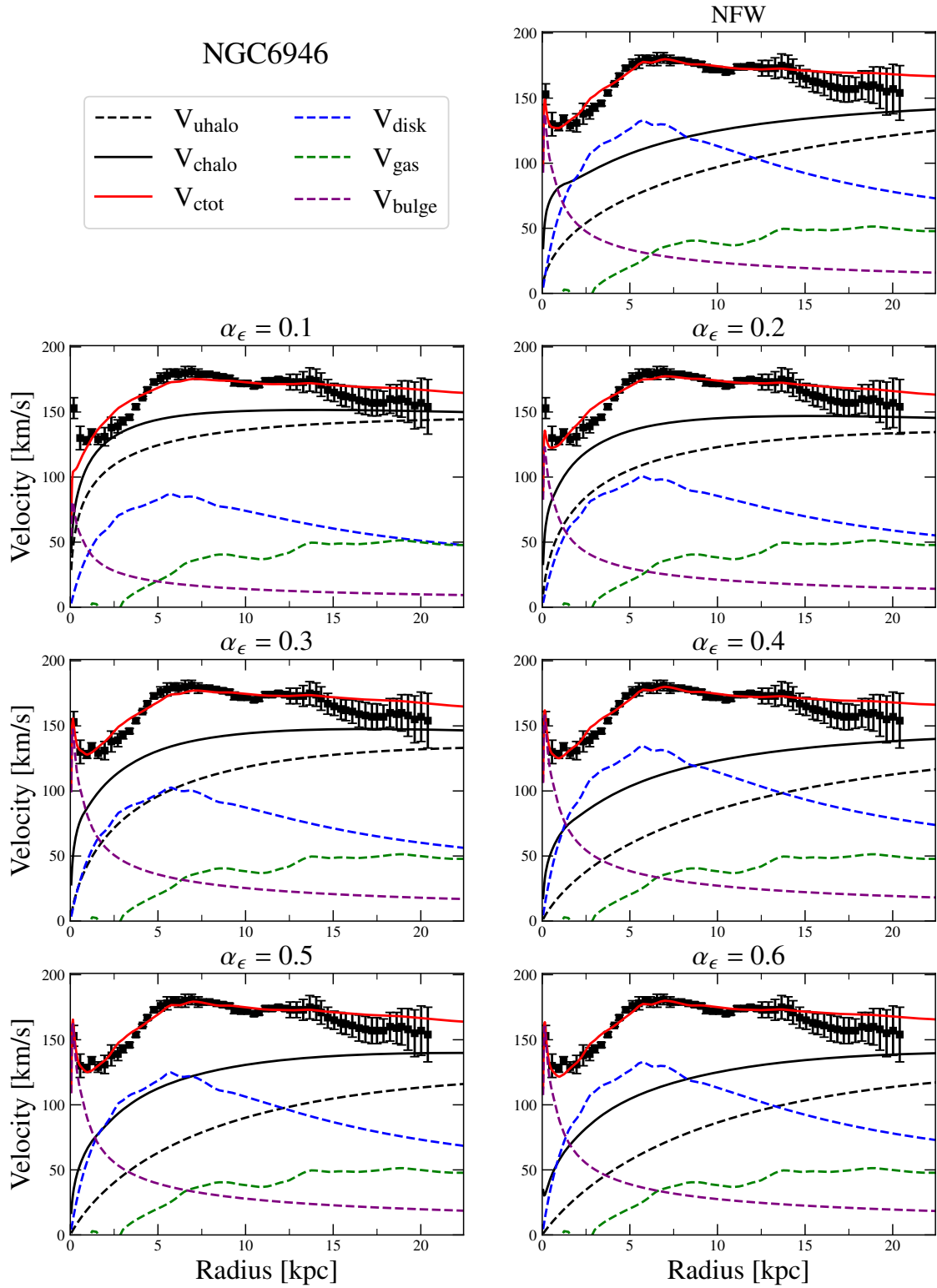


Figure A.13: Same as Figure 3.1, but for galaxy NGC 6946.

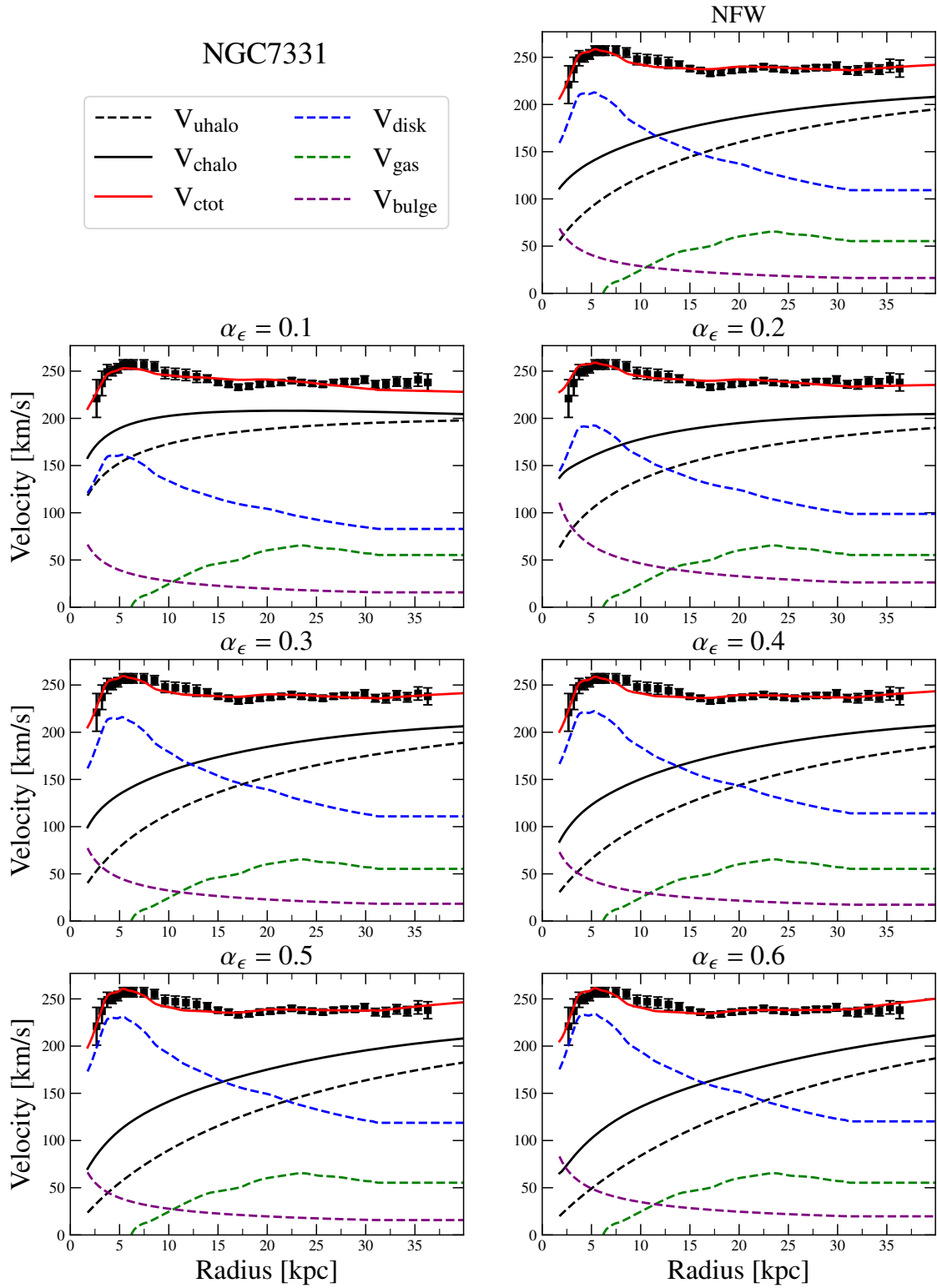


Figure A.14: Same as Figure 3.1, but for galaxy NGC 7331.

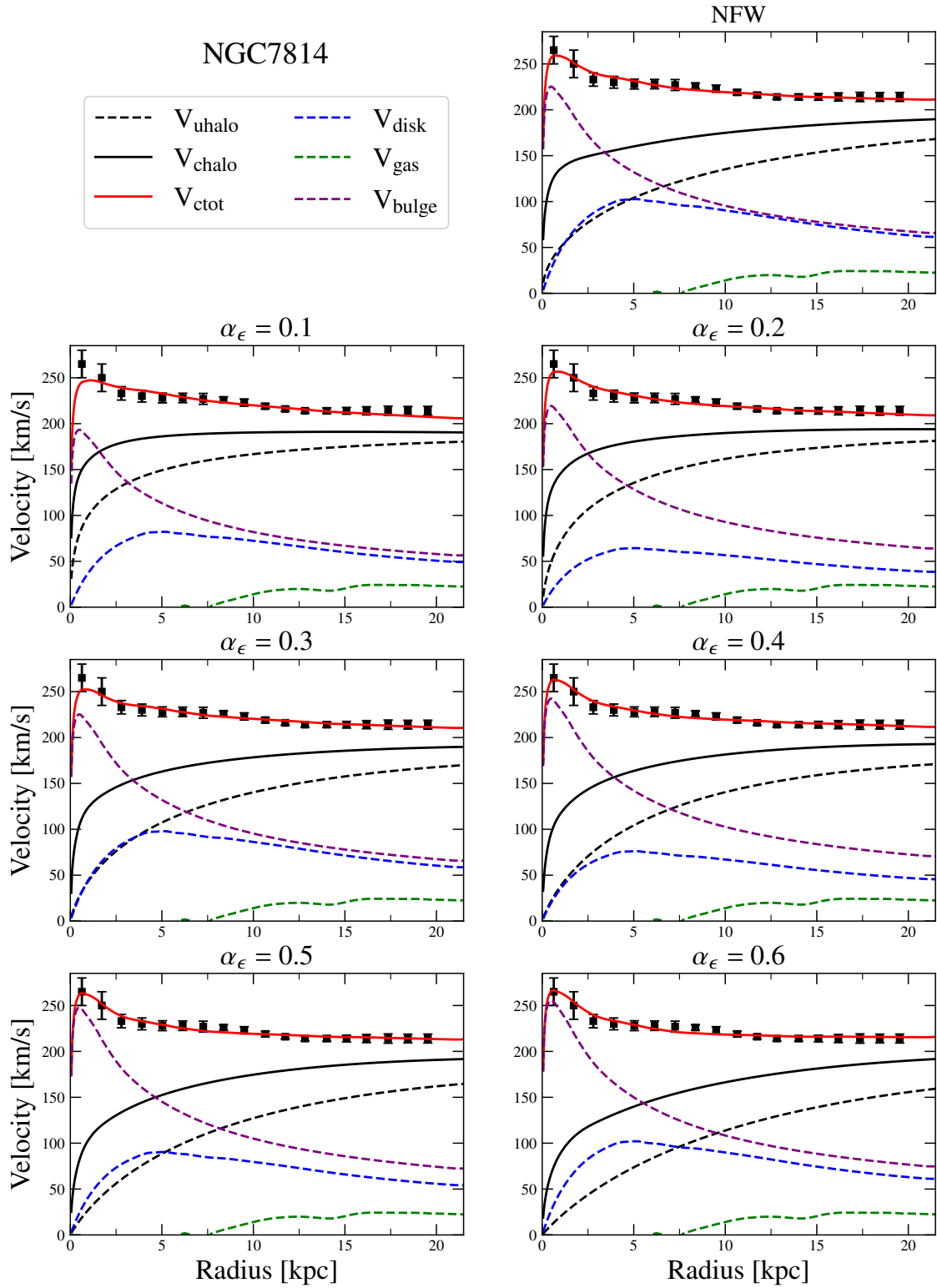


Figure A.15: Same as Figure 3.1, but for galaxy NGC 7814.

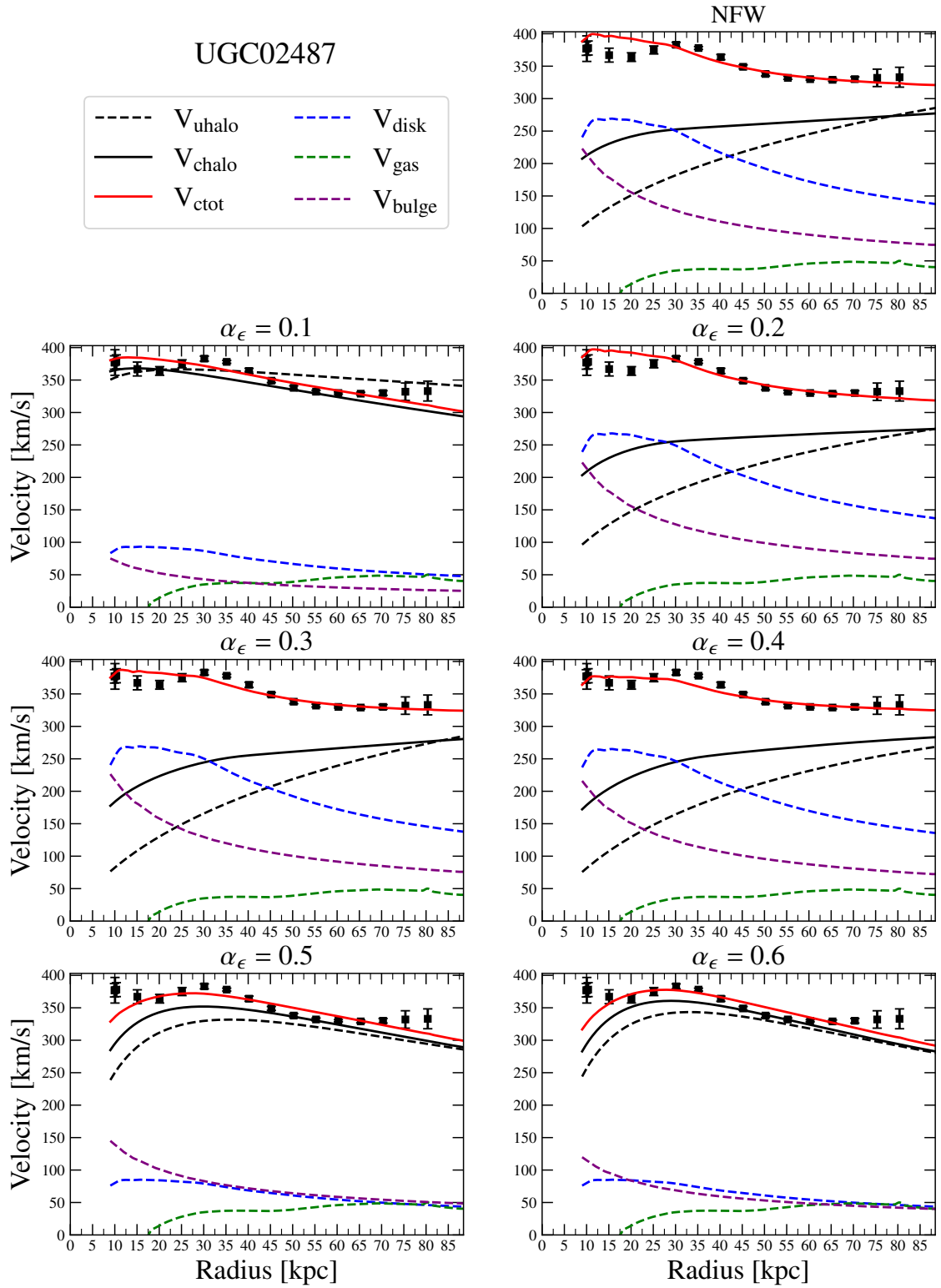


Figure A.16: Same as Figure 3.1, but for galaxy UGC 02487.

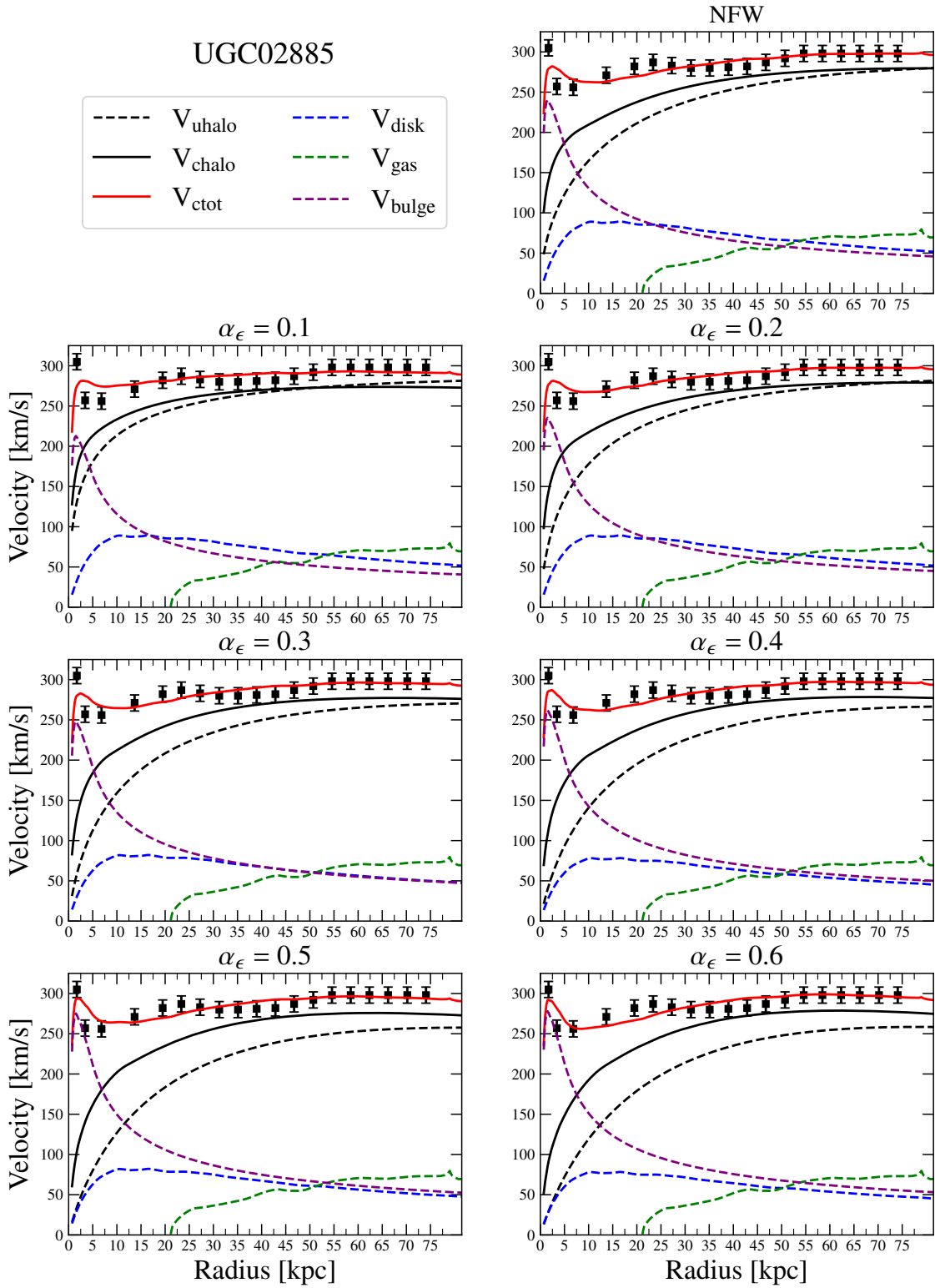


Figure A.17: Same as Figure 3.1, but for galaxy UGC 02885.

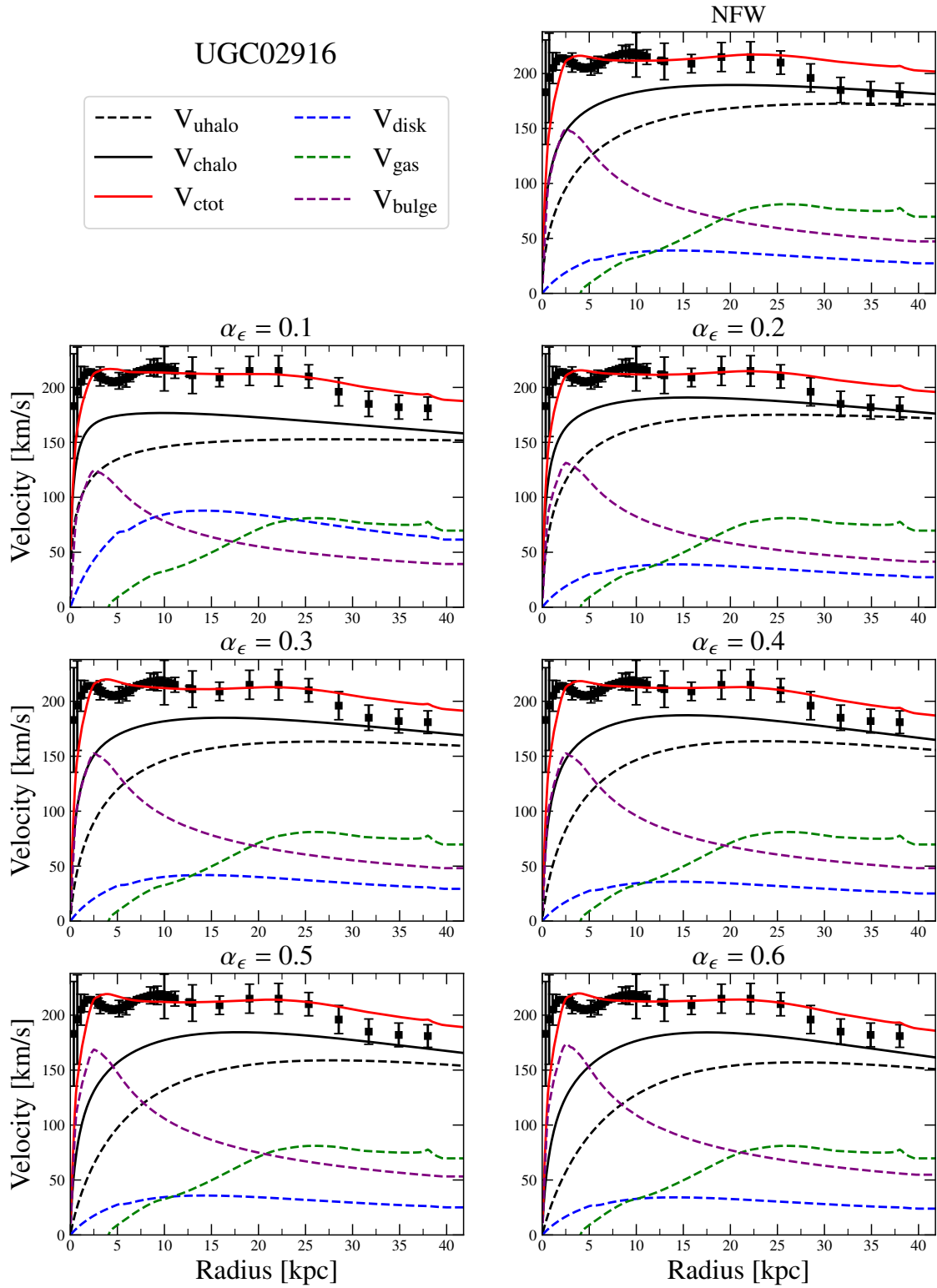


Figure A.18: Same as Figure 3.1, but for galaxy UGC 02916.

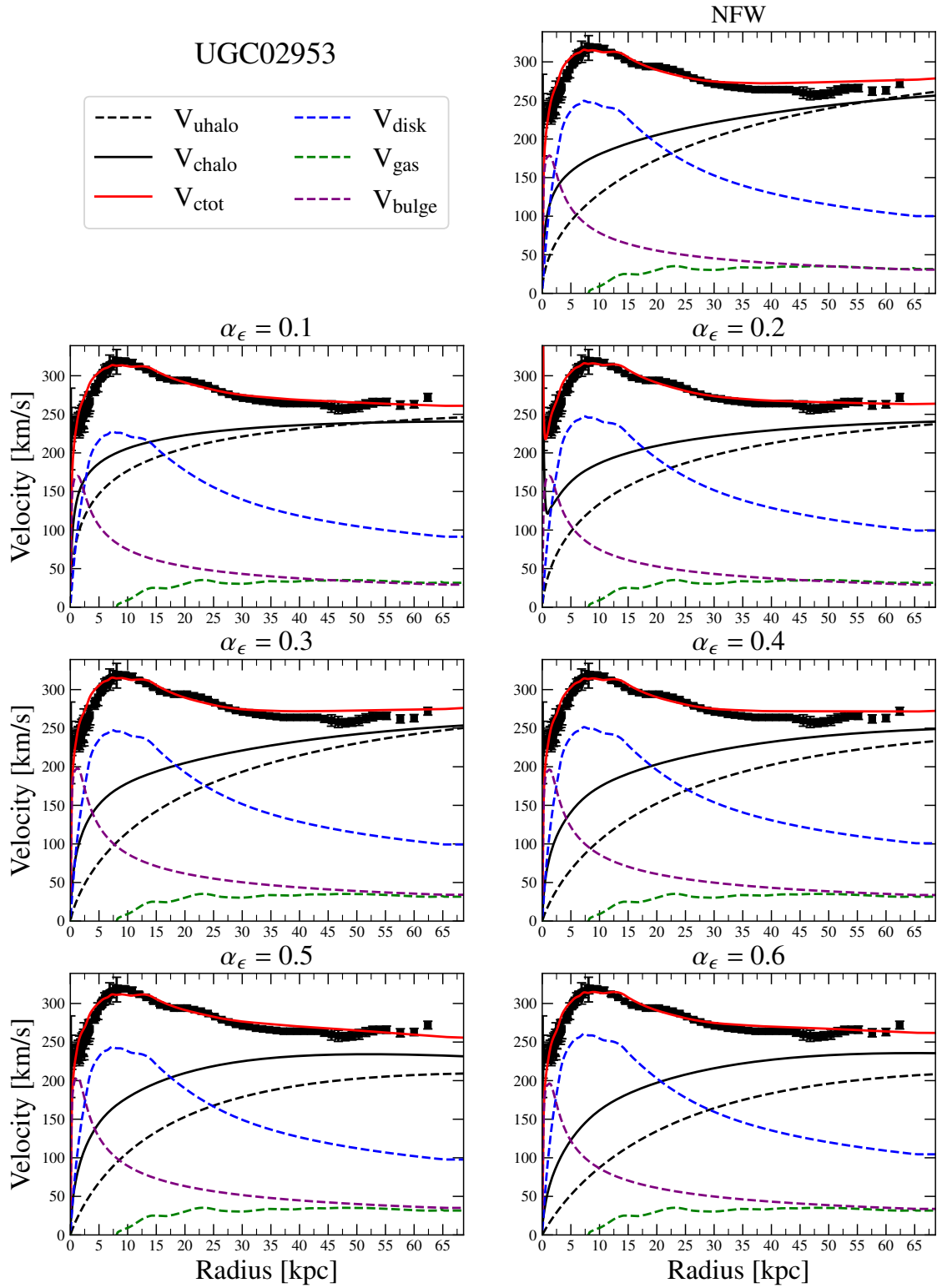


Figure A.19: Same as Figure 3.1, but for galaxy UGC 02953.

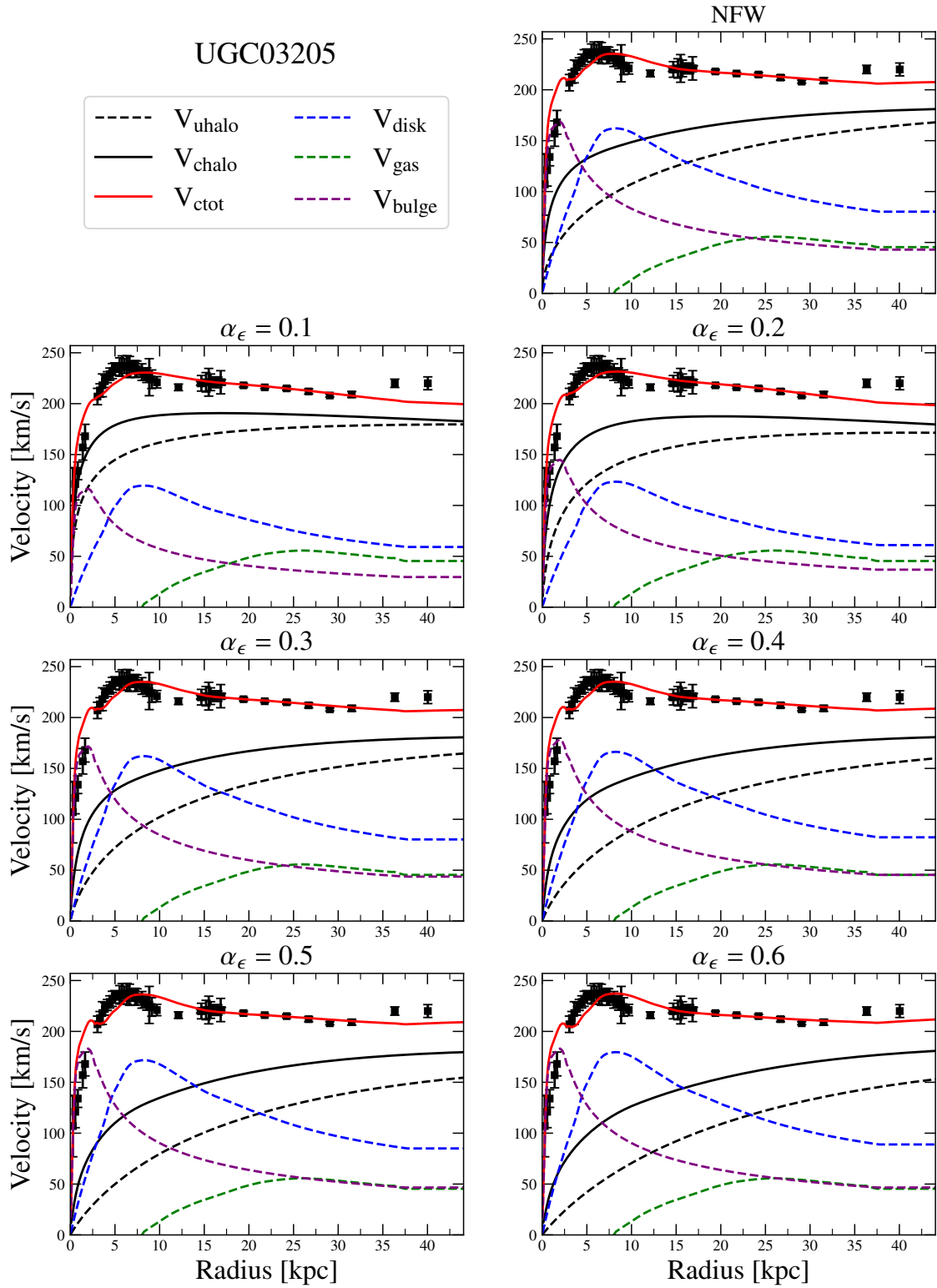


Figure A.20: Same as Figure 3.1, but for galaxy UGC 03205.

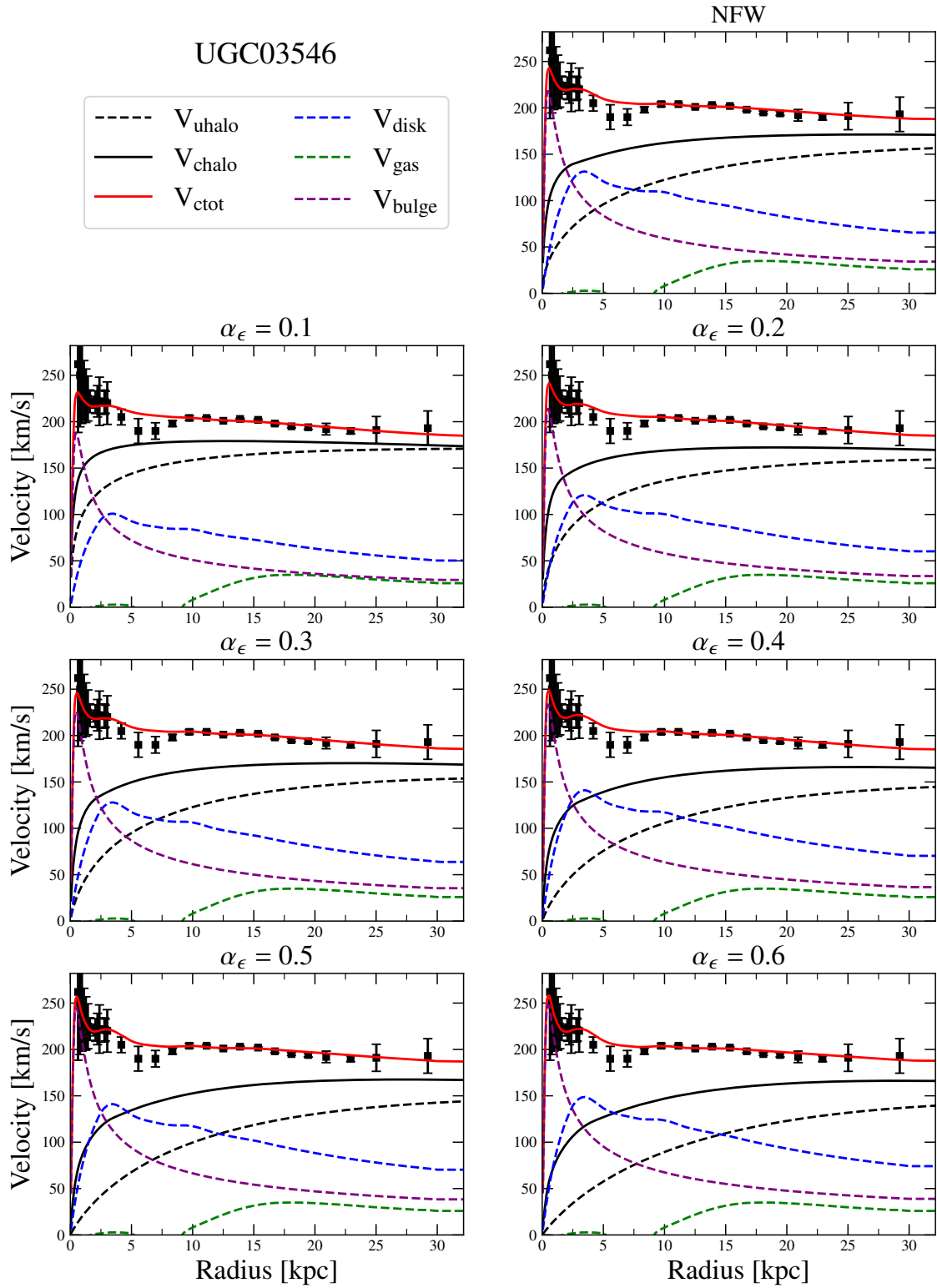


Figure A.21: Same as Figure 3.1, but for galaxy UGC 03546.

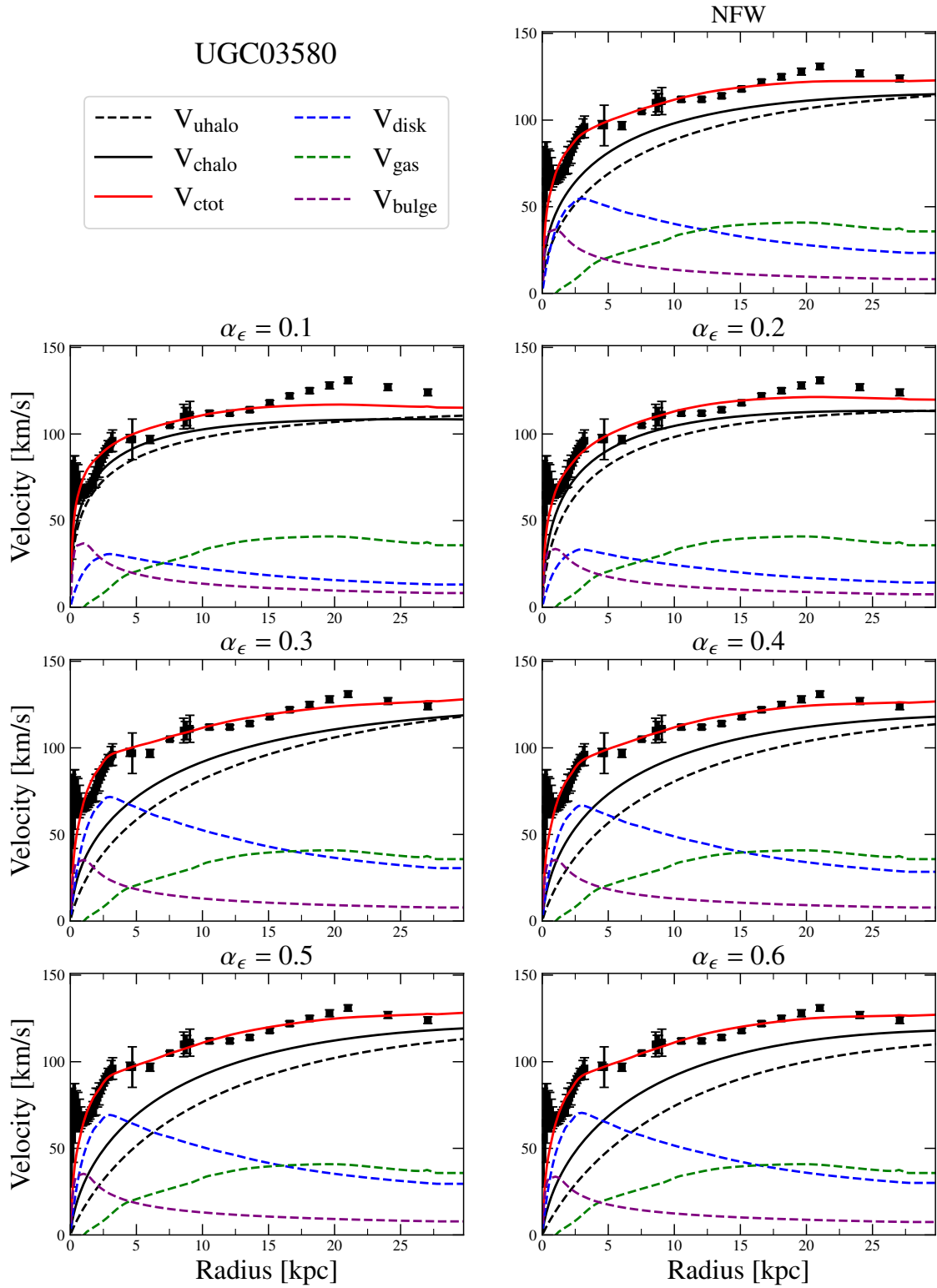


Figure A.22: Same as Figure 3.1, but for galaxy UGC 03580.

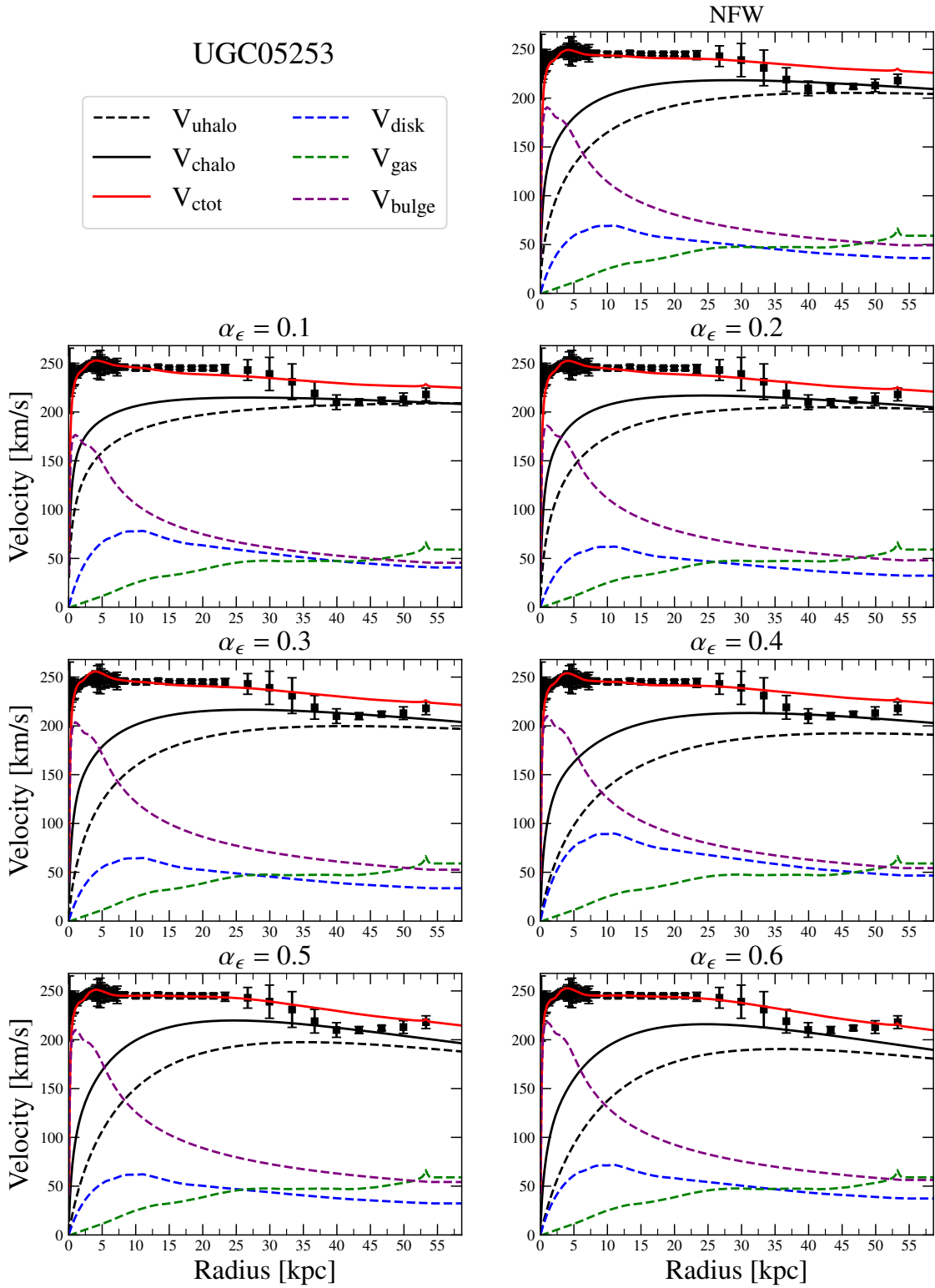


Figure A.23: Same as Figure 3.1, but for galaxy UGC 05253.

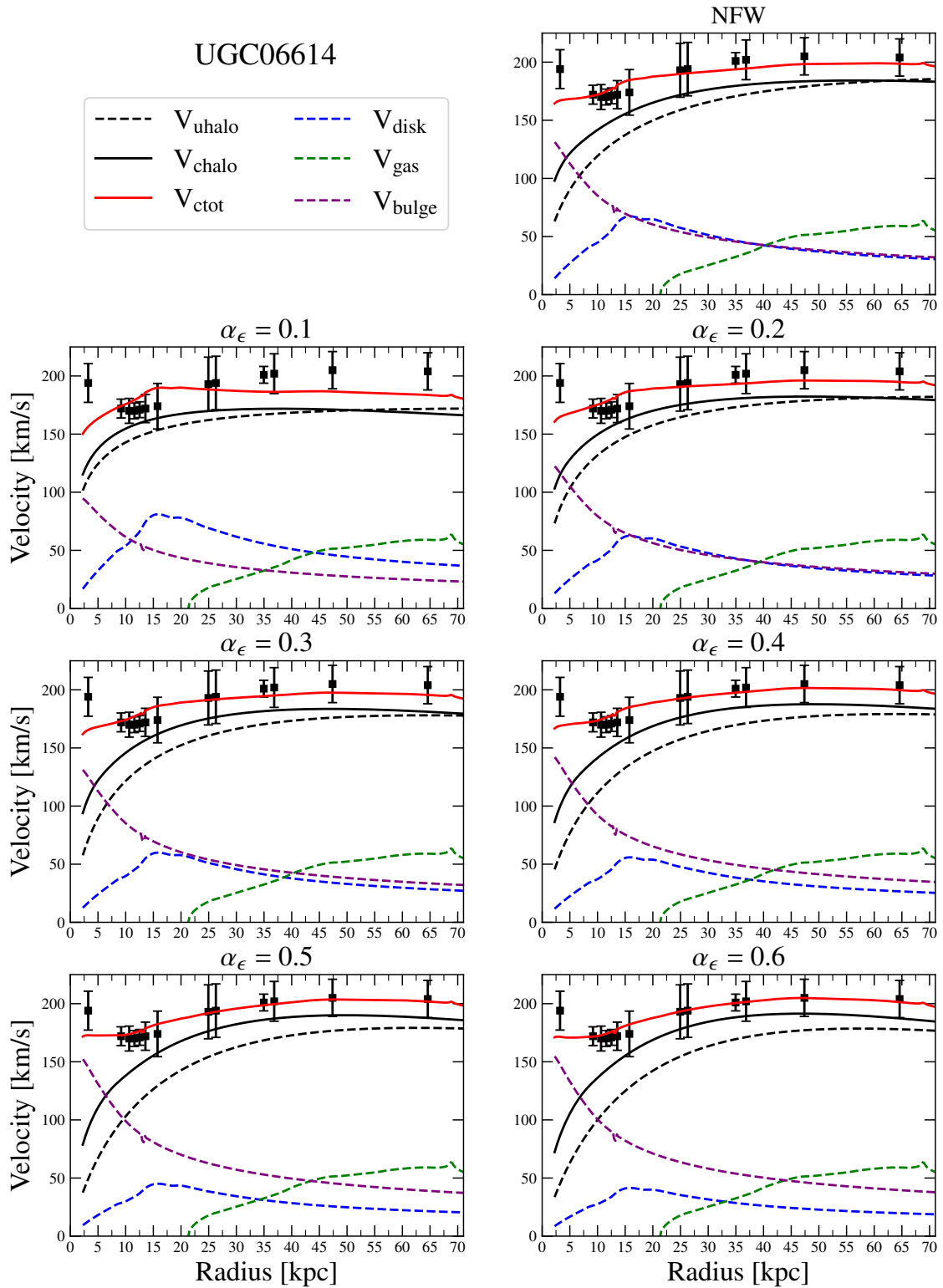


Figure A.24: Same as Figure 3.1, but for galaxy UGC 06614.

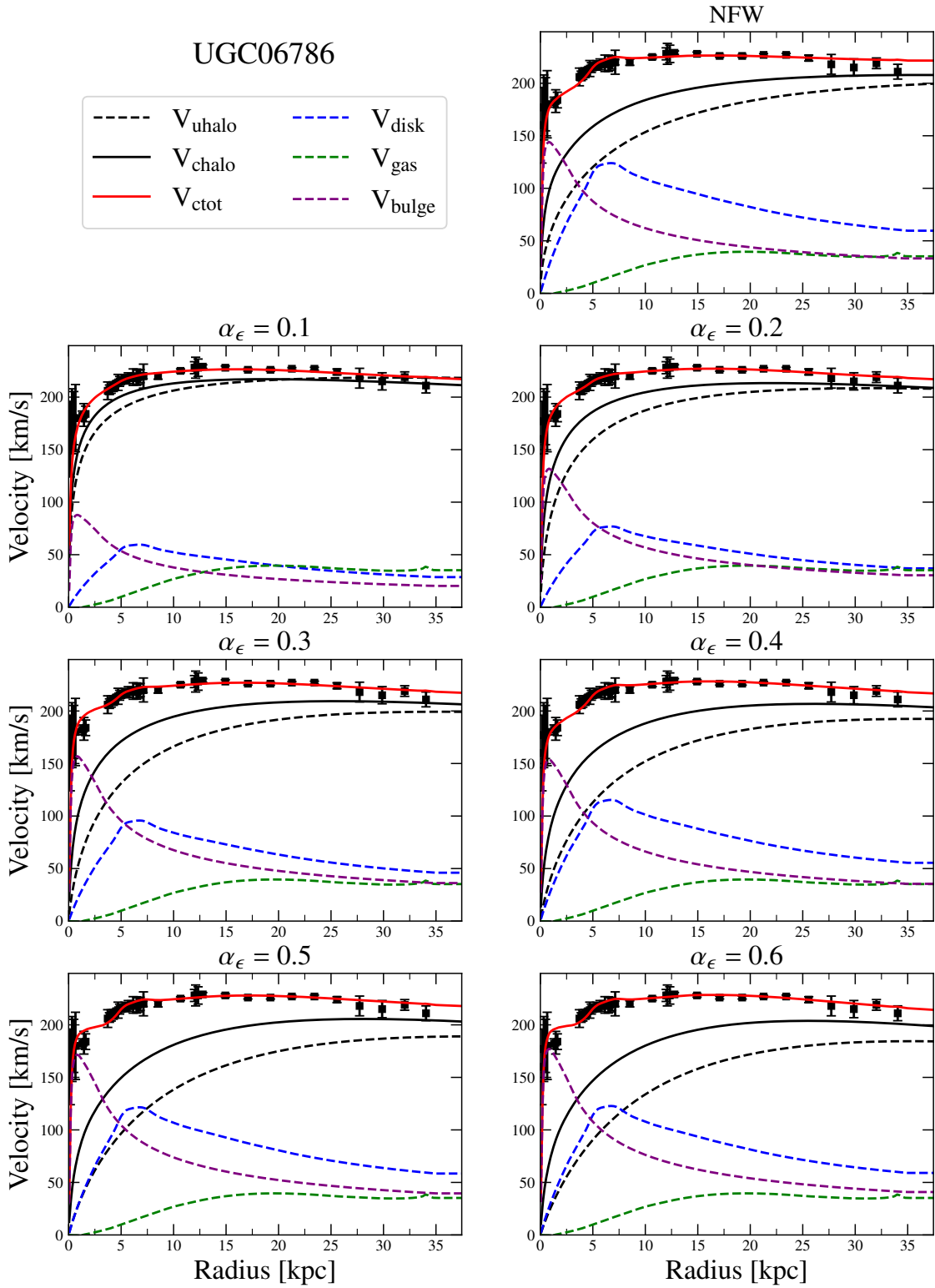


Figure A.25: Same as Figure 3.1, but for galaxy UGC 06786.

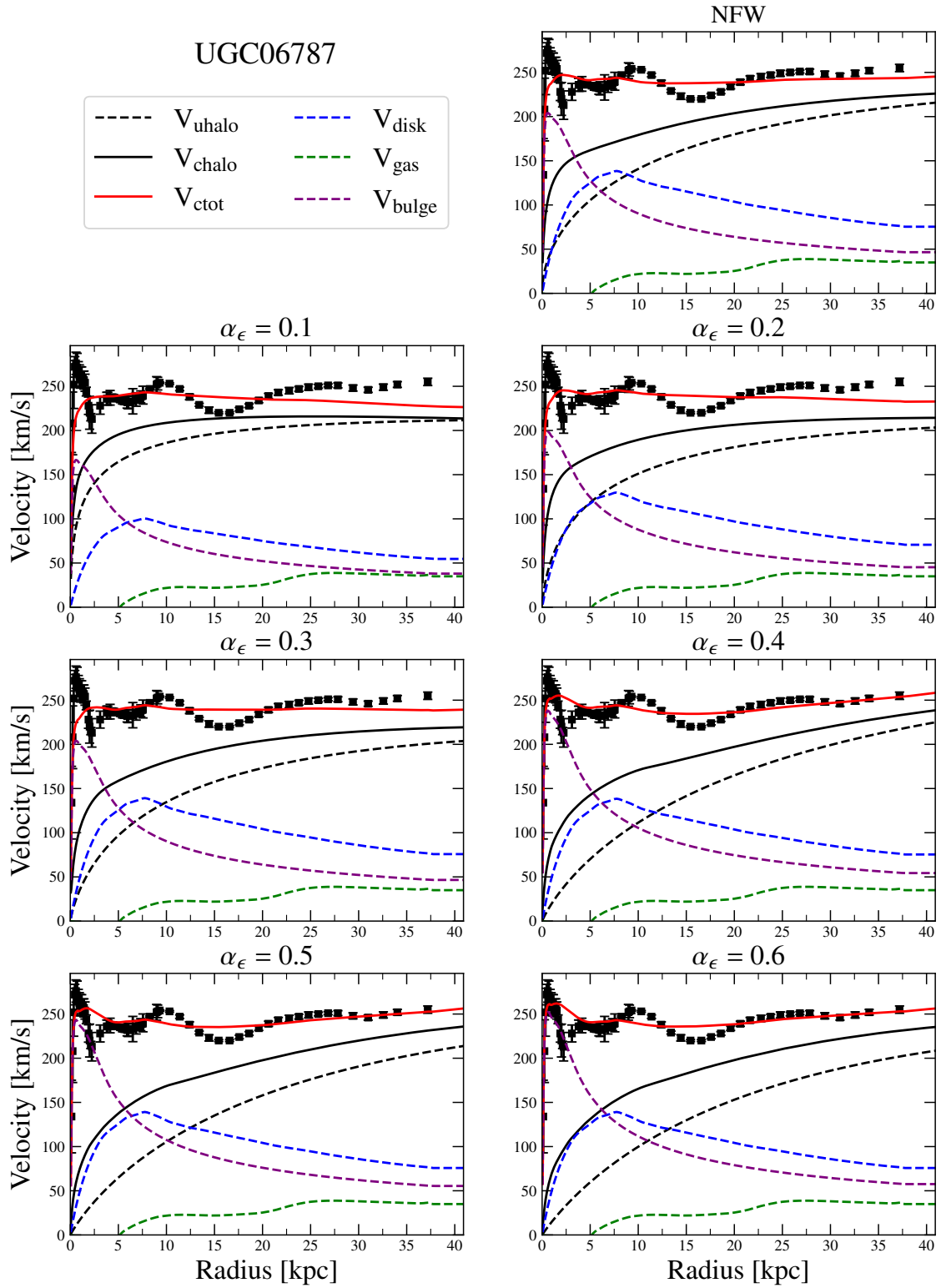


Figure A.26: Same as Figure 3.1, but for galaxy UGC 06787.

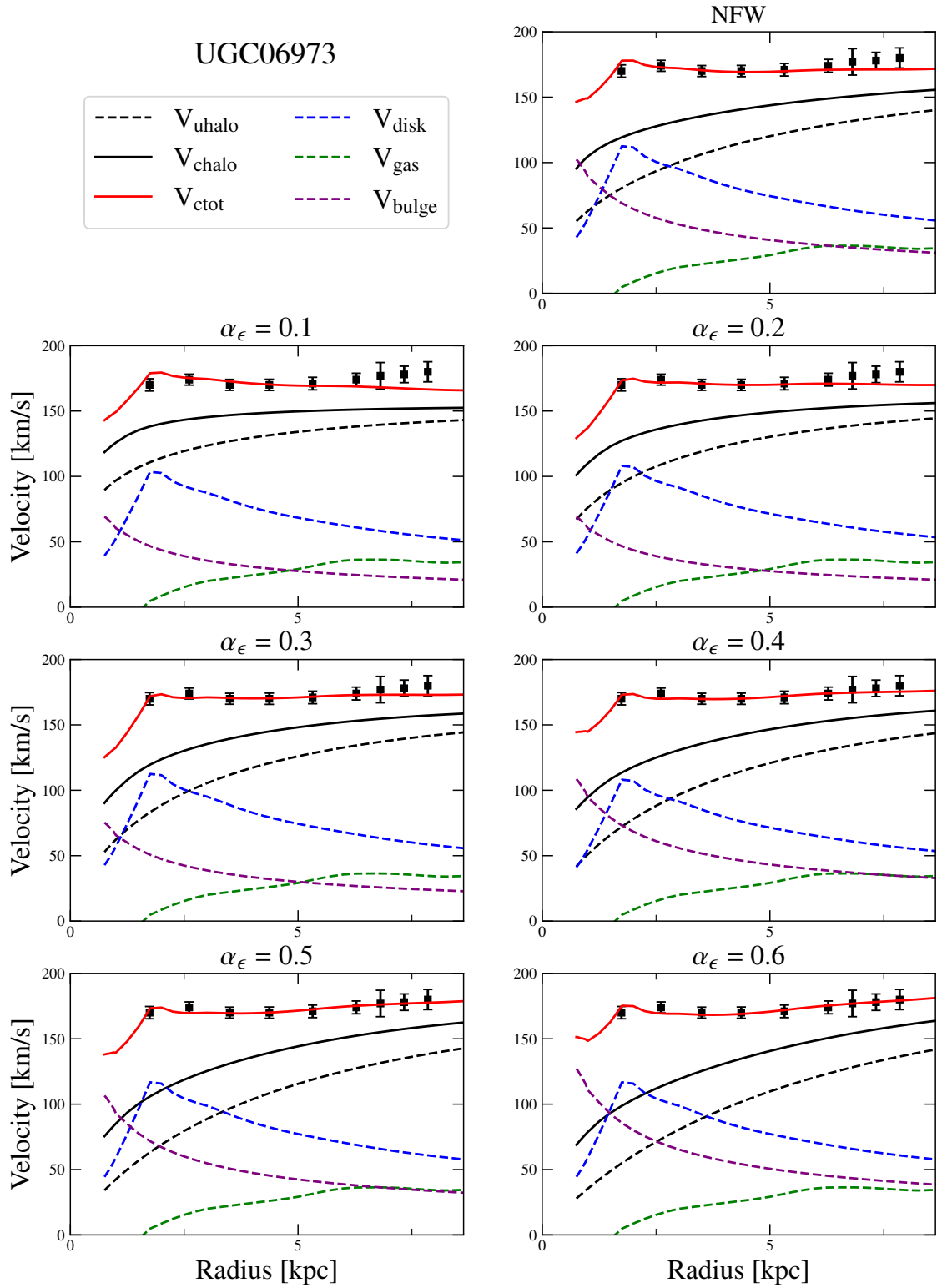


Figure A.27: Same as Figure 3.1, but for galaxy UGC 06973.

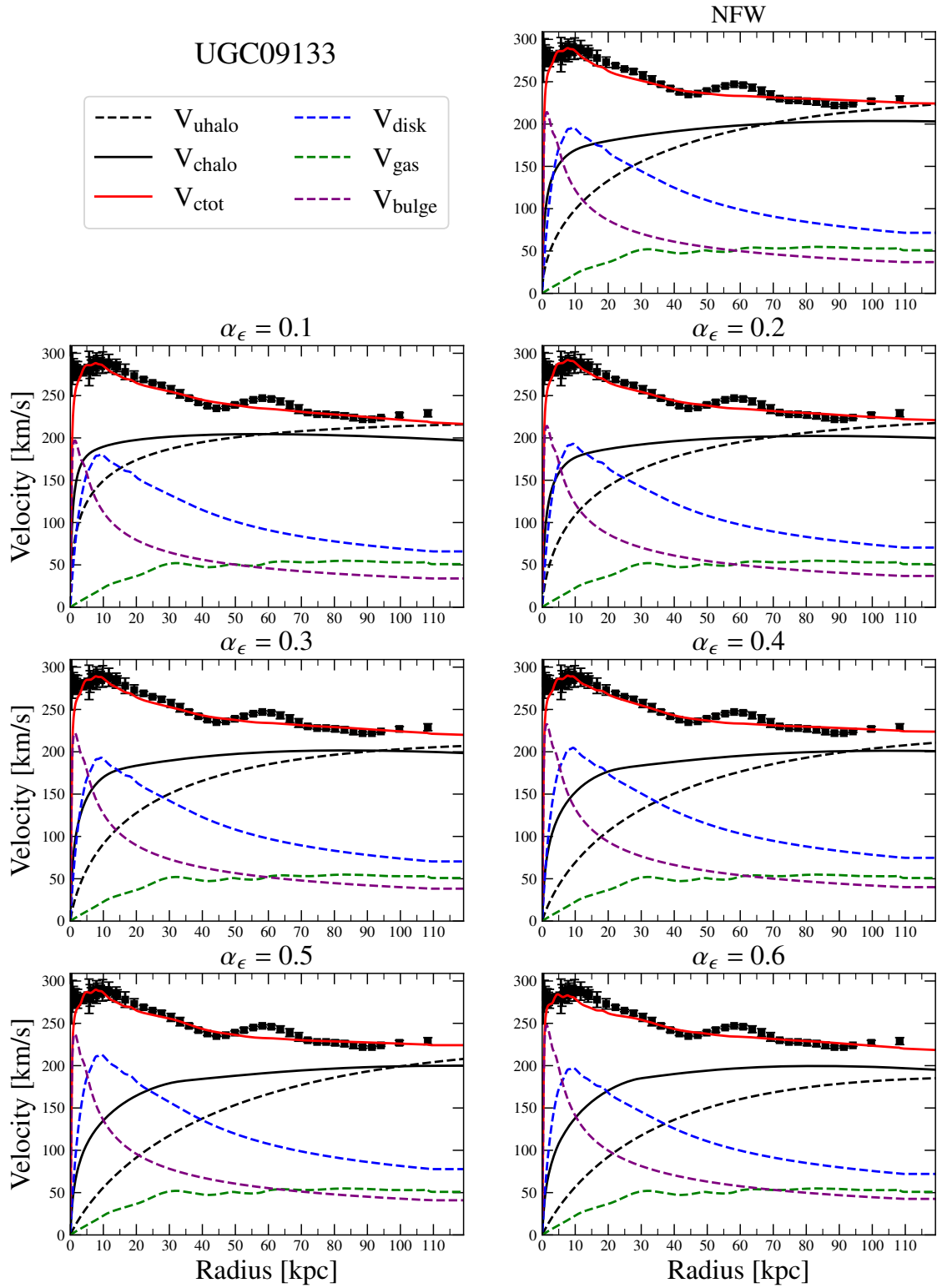


Figure A.28: Same as Figure 3.1, but for galaxy UGC 09133.

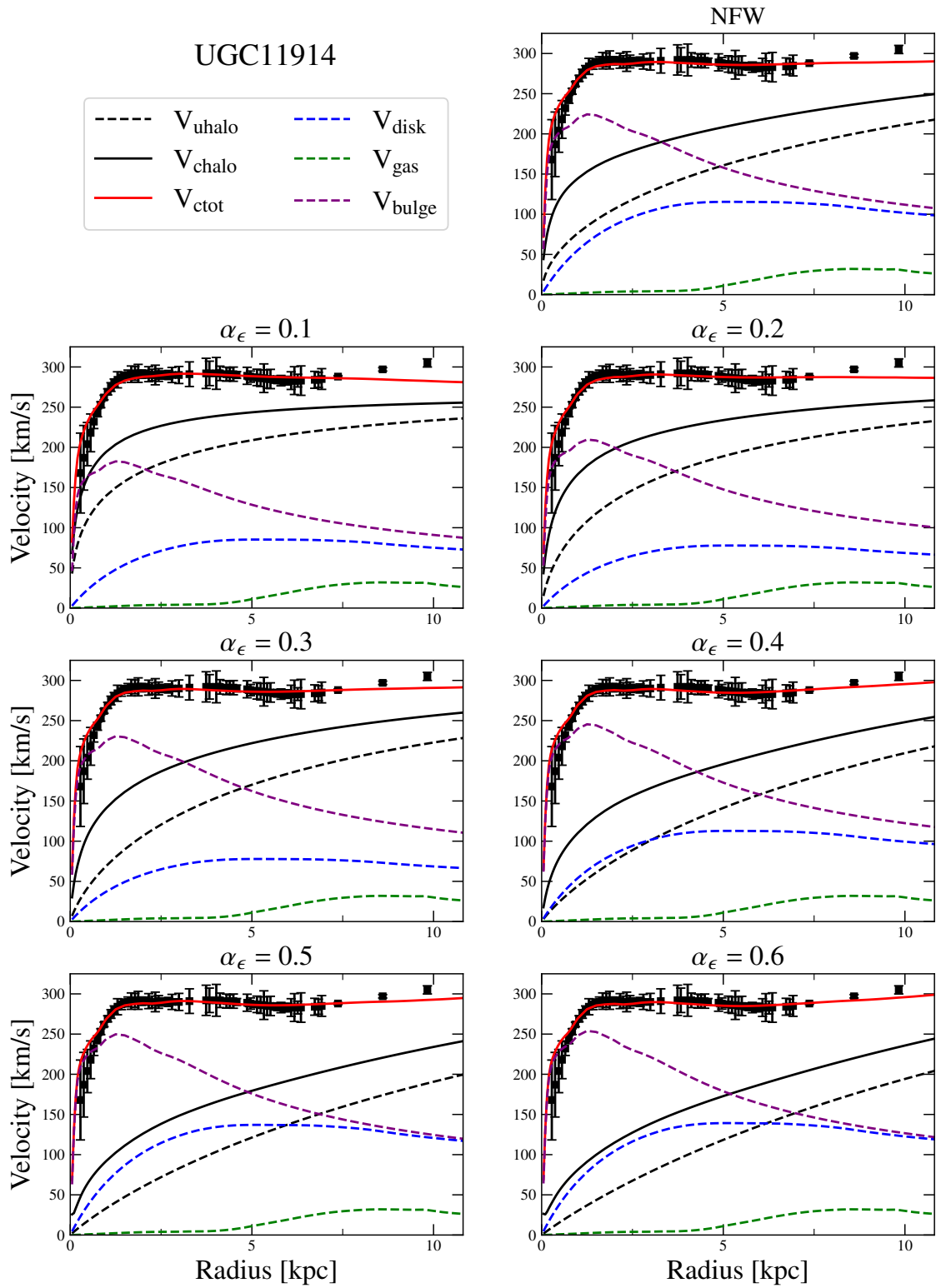


Figure A.29: Same as Figure 3.1, but for galaxy UGC 11914.